



All Theses and Dissertations

2011-08-10

Influence of Subglottic Geometry on Computational and Synthetic Vocal Fold Model Vibration

Simeon L. Smith

Brigham Young University - Provo

Follow this and additional works at: <https://scholarsarchive.byu.edu/etd>



Part of the [Mechanical Engineering Commons](#)

BYU ScholarsArchive Citation

Smith, Simeon L., "Influence of Subglottic Geometry on Computational and Synthetic Vocal Fold Model Vibration" (2011). *All Theses and Dissertations*. 2836.

<https://scholarsarchive.byu.edu/etd/2836>

This Thesis is brought to you for free and open access by BYU ScholarsArchive. It has been accepted for inclusion in All Theses and Dissertations by an authorized administrator of BYU ScholarsArchive. For more information, please contact scholarsarchive@byu.edu, ellen_amatangelo@byu.edu.

Influence of Subglottic Geometry on Computational and Synthetic
Vocal Fold Model Vibration

Simeon L. Smith

A thesis submitted to the faculty of
Brigham Young University
in partial fulfillment of the requirements for the degree of
Master of Science

Scott L. Thomson, Chair
Anton E. Bowden
Steven E. Gorrell

Department of Mechanical Engineering
Brigham Young University
December 2011

Copyright © 2011 Simeon L. Smith
All Rights Reserved

ABSTRACT

Influence of Subglottic Geometry on Computational and Synthetic Vocal Fold Model Vibration

Simeon L. Smith
Department of Mechanical Engineering, BYU
Master of Science

The voice plays a vital role in human communication. The purpose of voice research is to advance the understanding of voice production physics, with the ultimate goal of leading to improved voice care. In this research computational and synthetic vocal fold models were used to explore the role of subglottal geometry in vocal fold vibration. Three specific studies were performed. First, the effect of the inferior vocal fold surface angle on voice production was investigated using a two-dimensional self-oscillating finite element vocal fold model. Varying the inferior angle resulted in significant changes to model vibratory motion, glottal width, flow rate, and energy transfer. The changes were attributed primarily to changes in structural, rather than aerodynamic, factors. Second, subglottic stenosis (SGS) was introduced and parametrically varied in a similar computational model to determine the influence of SGS on vocal fold vibration. High severities of SGS influenced several factors related to vibration, including glottal width, flow rate, flow resistance, and vibration frequency. Subglottal pressure distributions and flow patterns were also affected. Third, the response of a self-oscillating silicone vocal fold model to varying degrees of SGS in an experimental setup was studied. Consistent with the computational SGS study, SGS had an effect on the synthetic model response at high severities. Changes were seen particularly in subglottal pressure and radiated acoustic sound, and consequently glottal efficiency, which may have important implications regarding the effect of SGS on the human voice.

Keywords: vocal folds, vocal fold modeling, subglottis, inferior surface angle, subglottic stenosis, Simeon L. Smith

ACKNOWLEDGEMENTS

First and foremost, I must acknowledge the hand of my Heavenly Father in my life. His guidance led me to choose to get my education at BYU, for which I feel blessed every day. He has helped me to discover a path where I can find enjoyment and best utilize the talents He has given me, motivating me to seek a career in biomedical engineering and obtain a master's degree in preparation for such. I am grateful for the inspiration of the Spirit and the miracles that have occurred to help me succeed in my education and research.

It has truly been a pleasure and blessing to work with Dr. Scott Thomson. The opportunity he has provided me to do voice research has helped me to gain priceless knowledge and experience that will bless me for the rest of my life. I thank him for his counsel, encouragement, patience, and inspiration. The success of my research and thesis are in large part due to his help and expertise. His wisdom and example have not only made me a better engineer and researcher but, more importantly, have inspired me to be a better disciple of Christ.

Special thanks go to my committee members, Dr. Anton Bowden and Dr. Steve Gorrell, for their insightful review of my thesis which led to its improvement. I deeply respect and have enjoyed my association with them.

I give my sincere gratitude to the BYU Mechanical Engineering Department and the National Institute on Deafness and Other Communication Disorders for providing the facilities, resources, and funding that have allowed me to do this research.

I would also like to recognize Preston Murray for his work in developing the synthetic model used for part of this research, as well as other members of the Vocal Fold Modeling Research Group who have contributed their knowledge and ideas.

Finally, I express my love and appreciation for my parents and family, who always offer me their love, support, and encouragement.

TABLE OF CONTENTS

LIST OF TABLES ix

LIST OF FIGURES xi

1 Introduction..... 1

1.1 Background..... 1

1.1.1 Purpose of Voice Research 1

1.1.2 Voice Anatomy and Function 1

1.1.3 Vocal Fold Modeling 3

1.2 Motivation..... 5

1.2.1 Inferior Vocal Fold Surface Angle..... 5

1.2.2 Subglottic Stenosis..... 6

1.3 Thesis Overview 6

1.4 Thesis Outline 7

1.4.1 Effect of Inferior Angle on the Self-Oscillation of a Computational Vocal Fold Model (Chapter 2)..... 7

1.4.2 Influence of Subglottic Stenosis on Computational Vocal Fold Model Flow-Induced Vibration (Chapter 3) 7

1.4.3 Influence of Subglottic Stenosis on Synthetic Vocal Fold Model Flow-Induced Vibration (Chapter 4) 8

2 Effect of Inferior Angle on the Self-Oscillation of a Computational Vocal Fold Model..... 9

2.1 Introduction..... 9

2.2 Methods 11

2.3 Results..... 19

2.3.1 Overview of Model Responses 19

2.3.2 Glottal Width 21

2.3.3	Flow Rate	22
2.3.4	Partially Rigid Model Responses	23
2.3.5	Energy Transfer	24
2.3.6	Flow Separation	31
2.3.7	Comparison to Human Vocal Folds and Previous Models	33
2.4	Discussion	36
2.5	Conclusions	39
3	Influence of Subglottic Stenosis on Computational Vocal Fold Model Flow-Induced Vibration	41
3.1	Introduction	41
3.2	Methods	44
3.2.1	Stenosis Definition	44
3.2.2	Parameterization	48
3.2.3	Computational Modeling and Simulation	50
3.2.4	Verification	51
3.3	Results	53
3.3.1	Overview of Model Responses	53
3.3.2	Glottal Width	55
3.3.3	Flow Rate	57
3.3.4	Flow Resistance	59
3.3.5	Subglottal Flow Visualization	61
3.4	Discussion	64
3.5	Conclusions	67
4	Influence of Subglottic Stenosis on Synthetic Vocal Fold Model Flow-Induced Vibration	69
4.1	Introduction	69

4.2	Methods	69
4.2.1	Stenosis Definition and Parameterization	69
4.2.2	Subglottal Duct	70
4.2.3	Vocal Fold Model	71
4.2.4	Experimental Setup.....	74
4.2.5	Experimental Procedures	74
4.2.6	Uncertainty Analysis and Statistical Significance	76
4.3	Results.....	77
4.3.1	Pressure	77
4.3.2	Glottal Area, Flow Rate, and Frequency	80
4.3.3	Sound Analysis	82
4.3.4	Videokymography.....	84
4.4	Discussion.....	86
4.5	Conclusions.....	88
5	Conclusions and Future Work.....	89
5.1	Effect of Inferior Angle on the Self-Oscillation of a Computational Vocal Fold Model (Chapter 2).....	89
5.1.1	Conclusions.....	89
5.1.2	Future Work	90
5.2	Influence of Subglottic Stenosis on Computational Vocal Fold Model Flow-Induced Vibration (Chapter 3).....	90
5.2.1	Conclusions.....	90
5.2.2	Future Work	91
5.3	Influence of Subglottic Stenosis on Synthetic Vocal Fold Model Flow-Induced Vibration (Chapter 4).....	91
5.3.1	Conclusions.....	91

5.3.2 Future Work	92
REFERENCES.....	93
Appendix A. Uncertainty Analysis	99
A.1 Subglottal Pressure.....	99
A.2 Onset Pressure.....	100
A.3 Flow Rate	100
A.4 Frequency.....	101
A.5 Glottal Area.....	101

LIST OF TABLES

Table 2-1. Flow separation point locations in terms of p^* and A^* for each cases at six phases.....	33
Table 2-2. Data comparing the vibratory behavior of the model used in this study (present model) with human vocal fold vibration.....	34
Table 2-3. Data of vibratory factors from previous self-oscillating models for comparison to vibratory behavior of present model.	35
Table 4-1. Uncertainty in experimental measurements.	77

LIST OF FIGURES

Figure 1-1. Geometry of the human larynx from sagittal (left image) and coronal (right image) planes (adapted from Gray’s *Anatomy of the Human Larynx*, images public domain, www.bartleby.com).....2

Figure 1-2. Coronal cross section of vocal folds showing various tissue layers.4

Figure 2-1. Geometry of the human larynx from sagittal (left image) and coronal (middle image) planes (adapted from Gray’s *Anatomy of the Human Larynx*, images public domain, www.bartleby.com). Right: idealized vocal fold outline with convergent prephonatory glottal angle.10

Figure 2-2. Solid (top) and fluid (bottom) domains, including material properties, for computational model with 40° inferior surface angle. The solid layers had densities of 1070 kg/m³ and Poisson’s ratios of 0.49. The epithelium thickness was 50 μm.....12

Figure 2-3. Vocal fold surface profiles for five inferior surface angles.15

Figure 2-4. Partially rigid vocal fold model (40° case). Shaded area represents fixed portion.16

Figure 2-5. Grid independence study results, comparing minimum glottal width for three grid densities during the first 0.05 sec of the simulations (top) and waveforms over a normalized steady-state cycle (bottom). ——— Model grid density, - - - - - Grid-halved density, - - - - - Grid-doubled density17

Figure 2-6. Top: Time step independence study results, comparing glottal width for three time step sizes. ——— Model time step, - - - - - Doubled time step, - - - - - Halved time step; Bottom: Convergence criteria independence study results. ——— Model criteria, - - - - -Criteria increased by factor of 10, - - - - - Criteria decreased by factor of 10.....18

Figure 2-7. Fluid domain mesh, with view of entire domain (top) and zoomed view of glottal region (bottom).18

Figure 2-8. Solid domain mesh, with view of entire domain (bottom) and zoomed view showing medial portion of the vocal fold model (top).19

Figure 2-9. Model surface profiles at six normalized times throughout the oscillatory cycle ($T = \text{period}$). Dotted lines denote contact line position. Circular markers denote flow separation points.20

Figure 2-10. Steady-state glottal width for fully-flexible model simulations. Vertical dotted lines correspond to phases shown in Figure 2-9.22

Figure 2-11. Flow rate over steady-state cycle of fully-flexible model simulations.23

Figure 2-13. Aerodynamic energy transfer rate (power) and average intraglottal pressure for fully-flexible cases over a steady-state cycle.....	25
Figure 2-14. Velocity, pressure distribution, and energy flux along the vocal fold model surface at $t/T = 0.2$ during a steady-state cycle for 40° and 25° inferior angles. The solid dashed lines in the top and middle rows denote static model position and pressure distribution, respectively.	28
Figure 2-15. Velocity, pressure distribution, and energy flux along the vocal fold model surface at $t/T = 0.59$ during a steady-state cycle for 40° and 25° inferior angles. The solid dashed lines in the top and middle rows denote static model position and pressure distribution, respectively.	29
Figure 2-16. Velocity, pressure distribution, and energy flux along the vocal fold model surface at $t/T = 0.73$ during a steady-state cycle for 40° and 25° inferior angles. Note the different scales on the pressure and energy flux plots for the 40° case. The solid dashed lines in the top and middle rows denote static model position and pressure distribution, respectively.....	30
Figure 3-1. Schematic of stenosis definition process. Using CT scan images of a patient with SGS, the luminal cross-section was approximated with an ellipse, the elliptical area was calculated, and a rational polynomial curve was fit to the area data points to mathematically define the stenosis.	45
Figure 3-2. Schematic of conversion from elliptical airway area approximation to stenosis profile for a rectangular airway with stenosis profile height h and characteristic depth d	47
Figure 3-3. Stenosis profile adapted for two-dimensional airway (plot) compared to three-dimensional segmentation of actual stenosis from CT images (blue model).	48
Figure 3-4. Parameterization of stenosis profile based on ratio of height at each point to peak height from original profile.....	49
Figure 3-5. Fluid domains of FSI model for each severity of stenosis.	51
Figure 3-6. Results of the grid-independence study. ——— Model grid density, - - - - - Grid-halved density, - - - - - Grid-doubled density	52
Figure 3-7. Top: Results of the time step independence study. ——— Model time step, - - - - - Doubled time step, - - - - - Halved time step; Bottom: Results of the convergence criteria independence study. ——— Model criteria, - - - - - Criteria increased by factor of 10, - - - - - Criteria decreased by factor of 10.....	52
Figure 3-8. Profiles showing model motion for the normal (0%), 60%, 95%, and 99% stenosis cases at 600 Pa inlet pressure. Images are zoomed to show just the medial portion of the model.....	54

Figure 3-9. Model oscillation frequency for all stenosis cases at three inlet pressures.	55
Figure 3-10. Glottal width waveforms over a normalized steady-state cycle for all stenosis cases at 300, 600, and 900 Pa inlet pressures.	56
Figure 3-11. Glottal flow rate waveforms over a normalized steady-state cycle for all stenosis cases at 300, 600, and 900 Pa inlet pressures.	58
Figure 3-12. Maximum flow declination rate for each stenosis case at three inlet pressures.	59
Figure 3-13. Average normalized resistance R^* across the glottis and across the stenosis for all stenosis cases at three inlet pressures. Note the logarithmic y scale.	60
Figure 3-14. Visualization of subglottal flow velocity magnitude (color) and direction (arrows) for the normal (0% stenosis) case at 600 Pa. Upper image shows flow at $t/T \approx 0$ (closed glottis). Lower image shows flow at $t/T \approx 0.6$ (around maximum glottal opening).	61
Figure 3-15. Visualization of subglottal flow velocity magnitude (color) and direction (arrows) for the 60% stenosis case at 600 Pa. Upper image shows flow at $t/T = 0$ (closed glottis). Center image shows flow at $t/T = 0.625$ (maximum glottal opening). Lower image shows flow at $t/T \approx 0.82$ (during glottal closing).	62
Figure 3-16. Visualization of subglottal flow velocity magnitude (color) and direction (arrows) for the 95% stenosis case at 600 Pa. Upper image shows flow at $t/T = 0$ (closed glottis). Center image shows flow at $t/T = 0.375$ (during glottal opening). Lower image shows flow at $t/T \approx 0.75$ (during glottal closing).	63
Figure 4-1. Images of subglottal duct and stenosis insert with dimensions.	71
Figure 4-2. Synthetic vocal fold model, showing coronal cross-section with four-layer geometry (left) and isometric view (right).	72
Figure 4-3. Rheological properties of silicone for various vocal fold model layers.	73
Figure 4-4. Experimental setup. Red stars show pressure tap locations in subglottal duct.	75
Figure 4-5. Mean pre- and post-stenosis pressure measurements for each case of stenosis severity. Top right and left plots are at onset pressure (P_{on}) and 125% of onset pressure ($P_{1.25}$), respectively. Bottom plot is at 150% of onset pressure ($P_{1.5}$). Lighter gray represents pre-stenosis pressure, and darker gray denotes post-stenosis pressure. Error bars at P_{on} show one standard deviation.	78
Figure 4-6. Pressure waveforms for the first 0.05 sec of recorded data for the 0% (top), 60% (middle), and 95% (bottom) cases at 125% of onset pressure ($P_{1.25}$).	79
Figure 4-7. Glottal area over a nondimensionalized oscillatory cycle for all three cases at $P_{1.25}$	81

Figure 4-8. Flow rate (left) and model vibration frequency (right) for all cases and pressures. ...82

Figure 4-9. Power spectral density plots for each case at $P_{1.25}$83

Figure 4-10. Power efficiency vs. stenosis severity at three pressures.84

Figure 4-11. Videokymograms for 0% (top), 60% (middle), and 95% (bottom) cases at $P_{1.25}$85

1 INTRODUCTION

1.1 Background

1.1.1 Purpose of Voice Research

Voiced speech is a powerful tool for human communication. For most people the voice is an essential component of everyday interactions, and some rely heavily on their voice for their livelihood (e.g., singers, coaches, teachers, etc.) Disorders of the human voice occur rather commonly, with about 7.5 million people being affected in the U.S. alone (NIDCD, 2010). Because of the vital role of the human voice, such disorders can severely affect quality of life. The primary motivation for voice research is to increase understanding of normal and pathological voice production through application of engineering, physics, and medical principles and practices, which in turn leads to clinical advances. Research in the past few decades has greatly enhanced understanding of the structure and mechanics of the vocal folds and their function during voice production. Through clinical application, this improved understanding has led to better diagnosis, prevention, and treatment of voice disorders, thus improving the quality of life for those who suffer from voice disorders.

1.1.2 Voice Anatomy and Function

Figure 1-1 shows the basic anatomy of the larynx, including the vocal folds. The larynx is situated in the anterior portion of the neck and joins the trachea and the vocal tract (mouth and

nose). Attached to the inside wall of the larynx are the vocal folds. This matching pair of soft tissue folds is positioned just behind and below the laryngeal prominence of the thyroid cartilage and is the functional mechanism of the voice. As shown in the figure, the glottis is the airway space between the vocal folds, with the supraglottis above and the subglottis below. The subglottis and its geometry are central subjects of this thesis research.

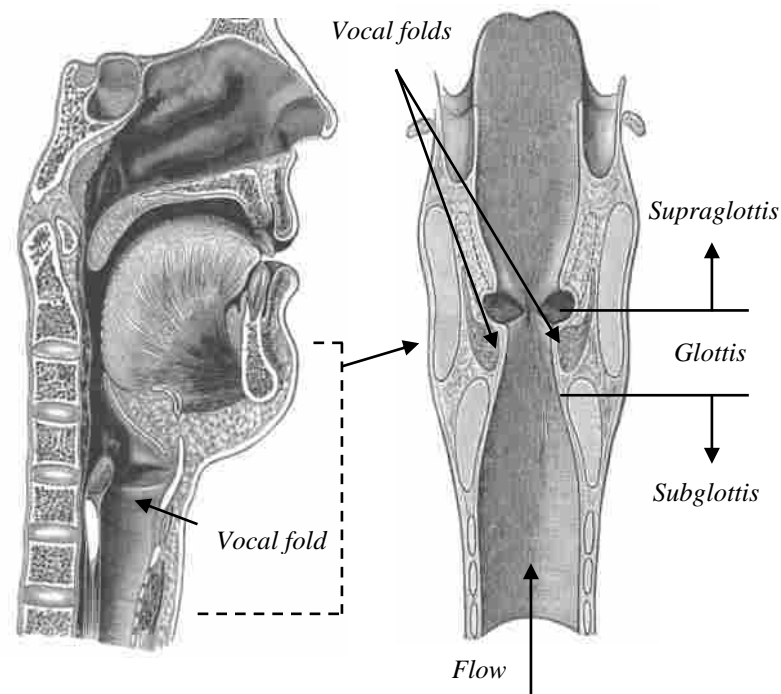


Figure 1-1. Geometry of the human larynx from sagittal (left image) and coronal (right image) planes (adapted from Gray's *Anatomy of the Human Larynx*, images public domain, www.bartleby.com).

The human voice is produced by flow-induced vibration of the vocal folds. Air is driven by pressure from the lungs through the larynx. Self-oscillation of the vocal folds is initiated as the vocal folds move close together medially and air with sufficient pressure is forced through the nearly closed glottis. The oscillations produce pressure fluctuations in the air jet which travel through the vocal tract and out of the mouth, generating audible sound.

Important to the vibratory characteristics of the vocal folds is their tissue composition. The vocal folds consist of various layers of tissue (Figure 1-2), each with differing mechanical properties. The epithelium is a very thin, relatively strong, outermost layer which helps protect the vocal folds during vibration. The lamina propria consists of superficial, intermediate, and deep layers. The extremely soft, gel-like tissue of the superficial lamina propria becomes progressively stiffer through the intermediate and deep layers as the density of collagen fibers increases. The deepest and largest layer is made up of the thyroarytenoid muscle. The loose superficial lamina propria allows continuous, vertically propagating wave-like movement of the vocal fold surface during vibration, which constitutes the “self-oscillation” and creates the pressure fluctuations necessary for sound. The stiffer intermediate and deep layers of the lamina propria and the muscle assist in vocal fold posturing and tension, which affect pitch and sound quality.

1.1.3 Vocal Fold Modeling

The most physiologically accurate methods for studying the voice use real vocal folds, including *in-vivo* studies and excised larynges. Measurements acquired in these ways, however, have limitations. *In-vivo* studies are restricted to imaging from a superior view, which does not allow full exploration of the larynx and suffers from poor spatial resolution. Excised larynges are fairly difficult to obtain and are hard to work with because of tissue sensitivity. Both of these methods are also generally not suitable for parametric studies involving varying geometry and material properties.

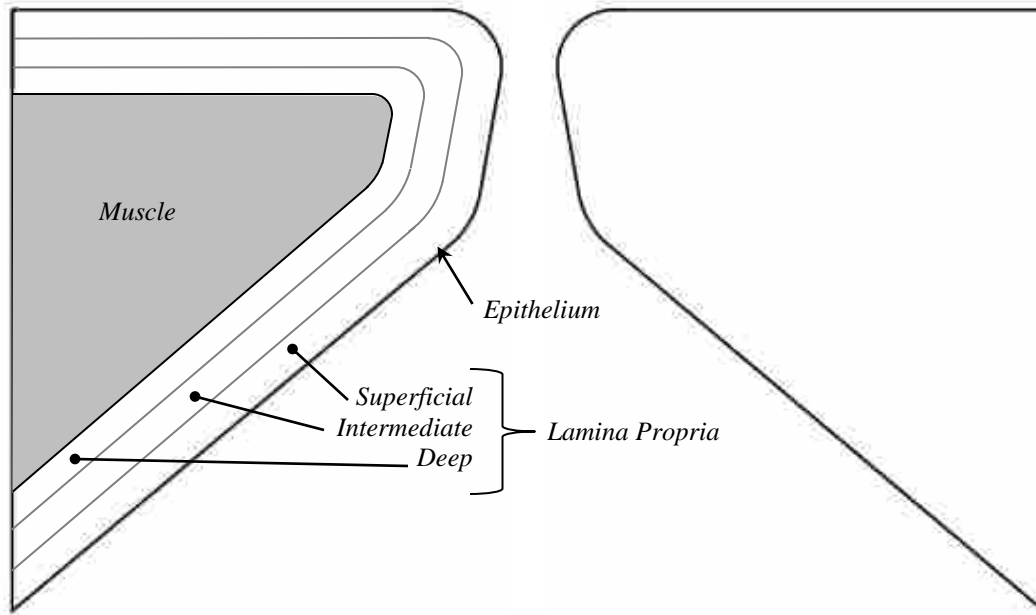


Figure 1-2. Coronal cross section of vocal folds showing various tissue layers.

Models of the vocal folds have been and are commonly used as a practical alternative method for studying the voice. Among the types of models used are synthetic (Titze et al., 1995; Berry et al., 2006) and computational (Story and Titze, 1995; Zhao et al., 2002). Some of the benefits of these models are that they are simple and inexpensive to create, are easily parameterized, and allow for measurement and observation of flow and tissue dynamical characteristics which are otherwise unattainable with real vocal folds. While they do not perfectly simulate vocal fold behavior because of simplified geometry and inability to exactly match material properties, computational and synthetic vocal fold models have been a key tool in gaining insight about the details of vocal fold vibration and the corresponding roles of other components of the vocal tract.

1.2 Motivation

An important area of voice research is the investigation of the influence of laryngeal geometry on vocal fold vibration. Prior studies have explored how glottal and supraglottal geometry affect vocal fold vibration, and other studies have shown that certain properties of the subglottis affect vocal fold vibration. Yet to be explored, however, is the specific influence of subglottic geometry on vocal fold vibration. Two questions regarding subglottal geometry deal with 1) the inferior vocal fold surface angle and 2) subglottic stenosis. These are described below, along with a brief statement of the state of relevant research. A more detailed literature review is provided in subsequent chapters.

1.2.1 Inferior Vocal Fold Surface Angle

The inferior surface of the vocal fold, the tapered portion below the glottis, has been shown to display various angles (θ , Figure 2-1) between human subjects and to vary during voice production (e.g., Agarwal et al., 2003; Nanayakkara, 2005). This inferior angle can also be altered due to surgical procedures (Grisel et al., 2010). While studies of the angle of the medial surface (glottis) have provided evidence that glottal angle strongly influences vocal fold vibration (Hofmans et al., 2003; Scherer and Shinwari, 2000; Li et al., 2006b), the influence of the inferior angle on vocal fold vibration has not been rigorously studied. One previous study suggested that the inferior angle has little effect on intraglottal pressure distributions; however, this was performed using a rigid model that did not self-oscillate (Li et al., 2006a). Thus, the effect of altering the inferior angle on vocal fold vibration needs to be further explored using self-oscillating models.

1.2.2 Subglottic Stenosis

Subglottic stenosis (SGS) is a narrowing of the airway below the vocal folds. Depending on the severity of the stenosis, it can severely affect breathing and is often associated with a degradation in voice quality (Poetker et al., 2006; Giudice, 2003). In addition, many patients who undergo surgery to remove stenosis experience a marked change in voice quality (Smith et al., 1993). Studies that have modeled SGS have been concerned, understandably, only with its effect on respiration. While one study sought to quantify voice quality in SGS patients pre-surgery (Ettema et al., 2006), no studies have been performed to explore the effect of subglottic stenosis on the physics of vocal fold vibration. The influence of subglottic stenosis on vibrating vocal fold models has yet to be explored.

1.3 Thesis Overview

The purpose of this thesis research was to study the influence of subglottic geometry on voice production. Specifically, the separate effects of the inferior vocal fold surface angle and subglottic stenosis on vocal fold model vibration were investigated. The studies were performed using self-oscillating computational and synthetic vocal fold models in order to investigate the fully-coupled fluid and solid model dynamics. It is anticipated that the results of this research will provide insight into the role of subglottal geometry on voice production and motivate future related work.

1.4 Thesis Outline

This thesis is subdivided as follows:

- 1) Effect of inferior angle on the self-oscillation of a computational vocal fold model (Chapter 2).
- 2) Influence of subglottic stenosis on computational vocal fold model flow-induced vibration (Chapter 3).
- 3) Influence of subglottic stenosis on synthetic vocal fold model flow-induced vibration (Chapter 4).

1.4.1 Effect of Inferior Angle on the Self-Oscillation of a Computational Vocal Fold Model (Chapter 2)

Inferior surface angle was systematically varied in a parametric, self-oscillating computational model of the vocal folds in order to determine the aerodynamic and structural effects of changing geometry on model vibration. Model responses to the various angles were compared by qualitative motion analysis and by quantitative measurements including glottal width, flow rate, frequency, and energy transfer.

1.4.2 Influence of Subglottic Stenosis on Computational Vocal Fold Model Flow-Induced Vibration (Chapter 3)

Subglottic stenosis was simulated using a similar computational model as was used in the inferior angle study. Changes in vocal fold model vibration due to varying degrees of stenosis severity were analyzed. The effect of the stenosis was characterized by examination of solid model dynamics, flow and vibration frequency measurements, and flow visualization.

1.4.3 Influence of Subglottic Stenosis on Synthetic Vocal Fold Model Flow-Induced Vibration (Chapter 4)

An experimental setup was created to model an airway with subglottic stenosis. The vibration of silicone, self-oscillating vocal fold models in response to varying degrees of stenosis was investigated. Measurements of pressure, flow, vibration frequency, radiated acoustics, and high-speed images were performed.

2 EFFECT OF INFERIOR ANGLE ON THE SELF-OSCILLATION OF A COMPUTATIONAL VOCAL FOLD MODEL

2.1 Introduction

Flow-induced oscillation of the human vocal folds is the primary mechanism for voiced sound production. Geometry plays an important role in governing the structural vibratory response as well as in influencing the pressure distributions that drive self-oscillation. Consequently, not only is geometry important in healthy phonation, but marked changes in voice quality have been associated with surgical procedures that have altered vocal fold geometry (e.g., Smith et al., 1993). It is therefore important to understand the relationships between vocal fold geometry and oscillation.

As illustrated in Figure 2-1, the airway around the vocal folds can be decomposed into subglottal, glottal, and supraglottal regions. Prior research has shown that the glottal angle (ϕ , Figure 2-1) sweeps through a range of glottal angles as the mucosal wave propagates superiorly and as the glottis profile alternates between convergent and divergent orientations during vocal fold vibration. The prephonatory glottal angle can also vary and influence the ease of phonation. For example, studies of flow through a glottis of different angles showed that some angles yield more favorable flow conditions than others for initiating and sustaining vocal fold vibration (Chan et al., 1997; Lucero, 1998). Other studies have examined glottal pressure distributions in models with varying glottal angles, giving complete pressure distributions for various symmetric

and asymmetric glottal configurations (Scherer and Shinwari, 2000; Scherer et al., 2001; Shinwari et al., 2003; Li et al., 2006b). Some of the same studies have shown how convergent and divergent glottal angles relate to factors such as flow resistance, diffuser efficiency, and flow separation location (Hofmans et al., 2003; Scherer and Shinwari, 2000; Li et al., 2006b).

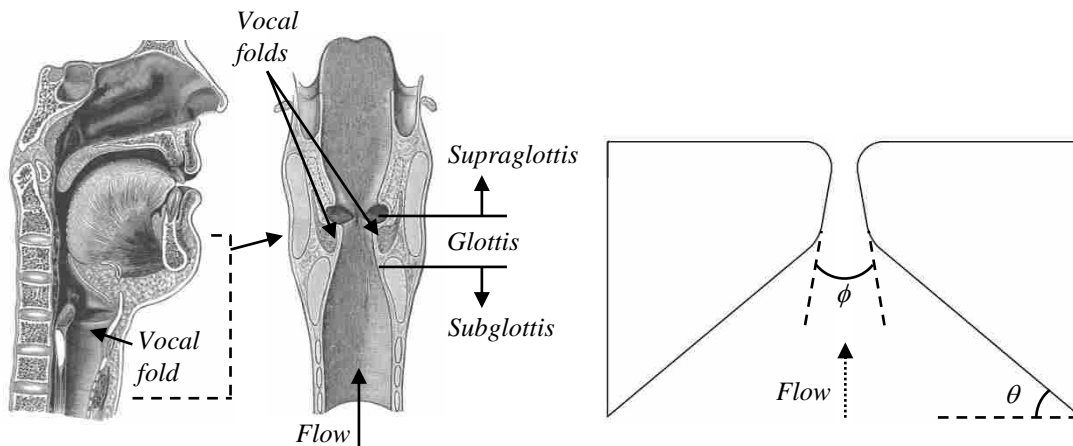


Figure 2-1. Geometry of the human larynx from sagittal (left image) and coronal (middle image) planes (adapted from Gray's Anatomy of the Human Larynx, images public domain, www.bartleby.com). Right: idealized vocal fold outline with convergent prephonatory glottal angle.

As is the case with the glottal angle, the inferior surface profile (θ , Figure 2-1) may also vary. Measurements made on laminagraphic tracings of the vocal fold contours taken during phonation have revealed that the inferior and superior surface angles vary somewhat during the phonatory cycle, and that the average angles over the cycle vary significantly between human subjects (Agarwal et al., 2003; Nanayakkara, 2005). Studies with excised canine larynges, distributed mass models, and finite element models also show motion of the inferior and superior vocal fold surfaces throughout the oscillatory cycle (Saito et al., 1981; Fukuda et al., 1983; Baer, 1981; Titze, 1981; Alipour et al., 2000). In addition, surgical procedures, particularly those that medialize paralyzed vocal folds, can result in considerable changes to the angle of the inferior vocal fold surface (Grisel et al., 2010).

Notwithstanding these studies demonstrating the existence and importance of variations in inferior surface profile, focused, parametric investigations of the influence of the inferior surface angle on vocal fold vibration have been very limited. Two studies have explored the effect of the subglottis profile on turbulence production using static models (Oren et al., 2009; Grisel et al., 2010). Another study explored how both the inferior and superior angles affected pressure distributions in static computational vocal fold models (Li et al., 2006a). Thus, while inferior surface geometry has been studied in the context of these factors, it has not been studied using self-oscillating models.

The purpose of this study was to explore how parametrically altering the inferior surface angle affected the predicted flow-induced response of a deformable computational vocal fold model. Model responses to both fully-couple fluid-structure interaction loading and purely aerodynamic loading were studied. Output variables including model motion, flow rate, intraglottal pressure, and energy transfer were analyzed to determine the sensitivity of the model to changes in inferior surface angle.

2.2 Methods

A finite element model with distinct but fully-coupled air flow (fluid) and vocal fold (solid) domains was created using the commercial fluid-structure interaction solver ADINA (ADINA R&D, Inc.) ADINA has previously been used in other studies of vocal fold flow-induced vibration (e.g., Thomson et al., 2005; Decker and Thomson, 2007). The model was two-dimensional and utilized lateral symmetry for computational efficiency.

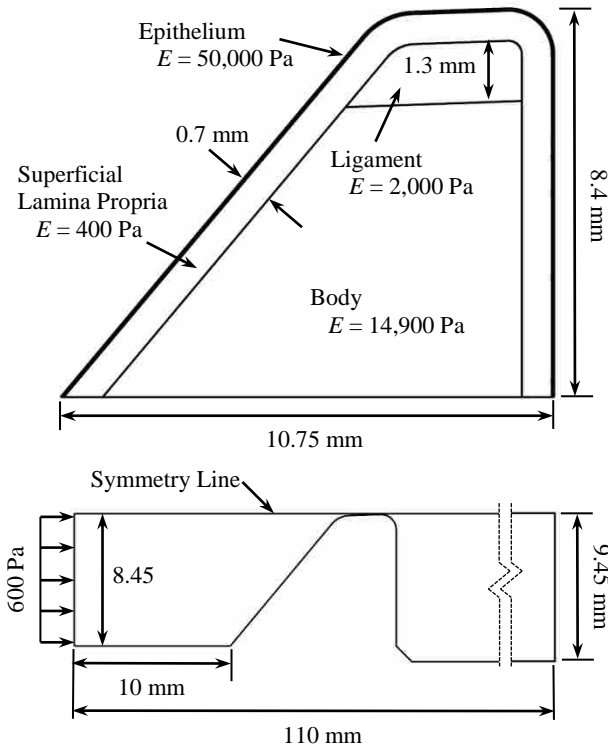


Figure 2-2. Solid (top) and fluid (bottom) domains, including material properties, for computational model with 40° inferior surface angle. The solid layers had densities of 1070 kg/m^3 and Poisson's ratios of 0.49. The epithelium thickness was $50 \mu\text{m}$.

The solid domain included four material layers, with an idealized exterior geometry similar to the model described by Scherer et al. (2001) with the modification of a $\phi = 4^\circ$ (ref. Figure 2-1) convergent-shaped glottis (see Figure 2-2 for geometry and material properties). The four layers generally represented (1) the epithelium, (2) the superficial lamina propria (Reinke's space), (3) the intermediate and deep layers of the lamina propria (ligament), and (4) the muscle (body) (Hirano et al., 1981). To allow for large displacement and large strain, a hyperelastic

Ogden material was defined for the superficial lamina propria, ligament, and body layers using nonlinear stress-strain properties. The shape of the stress-strain curves were derived from the equation

$$\sigma(\varepsilon) = A(e^{B\varepsilon} - 1), \quad (2-1)$$

used by Alipour and Titze (1991) to model the high strain portion of the stress-strain curve for vocal fold tissue. In this equation A was varied while B remained constant. A value of $B=10.5$ was derived by fitting this curve to stress-strain data for vocal fold lamina propria reported by Chan et al. (2007). The Young's modulus tangent to the stress-strain curve is given by $E(\varepsilon) = d\sigma/d\varepsilon = AB e^{B\varepsilon}$. Rearranging this equation allows A to be found for each layer by substituting values for the elastic modulus (E) at a given strain (ε) into the equation $A = E(\varepsilon)/B e^{B\varepsilon}$. For the present study, values for the elastic modulus of the body, cover, and superficial lamina propria layers were determined by a calibration process. The goal of the calibration was to achieve a model response which yielded glottal width amplitude in the expected physiological range (on the order of 1 mm) and vibratory motion which reasonably resembled human vocal fold vibration (convergent-divergent glottal profile and mucosal wave). The calibration examined ranges of elastic modulus values which were within the expected physiological range for each tissue layer. The ranges were roughly 3 to 45, 0.5 to 2.6, and 0.2 to 1.6 kPa for the body, ligament, and superficial lamina propria, respectively. Trial simulations were run, examining the model response to a few different modulus values for each individual layer at a time, in order to determine how changing the properties for a given layer affected the model response. Modulus values and combinations were further varied in a manner that was predicted to give a better model response based on previous simulations. This process was repeated until a combination of modulus values was found which gave a sufficiently desirable model response. The final elastic

moduli for each individual layer, were 0.4, 2, and 14.9 kPa for the superficial lamina propria, ligament, and body layers, respectively. Considering these values to be the slope of the stress-strain curve at 10% strain ($\varepsilon = 0.1$) yielded $A = 22.4, 112.0, \text{ and } 834.5$ Pa for the three respective layers. The epithelium was defined using linear stress-strain data with an elastic modulus of 50 kPa. Damping in the solid model was estimated using the Rayleigh scheme. The specified damping ratio, also determined through calibration in conjunction with the elastic modulus values, was around 0.05 for constants of $\alpha = 56.549$ and $\beta = 3.979 \times 10^{-5}$ for the frequency range between 100 and 300 Hz.

The fluid domain (also shown in Figure 2-2) consisted of subglottal, glottal, and supraglottal sections. Air with a density of 1.2 kg/m^3 and a viscosity of $1.8 \times 10^{-5} \text{ Pa}\cdot\text{s}$ was used. A pressure of 600 Pa was applied to the inlet. The outlet pressure was set to zero. A fluid-structure interaction boundary condition enforced consistent displacement and stress between the fluid and solid domains along the fluid-solid interface. The symmetry line was defined using a slip-wall condition, and the remaining fluid domain lines were defined using no-slip wall conditions. The flow solver was based on the unsteady, viscous, laminar, incompressible, Navier-Stokes equations. The initial gap between the vocal fold medial surface and the symmetry line was 0.05 mm. To prevent total collapse of the fluid domain mesh during vibration, a rigid contact line was placed 0.03 mm above the medial surface, prohibiting motion of the solid model past 0.02 mm from the symmetry line. This resulted in a minimum allowed total glottal width of 0.04 mm.

As shown in Figure 2-3, model geometry was parameterized to create cases with five different inferior surface angles ranging from 15° to 45° . These were the same angles used by Li

et al. (2006a) and are based on a range of values found in humans by Nanayakkara (2005). Other geometric features shown in Figure 2-2 (e.g., cover layer thickness, exit and entrance radius values) remained constant.

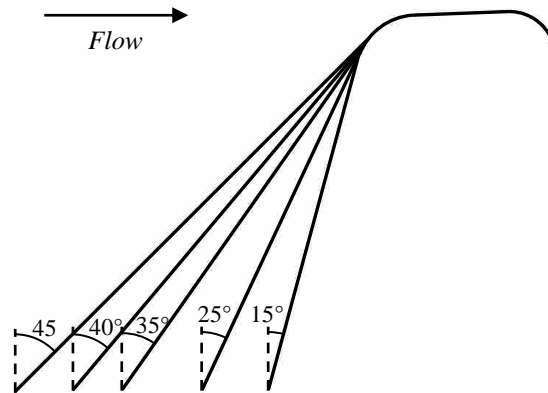


Figure 2-3. Vocal fold surface profiles for five inferior surface angles.

In order to consider aerodynamic as well as coupled fluid-solid dynamic responses, three types of simulations were performed for each of the five inferior surface angles. First, fluid-structure interaction (FSI) simulations were performed in which the complete vocal fold model was allowed to interact with the airflow. These are here referred to as the “fully-flexible” cases. Second, simulations of just the airflow were performed using rigid vocal fold models, as was done by Li et al. (2006a) (“static” cases). Third, partially rigid vocal fold models were studied in order to exclude effects from structural changes as the inferior angle changed. This allowed for the influence of subglottal aerodynamics on model vibration to be investigated, i.e., to determine the degree to which changes in model vibration patterns could be attributed solely to changes in subglottal aerodynamics, as opposed to changes which were due to vocal fold structural dynamics. This was done by adapting the model so that the vibrating portion was a solid model

with a 10° inferior angle, and the remaining geometry given by the desired inferior angle was fixed (see Figure 2-4). FSI simulations for the partially rigid models were run for each angle using the same parameters as the fully-flexible simulations.

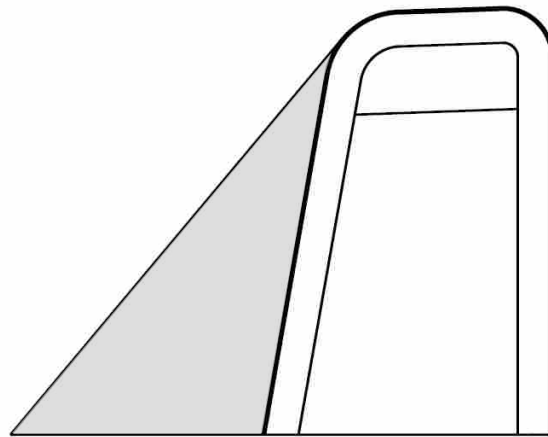


Figure 2-4. Partially rigid vocal fold model (40° case). Shaded area represents fixed portion.

Simulations were performed to ensure that the results were reasonably independent of grid density, time step size, and convergence criteria. These were performed using the 45° case. The study included sequentially varying the grid density by factors of two, the time step size by factors of two, and the convergence criteria by factors of ten. Results were compared by analyzing glottal width waveforms. Glottal width was calculated as twice the minimum lateral distance between the vocal fold medial surface and the symmetry line. Figure 2-5 includes results of the grid-independence study. The top plot gives glottal width for three grid densities during the first 0.05 sec of the simulations. It was observed that the results from the model grid simulation were not entirely independent of grid density. However, the responses were very similar, as can be seen in the bottom plot of Figure 2-5 showing the waveforms for all three grid densities over a normalized oscillatory cycle. Thus, in this case, the results of the model grid

simulations and the other grid simulations were deemed to be satisfactorily close. Results for both the time step size and convergence criteria independence studies, shown in Figure 2-6, yielded considerably less change. The final parameters were as follows. Fluid domain meshes (Figure 2-7) had gradually higher mesh density closer to the glottis and consisted of roughly 32,000 nodes for all cases, maintaining the same mesh density for all cases. The solid domain meshes (Figure 2-8) were of fairly uniform density throughout the domains, and again the same density was used in all cases. They contained approximately 42,000 to 54,000 nodes, depending on the inferior surface angle. Solutions for 6000 time steps with a simulation time step size of 2.5×10^{-5} s were obtained.

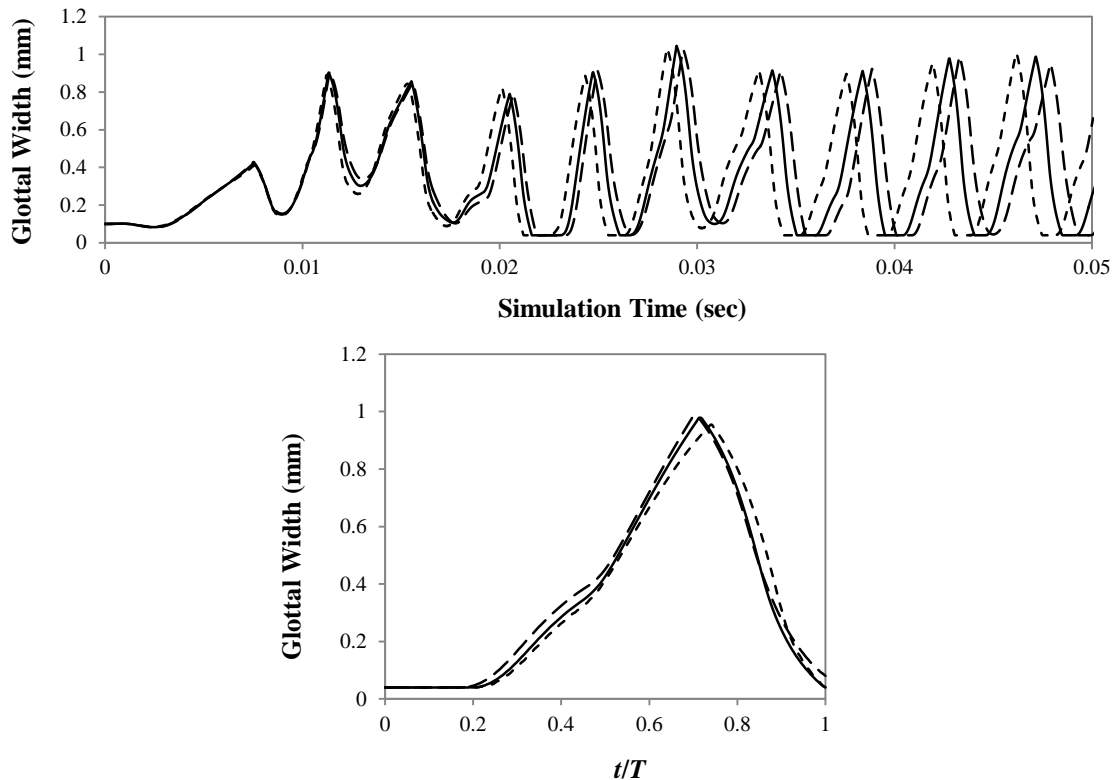


Figure 2-5. Grid independence study results, comparing minimum glottal width for three grid densities during the first 0.05 sec of the simulations (top) and waveforms over a normalized steady-state cycle (bottom). ——— Model grid density, - - - - - Grid-halved density, - · - · - Grid-doubled density

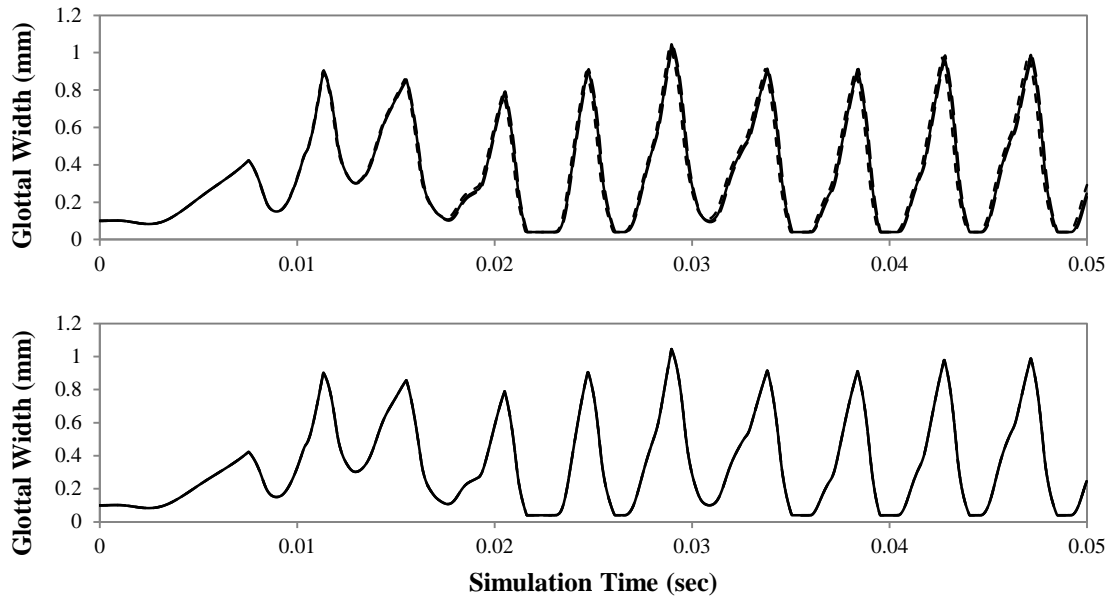


Figure 2-6. Top: Time step independence study results, comparing glottal width for three time step sizes. ——— Model time step, - - - - - Doubled time step, - . - . - Halved time step; Bottom: Convergence criteria independence study results. ——— Model criteria, - - - - - Criteria increased by factor of 10, - . - . - Criteria decreased by factor of 10

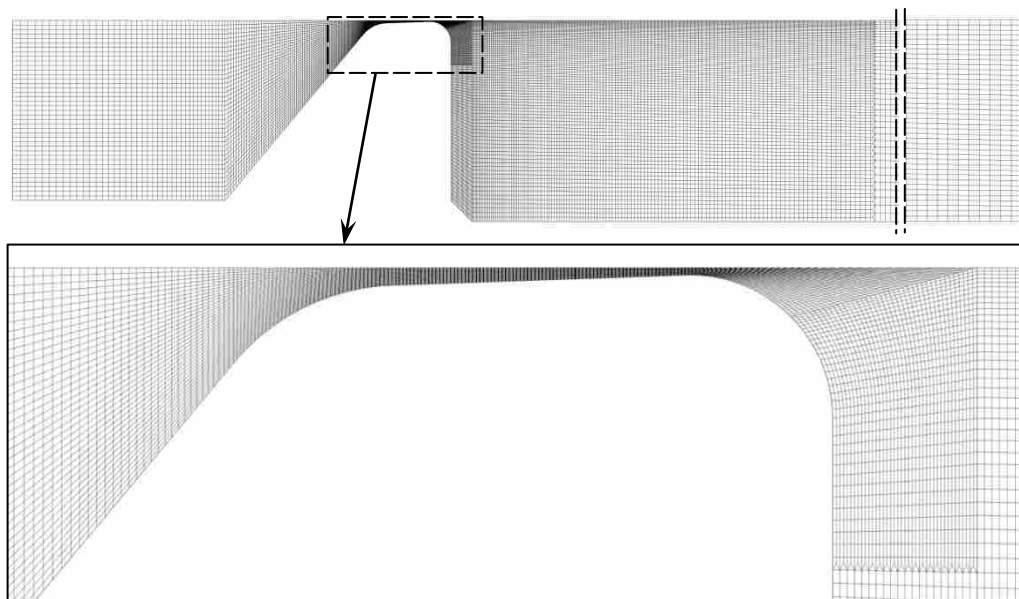


Figure 2-7. Fluid domain mesh, with view of entire domain (top) and zoomed view of glottal region (bottom).

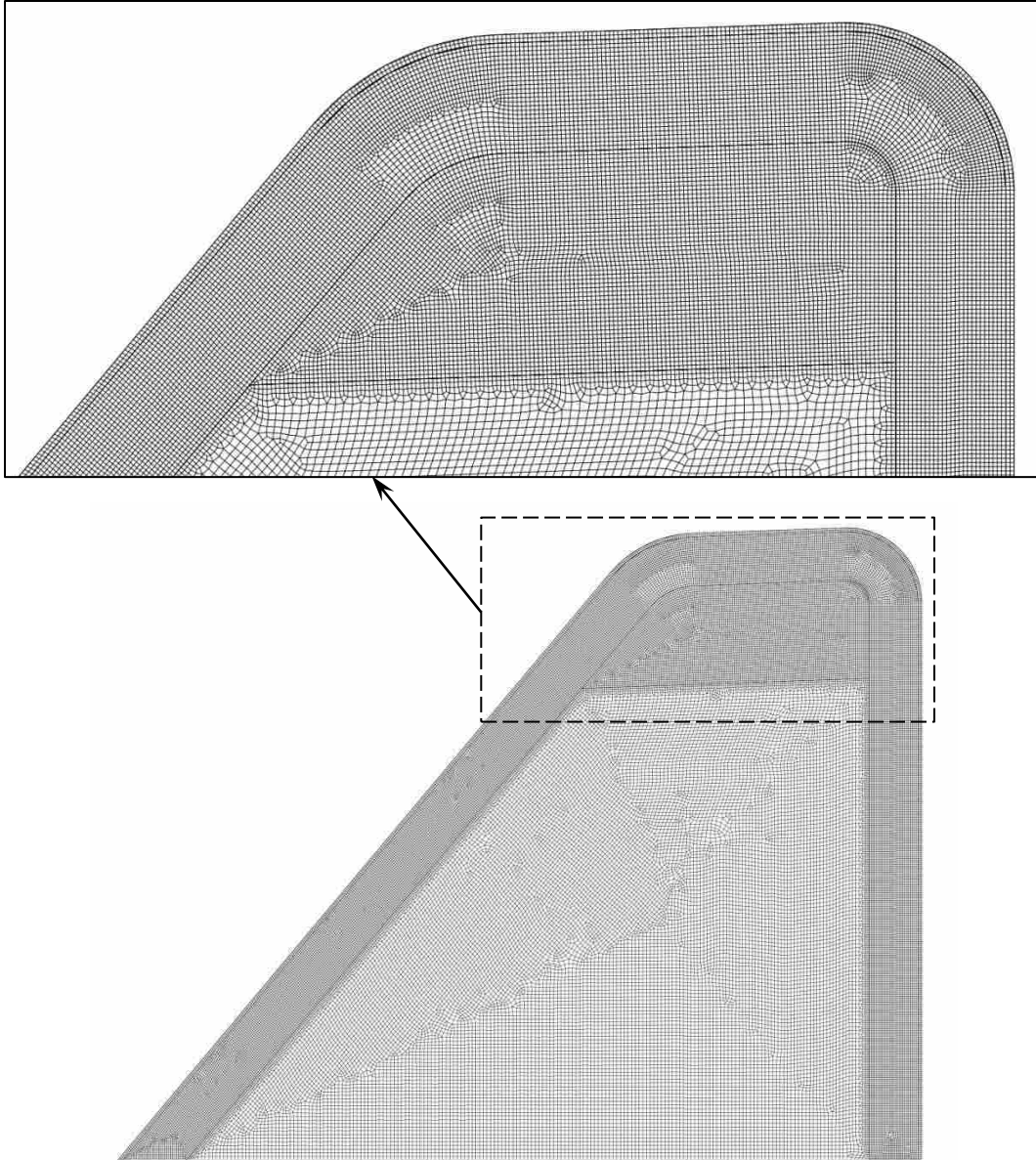


Figure 2-8. Solid domain mesh, with view of entire domain (bottom) and zoomed view showing medial portion of the vocal fold model (top).

2.3 Results

2.3.1 Overview of Model Responses

For the fully-coupled FSI cases, self-sustained oscillation was achieved for all but the 15° model. Vibration frequencies were 225, 229, 228, and 235 Hz for the 45° , 40° , 35° , and 25°

cases, respectively. Instantaneous medial surface profiles are shown in Figure 2-9 for six phases of the oscillatory cycle. The selected phases correspond to instances of significance pertaining to motion and energy transfer (ref. Figure 2-10 and Figure 2-13 as well as Section 2.3.5 below). The first phase ($t/T = 0$) corresponds to a “closed” glottis, or the time at which the glottal gap was at its minimum. The second and third phases ($t/T = 0.2$ and 0.35) were during glottal opening. The maximum opening and the point of transition between opening and closing motion occurred at the fourth phase ($t/T = 0.6$). The fifth and sixth phases ($t/T = 0.73$ and 0.85) were during glottal closing. General characteristics of the vibration were that it took place primarily in the medial portion of the cover, with a wave-like movement along the medial surface which resembled a mucosal wave, and with a glottis profile that alternated between a convergent shape during opening and a divergent shape during closing.

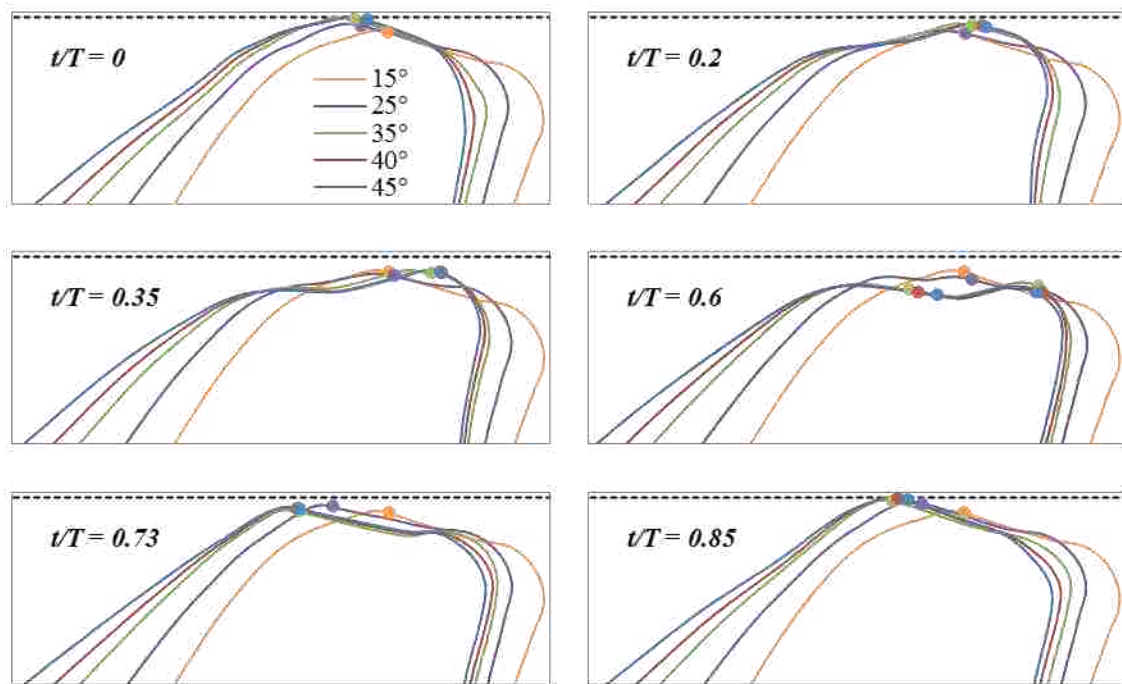


Figure 2-9. Model surface profiles at six normalized times throughout the oscillatory cycle ($T =$ period). Dotted lines denote contact line position. Circular markers denote flow separation points.

The vibratory behavior was similar for the 45°, 40°, and 35° models. For these models inferior-superior displacement was minimal and both the wave-like motion and convergent-divergent shape were apparent through the entire glottis. The only noticeable difference among these first three cases was a slight increase in vertical displacement of the profile as the inferior angle decreased. The point along the profile of minimum glottal width appeared to be essentially the same at all phases for these first three cases. Greater differences were seen, however, in the movement of the 25° model. In this case there was a more substantial increase in inferior-superior model displacement, and a smaller portion of the medial surface (roughly the upstream half) was involved in the alternating convergent-divergent profile change. The downstream half of the medial surface for the 25° model remained in a basically divergent orientation throughout the cycle. The profile of the 15° model is shown the same in all of these figures because self-oscillation was not sustained for this model. This model's steady-state superior displacement much greater than the other cases, and its glottal profile was divergent.

2.3.2 Glottal Width

Steady-state glottal width waveforms are shown in Figure 2-10. For reference, steady state glottal width for the 15° case was 0.47 mm (not shown). Glottal width was essentially the same for the 45° and 40° models. These cases reached full closure (touching the contact plane) for approximately 15% of the cycle and a maximum glottal width of about 0.96 mm. The 35° model's maximum glottal width was slightly smaller (about 0.88 mm). The most significant difference is observed in the response of the 25° model. This model reached a maximum glottal width of 0.67 mm (approximately 30% smaller than that of the other models), and incomplete glottal closure (0.16 mm compared with 0.04 mm for the other models).

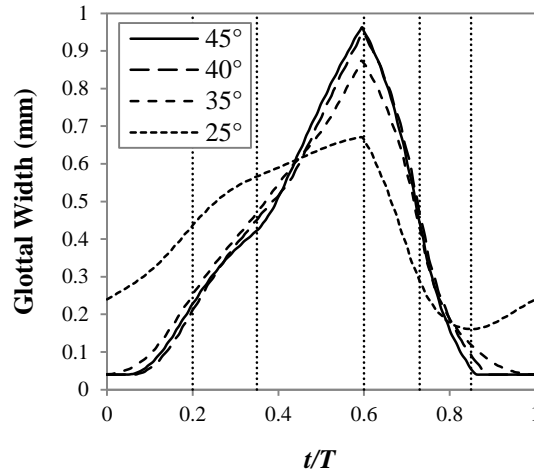


Figure 2-10. Steady-state glottal width for fully-flexible model simulations. Vertical dotted lines correspond to phases shown in Figure 2-9.

2.3.3 Flow Rate

Flow rate waveforms are shown in Figure 2-11. To approximately scale the two-dimensional flow rate data to a three-dimensional model, the flow rate data were multiplied by 1.5 cm (characteristic length of the human vocal folds). The waveform shapes show the maximum and minimum flow closely corresponding to the maximum and minimum glottal width. The exception is the negative flow that occurred between $t/T \approx 0.8$ to $t/T \approx 1$, which was due to reversed flow outside of the glottal jet in the supraglottal region. Similar differences in peak flow rates were seen as with glottal widths. Peak flows were 440 and 437 ml/s for the 45° and 40° models, respectively. A slight decrease (9%) occurred for the 35° inferior model and a greater decrease (30%) occurred for the 25° model. Flow rates at glottal closure were around 40 ml/s for all cases except 25°, which was 122 ml/s. Average flows over the cycle were 198 ml/s for the 25° case and around 177 ml/s for the others.

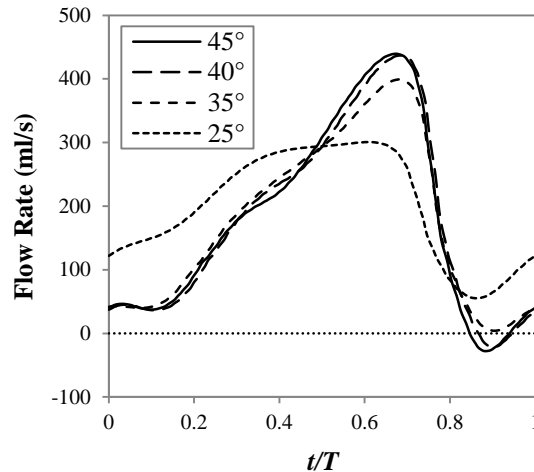


Figure 2-11. Flow rate over steady-state cycle of fully-flexible model simulations.

2.3.4 Partially Rigid Model Responses

Self-oscillation occurred for all inferior angle cases of the partially rigid model with a vibration frequency of approximately 242 Hz for all cases, slightly higher than the frequencies for the fully-flexible cases. Vibratory motion also differed from that of the fully-flexible models. Motion was restricted in the inferior third of the medial surface because of the attached rigid portion, while the superior two-thirds alternated between a convergent and slightly divergent profile. In comparing the medial surface motion among the inferior angle cases for these models, no noticeable differences were observed. Figure 2-12 shows glottal width and flow rate for these simulations. Both glottal width and flow rate amplitudes were less than those seen for the fully-flexible cases. The waveforms are essentially identical for all the cases, confirming that there are no differences in vibratory motion among the cases. The only deviation is a slight time shift between the 45° and the other cases; otherwise, the waveform shapes and frequency were consistent.

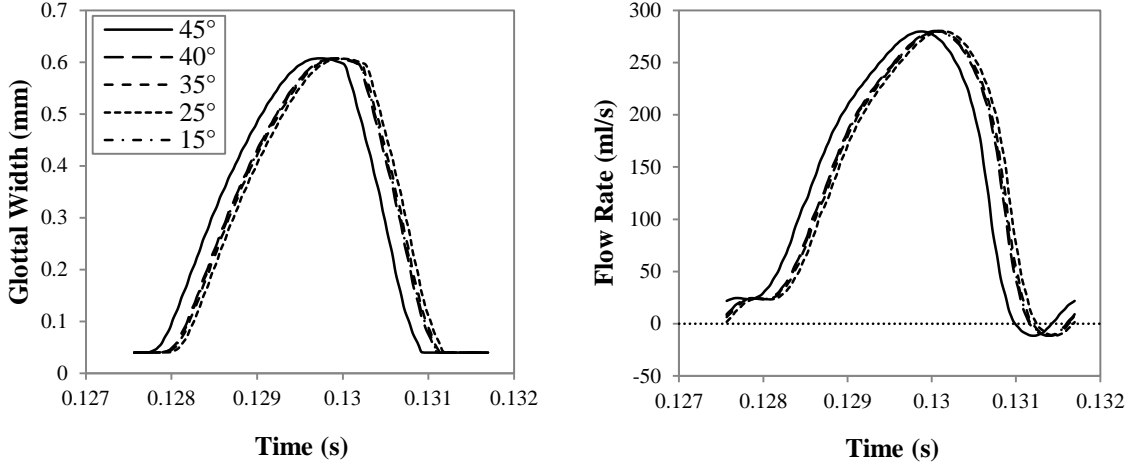


Figure 2-12. Glottal width and flow rate waveforms for a steady-state cycle of partially rigid model simulations.

2.3.5 Energy Transfer

Figure 2-13 shows steady-state aerodynamic energy transfer rate (power) and average intraglottal pressure for the fully-flexible cases. Energy transfer rate is the product of force and velocity, and was here calculated by

$$\dot{E}_p = \int_S u_i (-p\delta_{ij})(-n_j) dS, \quad (2-2)$$

where \dot{E}_p is the energy transfer rate due to normal stress on the vocal folds with units of power (Joules per second), u is the fluid velocity, p is the fluid pressure, n is the control surface outward normal unit vector (points out of the fluid domain), and S represents the control surface (vocal fold surface). The integrand, denoted by \dot{I}_p , is equivalent to intensity or energy flux (energy per unit time and per unit area). Typically, there is an additional viscous stress term (\dot{E}_μ) which, following the analysis by Thomson et al. (2005), is here assumed to be negligible. According to

this equation, a positive energy flux (\dot{I}_p) occurs when the normal pressure acting on the vocal folds is in phase with the component of velocity normal to the vocal fold surface.

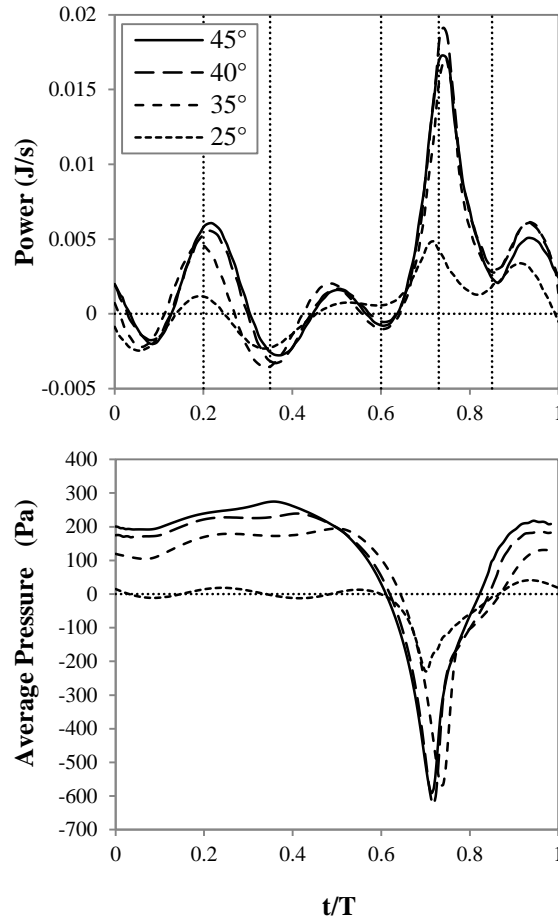


Figure 2-13. Aerodynamic energy transfer rate (power) and average intraglottal pressure for fully-flexible cases over a steady-state cycle.

General trends for energy transfer rate to the vocal fold model included alternating positive and negative values during glottal opening, higher values during the closing portion of the cycle, and nearly no energy transfer for an “open” and “closed” glottis. Average intraglottal pressure can be seen to have correlated relatively well with power, i.e., varying pressures can be seen within the first half of the cycle, and negative pressure can be seen to have occurred during

closing at the times of peak power. Positive energy transfer during opening was produced when the general motion was lateral (a positive normal velocity component) and the average intraglottal pressure was positive. During closing the negative average pressure coupled with closing motion (negative normal velocity component) again resulted in positive energy transfer. At the points of maximum and minimum glottal width, the major contributor to low energy transfer was the low surface velocity of the vocal fold associated with changing direction of the surface motion.

As with the other output measures discussed above, while little difference in energy transfer rate behavior was observed among the 45°, 40°, and 35° models, greater dissimilarity existed between these and the 25° model. For the three highest angles, the waveforms and peak power values were comparable, with the 40° case showing a slightly higher peak than for the other cases and the 35° case varying slightly from the other cases throughout the cycle. Compared to these cases, the major difference apparent in the 25° case was lower amplitude. While the waveform bore a similar shape to the higher angle cases, amplitudes of both positive and negative energy transfer rate were generally lower throughout the cycle. The peak power for the 25° case was substantially lower than the others. Total cycle energy transfer values (integrals of energy transfer rate over one period) also followed this trend. The greatest energy transfer of 1.22×10^{-5} J was seen for the 40° case. The 45° and 35° cases yielded values of 1.21×10^{-5} and 1.00×10^{-5} J, respectively. Total energy transfer was considerably less for the 25° case, at 0.23×10^{-5} J.

Inspection of vocal fold surface velocity, pressure distribution, and energy flux (\dot{I}_p) at particular phases (Figure 2-14 through Figure 2-16) provided further insight into the model responses. Figure 2-14 includes plots of these data for the 40° and 25° cases at the $t/T = 0.2$

opening phase. Note that the behavior of both cases at $t/T = 0$ and $t/T = 0.35$ was similar to that at this phase. Corresponding rigid model profiles and static model pressure distributions are included for comparison. This phase included an energy transfer rate local maximum for both cases. Pressure distribution was the same for all of the static cases. For the fully-flexible cases, pressure distributions differed from the static distributions and were distinct between cases, contributing to differences in energy flux. At this phase, pressures for the 40° and 25° cases drop and reach their respective minima at different locations. This corresponds to the difference in location of the point of minimum glottal width along the medial surface between the models. For the 40° case most of the energy flux was produced in the glottis before the location of minimum width, where the surface velocity into the fold was in phase with the positive pressure. At the location of minimum width, pressure dropped to a negative value while velocity remained into the fold, resulting in the small negative energy flux just before the zero distance mark. Moving downstream along the surface, pressure was slightly positive while surface velocity was away from the fold, causing energy flux to remain negative. On the inferior surface pressure was at essentially the inlet value, while the cover velocity alternated movement on different portions to create both positive and negative energy flux. For the 25° case at this phase, the behavior was similar to the 40° case, but the convergent portion of the glottis was not as large and had a lower surface velocity. It therefore did not create as much positive energy flux.

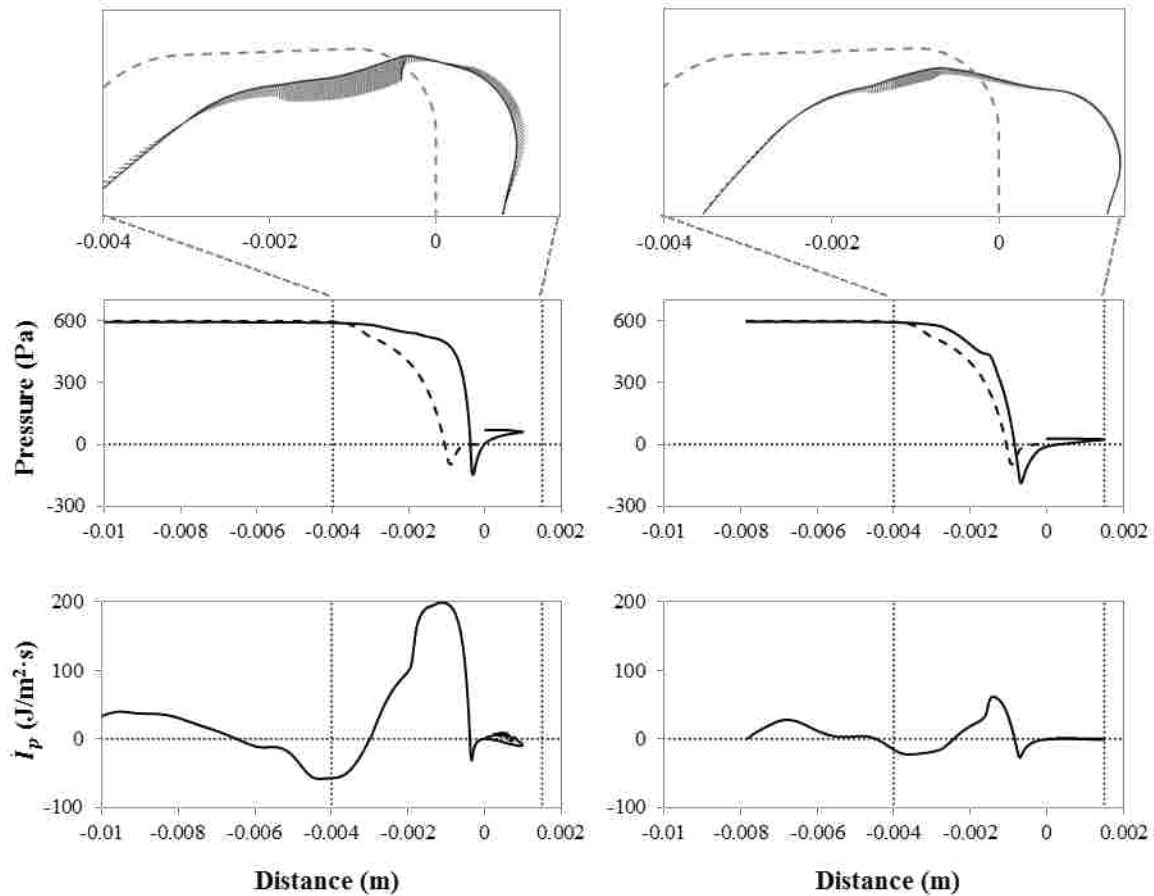


Figure 2-14. Velocity, pressure distribution, and energy flux along the vocal fold model surface at $t/T = 0.2$ during a steady-state cycle for 40° and 25° inferior angles. The solid dashed lines in the top and middle rows denote static model position and pressure distribution, respectively.

The phase $t/T = 0.6$ (Figure 2-15) was the point of maximum glottal opening and a point of almost no energy transfer for all of the cases. Here the pressure distributions were different from the static simulations in that there were two pressure local minima for both the 40° and 25° cases. These were associated with the glottis shape; note the dual elevated regions of the surfaces at both the entrance and exit for the 40° case, and a slight elevated region at the entrance with a larger elevated region in the center of the medial surface for the 25° case. Along the surface energy alternated between negative and positive flux as pressure and velocity went in and out of

phase with each other. Integrating these alternating fluxes across the entire surface resulted in a net energy transfer rate that was close to zero.

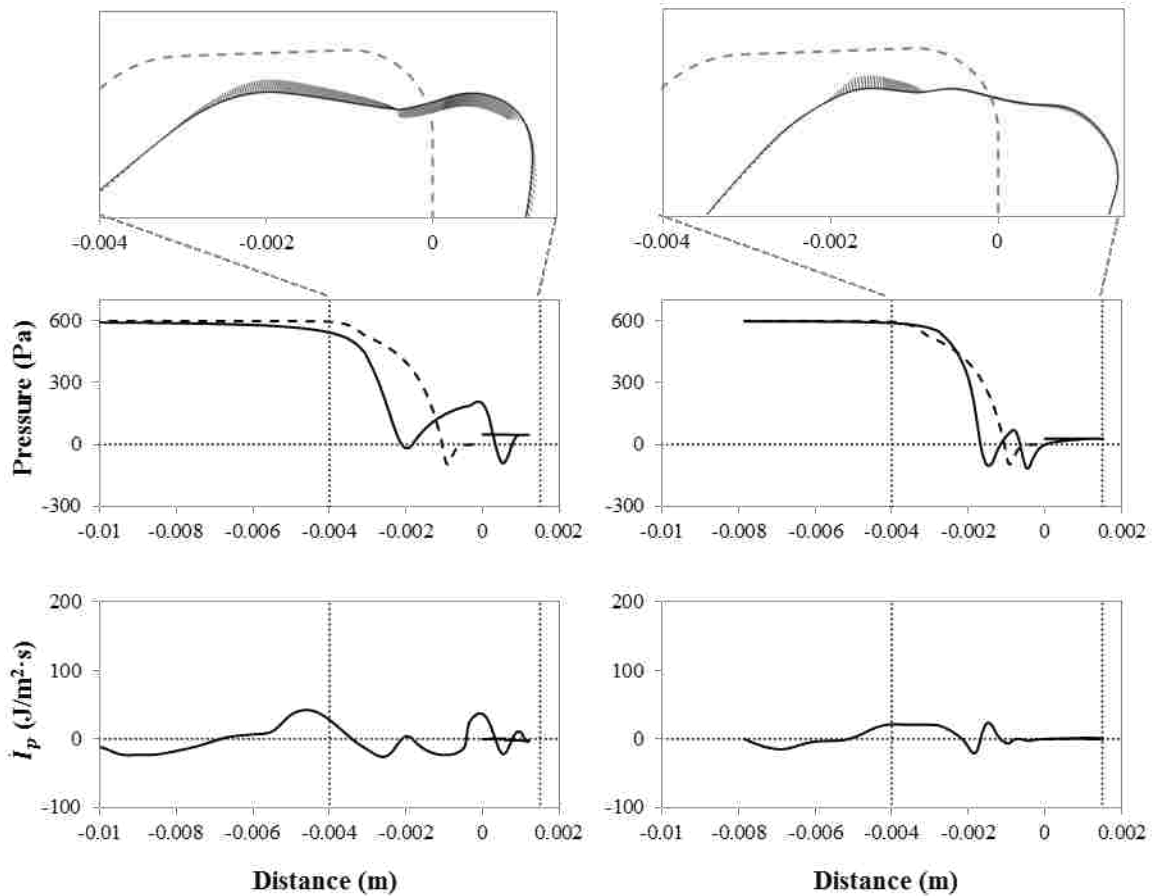


Figure 2-15. Velocity, pressure distribution, and energy flux along the vocal fold model surface at $t/T = 0.59$ during a steady-state cycle for 40° and 25° inferior angles. The solid dashed lines in the top and middle rows denote static model position and pressure distribution, respectively.

Corresponding data at $t/T = 0.73$, the point of highest energy transfer for all the cases, are shown in Figure 2-16. The pressure distribution for the 40° case included a highly negative pressure drop and a recovery pressure that was still significantly less than zero. Notably, this pressure drop was much lower than the corresponding static pressure drop. This highly negative pressure coupled with high closing velocities created a positive energy flux that was higher than

at other phases and occurred over almost the entire vocal fold surface. Considerable positive energy flux also occurred on much of the inferior surface, further contributing to the energy transfer rate at this phase. The pressure distribution for the 25° case was also considerably negative, yet not nearly as great in magnitude as for the 40° case.

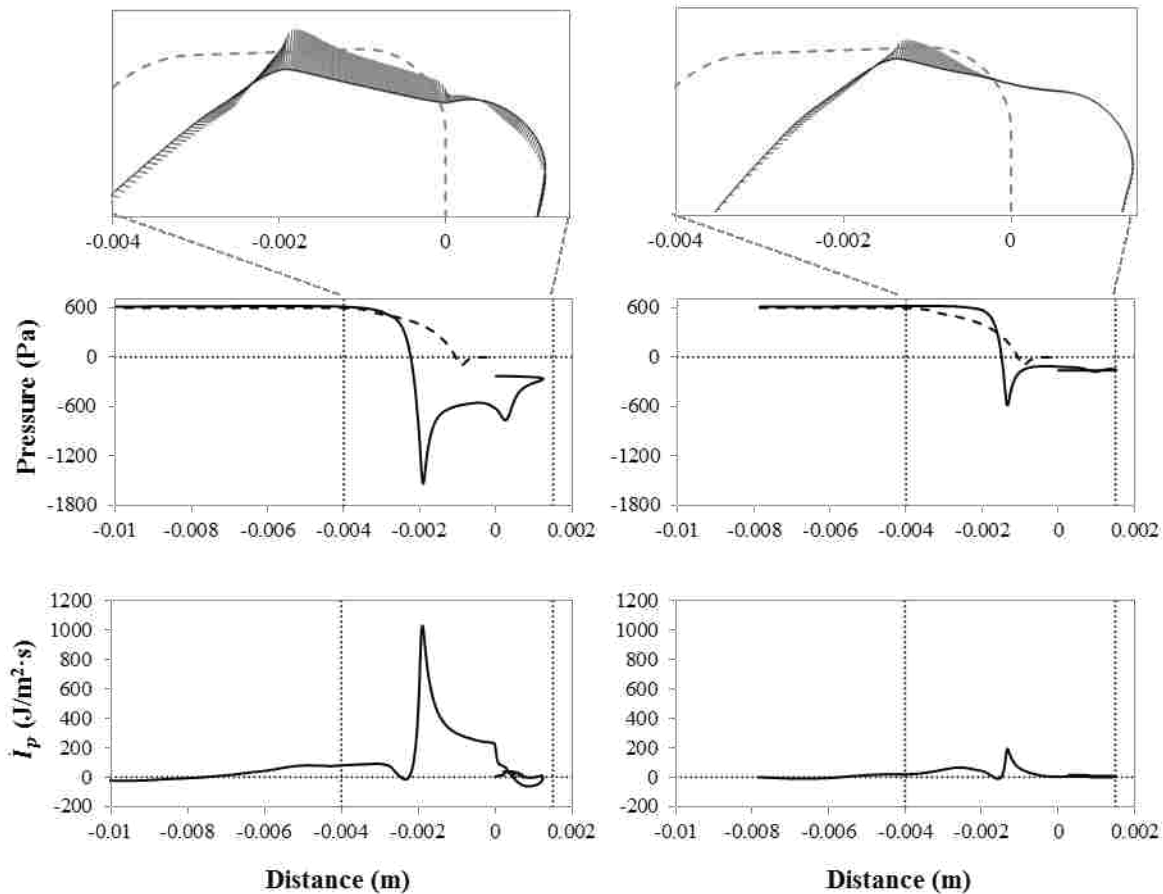


Figure 2-16. Velocity, pressure distribution, and energy flux along the vocal fold model surface at $t/T = 0.73$ during a steady-state cycle for 40° and 25° inferior angles. Note the different scales on the pressure and energy flux plots for the 40° case. The solid dashed lines in the top and middle rows denote static model position and pressure distribution, respectively.

As with the 40° case, the higher closing velocity was in phase with negative pressure, creating a significant amount of positive energy transfer. However, because less of the medial

surface was involved in the movement for this case than for the higher angles and because pressures and velocities were not as great in magnitude, the positive energy transfer value was roughly five times lower than for the other cases.

2.3.6 Flow Separation

Flow separation along the vocal fold surface appeared to occur at all phases for all cases. Separation locations at different phases were visually estimated using flow visualization produced by the commercial postprocessing software EnSight (CEI, Inc.) The circular markers in Figure 2-9 show the estimated separation points. The points were closely grouped at all phases for the 45°, 40°, and 35° cases. During the first two phases, separation point for the 25° case was also grouped with the others. It is important to note that while separation points appeared close to the same location, because the models tended to deflect more superiorly and the point of minimum glottal width moved gradually upstream with decreasing angle, flow separation actually moved slightly upstream in relation to the position of the superior surface for each model as inferior angle decreased. At $t/T = 0.35$ separation for the 25° case is significantly upstream of the other cases and then shifts downstream during closing. An interesting phenomenon was seen at $t/T = 0.6$, where two separation points occurred for 45°, 40°, and 35°. The two elevated surface regions at the glottis entrance and exit caused two distinct pressure drops (see Figure 2-15), which caused flow separation on the recovery of each drop. While there were two peaks on the medial surface for 25° at $t/T = 0.6$, the flow remained attached after the first peak, and there was only one separation point (which was located downstream of the second peak).

For comparison with previously reported data (Li et al, 2006b; Alipour and Scherer, 2004; Decker and Thomson, 2007), separation point location is here related to two measures, one of which is related to pressure distribution, and the other is related to glottal width. For the former measure (here denoted p^*), the pressure drop at separation (Δp_{sep}) is expressed as a percentage of the total pressure drop (Δp_{tot}), i.e.,

$$p^* = \Delta p_{sep} / \Delta p_{tot} \times 100\% = (p_{rec} - p_{sep}) / (p_{rec} - p_{min}) \times 100\%, \quad (2-3)$$

where p_{sep} , p_{min} , and p_{rec} denote the pressure at separation, the minimum pressure, and the downstream recovery pressure, respectively. The recovery pressure was defined as the highest pressure along the vocal fold surface after separation. p^* values for all cases and phases are given in Table 2-1. Average values of p^* over the six phases were 24.9%, 29.0%, 37.3%, and 38.1% for the 45°, 40°, 35°, and 25° cases, respectively. For the 15° case p^* was 45.7%. The same trend of increasing p^* with decreasing inferior angle was seen at $t/T = 0.6$, but the other phases did not show predictable trends. The high and low values were 61.5% for 35° at $t/T = 0.73$ and 7.1% for 45° at $t/T = 0.6$ (upstream separation point).

For the other separation point measure related to glottal width, the area ratio $A^* = A_{sep}/A_{min}$ is used, where A_{sep} is the glottal area at separation and A_{min} is the minimum glottal area (see, for example, Alipour and Scherer, 2004; Decker and Thomson, 2007). A^* values for all inferior angles and phases are listed in Table 2-1. Most A^* values ranged from approximately 1.10 to 1.40. Values were considerably higher at $t/T = 0$ (3.58, 3.73, and 3.48) and $t/T = 0.86$ (3.51, 2.01, and 1.44) for the three highest angles. Average A^* values over all six phases were 1.90, 1.70, 1.58, and 1.25 for the 45°, 40°, 35°, and 25° cases, respectively, with $A^* = 1.13$ for the 15° case, showing a decreasing trend with decreasing angle.

Table 2-1. Flow separation point locations in terms of p^* and A^* for each cases at six phases.

p^*						
	$t/T = 0$	$t/T = 0.2$	$t/T = 0.35$	$t/T = 0.6$	$t/T = 0.73$	$t/T = 0.85$
45°	20.44%	37.07%	38.67%	7.14%, 18.38%	39.14%	13.71%
40°	20.98%	40.65%	32.80%	10.50%, 29.51%	38.55%	29.69%
35°	20.18%	42.41%	29.29%	31.26%, 34.94%	61.45%	41.73%
25°	39.31%	34.65%	43.49%	43.18%	31.32%	36.48%
15°	45.74%	45.74%	45.74%	45.74%	45.74%	45.74%

A^*						
	$t/T = 0$	$t/T = 0.2$	$t/T = 0.35$	$t/T = 0.6$	$t/T = 0.73$	$t/T = 0.85$
45°	3.58	1.39	1.16	1.21, 1.31	1.17	3.51
40°	3.73	1.40	1.20	1.20, 1.27	1.08	2.01
35°	3.48	1.36	1.24	1.15, 1.24	1.13	1.44
25°	1.35	1.27	1.17	1.14	1.17	1.41
15°	1.13	1.13	1.13	1.13	1.13	1.13

2.3.7 Comparison to Human Vocal Folds and Previous Models

In an effort to validate the behavior of the model used in this study, comparisons were made to vibratory behavior of human vocal folds as well as previous numerical and synthetic self-oscillating models. Data from the model with a 40° inferior surface angle was used for comparison, since this geometry has been commonly used in other studies. The vibratory factors that were considered for comparison included glottal width, flow rate, frequency, pressure and qualitative motion.

Table 2-2 shows vibratory factors for the model used in this study (termed “present model”) compared to data measured from the human vocal folds. In general, the present model exhibited features that compare well with actual human vocal fold vibration. Inlet pressure used here was in the range of typical subglottal pressures for softer phonation (e.g., Hsiao et al., 2001; Jiang and Titze, 1993). A maximum glottal width of 0.95 mm was very similar to *in-vivo*

measurements of about 1 mm (Schuberth et al., 2002) and on the same order of magnitude as measurements of up to 4 mm from excised larynges (Doellinger and Berry, 2006; Boessnecker et al., 2007). The average flow rate of 178 ml/s fit within the range from 100 to 400 ml/s for average flow rate in human phonation (Jiang and Titze, 1993; Doellinger and Berry, 2006; Boessnecker et al., 2007). Vibration frequency was in the higher range of the human voice (e.g., Schuberth et al., 2002). The alternating convergent-divergent glottal profile observed in the present model is a characteristic feature of vocal fold vibration and has been shown to be an important factor in sustained self-oscillation of the vocal folds (e.g., Hirano, 1981; Titze, 1988). Also, the inferior-superior propagating wave-like motion in the present model resembles the mucosal wave present along the medial surface of human vocal folds during phonation (e.g., Boessnecker et al., 2007).

Table 2-2. Data comparing the vibratory behavior of the model used in this study (present model) with human vocal fold vibration.

	<i>Glottal Width (mm)</i>	<i>Flow Rate (ml/s)</i>	<i>Frequency (Hz)</i>	<i>Pressure (kPa)</i>	<i>Motion</i>
<i>Human Vocal Folds</i>	1 - 4	100 - 400	120 - 240	0.4 - 3	Alternating convergent-divergent glottal profile; mucosal wave
<i>Present Model (40°)</i>	0.95	178	229	0.6	Alternating convergent-divergent glottal profile; wave-like motion

Table 2-3 gives data for vibratory factors of several self-oscillating computational and synthetic models used in previous studies. A description of each model with the number of material layers, the type of geometry employed, and the numerical solver or synthetic material, is provided. Models with “M5 geometry” had geometry similar to that of the present model. The results of the present model agree reasonably well with and offer some improvements over

Table 2-3. Data of vibratory factors from previous self-oscillating models for comparison to vibratory behavior of present model.

Previous Computational Models

<i>Model Description</i>	<i>Authors</i>	<i>Glottal Width (mm)</i>	<i>Flow Rate (ml/s)</i>	<i>Frequency (Hz)</i>	<i>Pressure (kPa)</i>	<i>Motion</i>
3-layer; continuum models coupled with flow predictions	Alipour et al. (2000); Alipour & Scherer (2000)	0.9 - 2.0	167 - 309	113 - 147	0.8 or 1.6	
1-Layer; 2D M5 geometry; ADINA FSI	Thomson et al. (2005)	4	-	93	2	Briefly convergent, mostly divergent glottal profile; no wave
3-layer; 2D geometry from CT scan; immersed boundary method	Zheng et al. (2009); Luo et al. (2009)	0.9 - 1.5	266 - 322	160 - 230	0.8 - 1.2	Slightly convergent-divergent glottal profile; no wave
2-layer; 2D M5 geometry; ADINA FSI	Pickup (2010)	1.0 - 1.4	150 - 250	113 - 122	0.9	Briefly convergent, mostly divergent glottal profile; no wave

Previous Synthetic Models

<i>Model Description</i>	<i>Authors</i>	<i>Glottal Width (mm)</i>	<i>Flow Rate (ml/s)</i>	<i>Frequency (Hz)</i>	<i>Pressure (kPa)</i>	<i>Motion</i>
1-layer; M5 geometry; Silicone	Thomson et al. (2005)	3.5	169	120	2	Briefly convergent, mostly divergent glottal profile; no wave
2-layer; M5 geometry; Silicone	Riede et al. (2008); Murray (2011)	1.5 - 4.0	550 - 750	100 - 120	0.8 - 1.0	Briefly convergent, mostly divergent glottal profile; no wave
2-layer; MRI-based geometry; Silicone	Pickup & Thomson (2010); Murray (2011)	2.0 - 2.5	800 - 900	130 - 140	1.7 - 2.2	Alternating convergent-divergent glottal profile; wave-like motion
4-layer; M5 geometry; Silicone	Murray (2011)	1.2 - 2.5	250 - 550	85 - 100	0.3 - 0.4	Alternating convergent-divergent glottal profile; wave-like motion

previous computational and synthetic model behavior. Glottal width and flow rate of the present model fit in lower end of the range of glottal width and flow rate values for previous models. The fact that many of the previous models yielded higher values for these factors was possibly due to generally higher operating pressures for the previous models. Frequencies for the present model were typically considerably higher than for previous models, most likely because of its nonlinear stress-strain properties (discussed in section 2.4). The mucosal wave-like motion and well-defined convergent and divergent glottal profiles of the present model were an improvement over the behavior of several previously used models and were similar to the motion of some more recent synthetic models.

2.4 Discussion

Results showed that changing the inferior angle significantly influenced model behavior. The behavior of the models tended to become less characteristic of actual vocal fold vibration as the inferior angle decreased. While the changes were less noticeable from 45° to 35° , the 25° case showed that decreasing the inferior angle increased vertical displacement. With a smaller inferior angle, the overall mass and effective stiffness of the model was lessened. Given that each case was subjected to the same boundary conditions, it was natural that the models with less mass and stiffness would be deflected more in response to the flow. The increased deflection changed the overall glottal profile to a more divergent shape and also increased the pre-steady-state glottal width, factors which are known to adversely affect vibration (Lucero, 1998). Decreases in glottal width and flow rate amplitudes were associated with the changes in vibration as inferior angle decreased.

Changing the inferior surface angle clearly altered the structural response of the models by changing both mass and stiffness. The purpose of the partially rigid model simulations was to remove these effects and explore how vibration was affected solely due to any changes in aerodynamics that were introduced by changing the inferior angle. As was shown, there were essentially no differences in vibration among the cases for these models. This indicates that the inferior angle itself did not introduce any significant aerodynamic changes in the flow that altered vibration. This is consistent with the findings of Li et al. (2006a) that pressure distributions were not affected with changing inferior angle, but the present study extends this conclusion to the self-oscillating case. It can therefore be concluded that the observed changes in vibration seen in the fully-flexible models were primarily due to changes in structural, not aerodynamic, responses.

In order for self-sustained vocal fold oscillations to occur, a positive net airflow-to-tissue energy transfer is required to overcome energy dissipation within vocal fold tissue (Titze, 1988; Thomson et al., 2005). The present results showed a positive net energy transfer to the vocal folds for all self-oscillating cases. Generally, the energy transfer decreased with decreasing inferior surface angle.

Separation point measurements found here support the findings of previous studies. p^* values showed that separation points occurred upstream of total pressure recovery. This observation is consistent with general fluid dynamic theory as well as other voice production studies (Shinwari et al., 2003; Li et al., 2006b; Hofmans, 1998). For example, Li et al. (2006b) reported values of $p^* = 6.5\%$, 13.0% , 41.9% , and 34.4% for static divergent models with intraglottal divergence angles of 5° , 10° , 20° , and 40° , respectively; these values are similar to the p^* values from the present self-oscillating models. A^* values presented here are similar to

values in the range of 1.00 to 1.73 reported by Decker and Thomson (2007), as well as values in the range of about 1.1 to 1.9 with an average of 1.47 predicted by Alipour and Scherer (2004). The much higher A^* values seen in the present models typically occurred when the glottis is at its maximum closure, where the glottal width (A_{min}) is very small, so the area ratio will naturally be larger than at other times.

Separation point also plays a role in energy transfer to the vocal folds by affecting pressure distributions. The detachment of the flow signifies that the pressure from that point on is close to the recovery pressure, which is smaller in magnitude (if not zero) and therefore results in little to no energy transfer. Thus, if separation occurs more upstream than down, average pressures are generally lower and energy transfer is generally less. The general trend in these models is that the separation point moved upstream on the medial surface with decreasing angle, especially during glottal opening. This is consistent with the lower average intraglottal pressures during opening and less energy transfer for smaller angles.

The calibration of material parameters showed that the model response was sensitive to material properties. In addition, geometry was shown to affect model response as the inferior surface angle was changed. The sensitivity of the model to both of these factors suggests that the utilization of different material properties or profile geometry than that used in this study may produce different results than those shown here. Because self-oscillation is a nonlinear process it is unpredictable how and to what extent vibratory response would differ. In theory, the better a model matches the shape and tissue behavior of the human vocal folds the more accurate the response would be. It should also be noted that this model did not include turbulence, which could be increased or decreased by changes in geometry. This would affect flow aerodynamics

which may contribute to variation in the model response. Consideration of these issues should be included in future studies.

2.5 Conclusions

A two-dimensional, self-oscillating, finite element model of the vocal folds was used to study the effect of changing inferior vocal fold surface geometry on vocal fold vibration. Fully-coupled fluid-structure interaction simulations with varying geometry were performed. Simulations using a partially rigid model were carried out in order to isolate and study the effects of changing subglottal aerodynamic loading on the model. Results of the fully-flexible model simulations showed that vocal fold vibration was significantly altered as the inferior angle of the model was varied. Specifically, reducing the angle resulted in greater vertical displacement of the vocal fold and a smaller convergent-divergent spatial portion of the glottis. Associated with changes in vibration were decreases in glottal width and flow rate amplitudes and net airflow-to-tissue energy transfer as the inferior surface angle was reduced. The partially rigid model responses yielded evidence that changes in vibration of the fully-flexible models occurred primarily because of changes in structural, rather than aerodynamic, model responses.

3 INFLUENCE OF SUBGLOTTIC STENOSIS ON COMPUTATIONAL VOCAL FOLD MODEL FLOW-INDUCED VIBRATION

3.1 Introduction

While considerable work has been done to understand the glottis and supraglottis, understanding the role of the subglottal airway in phonation is a subject which is still under investigation. Of the relatively limited number of studies related to the subglottis, several have pointed to the geometry of the subglottis having an important effect on vibration of the vocal folds.

One of the areas most researched in relation to subglottal geometry has been the influence on phonation of subglottal acoustic resonance, which is largely governed by tracheal tube length. Austin and Titze (1997) first showed that involuntary register changes in the voice are related to tracheal resonance. Zhang et al. (2006a) also found evidence that register changes of synthetic models, along with other nonlinear phenomena in phonation such as frequency jumps and various classes of phonation onset and offset, can be produced solely on the basis of laryngeal interactions with the acoustical resonances of the subglottal system. The idea of acoustically driven phonation was given by these same authors (Zhang et al., 2006b), where synthetic vocal fold model vibration is coupled with the acoustic resonance of the subglottal tract and motion is described with a different eigenmode than aerodynamically driven vibration.

Other studies related to subglottal geometry have explored how subglottal shape influences vocal fold motion and other factors related to phonation. It was proposed by Li et al.

(2006a) that inferior vocal fold surface angle has little effect on intraglottal pressure distributions, which significantly influence vocal fold motion. As part of this thesis, a follow-up study was performed which showed that inferior vocal fold surface angle does directly affect vocal fold motion (see previous chapter). Specifically, changing the angle affects vertical displacement of the vocal fold and the convergent-divergent spatial portion of the glottis, resulting in changes in intraglottal pressures and net energy transfer. Grisel et al. (2010) recently found that changes in the subglottal shape after medialization thyroplasty surgery can significantly increase turbulence through the glottis, which can produce an abnormal voice, breathiness, and chaotic vocal fold vibrations. The turbulence can be reduced with medialization of the subglottis. While this prior research has provided insight into the influence of subglottal geometry in phonation, much more understanding is needed.

Subglottic stenosis (SGS) is a condition which alters subglottic geometry and can be associated with changes in voice quality. SGS is a narrowing of the airway in the subglottal larynx or upper trachea. In the majority of patients it is due to prolonged intubation and/or tracheotomy causing damage to the airway lumen. It can also occur congenitally, as a result of external trauma, from disease, or idiopathically (Giudice et al., 2003; George et al., 2005; Herrington et al., 2006). Symptoms regularly include respiratory problems such as dyspnea, stridor, and croup (Poetker et al., 2006; Bailey et al., 2003; Lesperance and Zalzal, 1998), but the voice is also sometimes affected and presents as hoarseness and/or dysphonia (Poetker et al., 2006; Giudice et al., 2003). Symptoms generally worsen as the severity of the stenosis increases.

When diagnosed, SGS is typically measured by percent occlusion (blockage) of the airway and classified by the Myer-Cotton grading scale (Grade I – 0-50%; Grade II – 51-70%; Grade III – 71-99%; Grade IV – 100% occlusion) (Myer et al., 1994). Lower grades (Grade I or

mild Grade II) may require little to no treatment, but more severe cases require more prompt and extensive treatment. Initial treatment for such cases often involves tracheostomy (placement of a tracheal tube) in order to ease respiration, but when the airway is severely compromised surgery is required. While simple operations can be performed for Grades II and III, Grades III and IV call for open reconstructive surgeries, tracheal resection and partial cricotracheal resection being the most effective (Bailey et al., 2003; Herrington et al., 2006). These types of surgeries have been shown to further affect voice quality (Smith et al., 1993; Smith et al., 2008).

Understandably, research related to SGS has focused primarily on treatments that will effectively obtain the goals of restoring airway patency and decannulation (tube removal). A subject less studied in relation to SGS, however, has been the management of laryngeal function, particularly the voice. A number of studies have considered voice quality due to SGS before surgery (Zalzal, 1988; Cotton, 1991; Zalzal et al., 1993), but the purpose of the assessments was for simple comparison with postoperative voice quality, and, therefore, no detailed qualitative or quantitative data about voice quality in the patients were reported. Ettema et al. (2006) sought to quantify voice quality in SGS patients through a perceptual voice analysis. According to their assessment, roughly 50% of their SGS patients had moderately to extremely affected voice quality. However, the majority of these patients had other negative risk factors besides SGS that would contribute to poor voice quality, including multiple stenoses, vocal fold impairment, and previous airway surgery. Thus, it is unknown whether effects on the voice were due to the subglottic stenosis or other factors. Furthermore, some patients with higher grade stenoses retained normal voice quality, showing that SGS affects some voices and not others. Because of the uncertainty about the connection of SGS to voice quality, it is of interest to further study the subject.

While a few studies have modeled subglottic stenosis, none have explored the effect of SGS on vocal fold vibration. Three studies (Cebal and Summers, 2004; Brouns et al., 2007; Mihaescu et al., 2008) have modeled the airway with SGS, defining three-dimensional geometry from human image data sets and performing computational simulations of respiratory airflow. Brouns et al. (2007) parametrically varied the severity of the stenosis. However, these studies focused solely on the effects of SGS on respiration and did not include vocal fold vibration.

This study investigates how varying subglottal geometry due to SGS affects vocal fold vibration. Vocal fold vibration is simulated using a two-dimensional finite element fluid-structure interaction model. Parametric changes to subglottal geometry are made by varying the severity of an idealized subglottic stenosis. Such a model makes it possible to identify effects of the stenosis itself, absent other contributing factors.

3.2 Methods

3.2.1 Stenosis Definition

The subglottic stenosis used in this study was approximated from computed tomography (CT) data and defined mathematically (Figure 3-1). A CT scan of a patient with subglottic stenosis was obtained from the University of Utah School of Medicine. The scan images had a pixel size of 0.45×0.45 mm in the transverse plane with 2 mm spacing between images. Twelve images, starting approximately at the inferior edge of the vocal folds and extending inferiorly through the stenosis to where the trachea returned to an approximately constant cross-section, were used to define the stenosis. The images were imported into MATLAB where code was executed to approximate each luminal cross section with an ellipse. The major and minor radii of each ellipse were determined, from which the elliptical area (A_e) of each cross section was

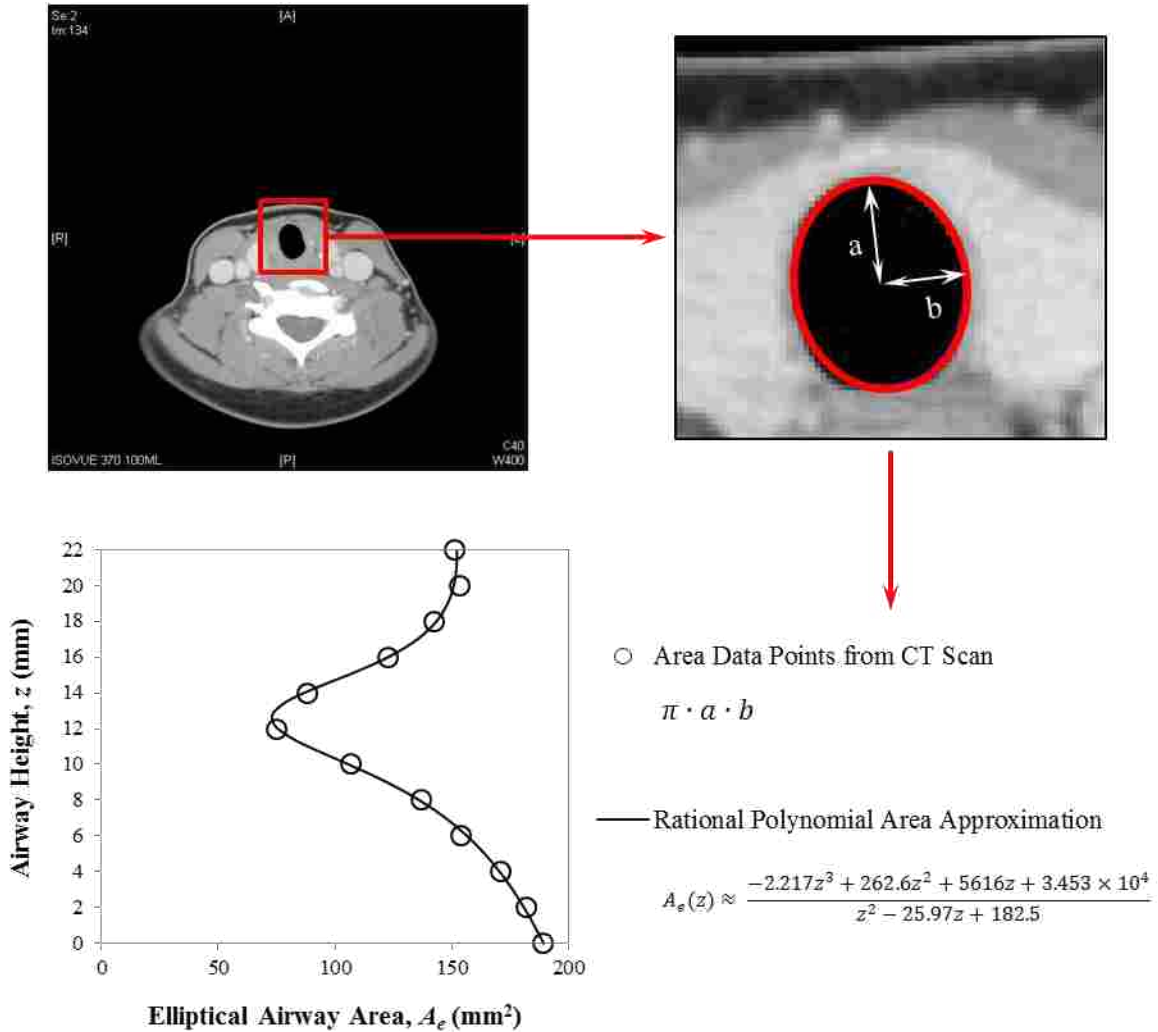


Figure 3-1. Schematic of stenosis definition process. Using CT scan images of a patient with SGS, the luminal cross-section was approximated with an ellipse, the elliptical area was calculated, and a rational polynomial curve was fit to the area data points to mathematically define the stenosis.

calculated. A rational polynomial curve was fit to the area data points in order to create a mathematical definition of the stenotic airway area as a function of distance along the airway.

The rational polynomial approximation was

$$A_e(z) \approx \frac{-2.217z^3 + 262.6z^2 + 5616z + 3.453 \times 10^4}{z^2 - 25.97z + 182.5}, \quad (3-1)$$

where z here refers to the inferior-superior height of the airway and ranges from 0 (inferior) to 22 (superior) mm for the profile. A_e is expressed in mm^2 .

Because the stenosis was incorporated into a two-dimensional computational model, the elliptical area profile was converted to an equivalent profile for a rectangular airway using a characteristic depth d and a stenosis profile height h . Figure 3-2 gives a schematic of the conversion with dimension definitions. First, the depth d of the rectangular airway was solved for. This process was performed as follows: (1) Set elliptical area and rectangular area equal at superior end of airways; (2) Let height and minor radius be equal ($b_0 = h_0$); (3) Solve for d .

$$(1) \pi a_0 b_0 = 2h_0 d \rightarrow (2) \pi a_0 b_0 = 2b_0 d \rightarrow (3) d = \frac{\pi a_0}{2} \quad (3-2)$$

Substituting in the major radius value from the superior-most CT scan data point ($a_0 = 8.826$) gives $d \approx 13.86$ mm. This became the characteristic depth that was held constant and used for calculating the stenosis profile height (h). The profile height was found by setting the elliptical area approximation and rectangular area equations equal to each other and solving for h , as follows:

$$A_e = 2hd \rightarrow h = \frac{A_e}{2d} \quad (3-3)$$

where A_e is the rational polynomial area curve (Equation 3-1) and d is the characteristic depth found above. The resulting stenosis profile found by h was similar in size and general shape to the stenotic portion of the airway segmented from the CT scan (Figure 3-3). The stenosis profile adapted for the two-dimensional airway was more narrow because it only reduced area in one dimension rather than two as in the elliptical airway.

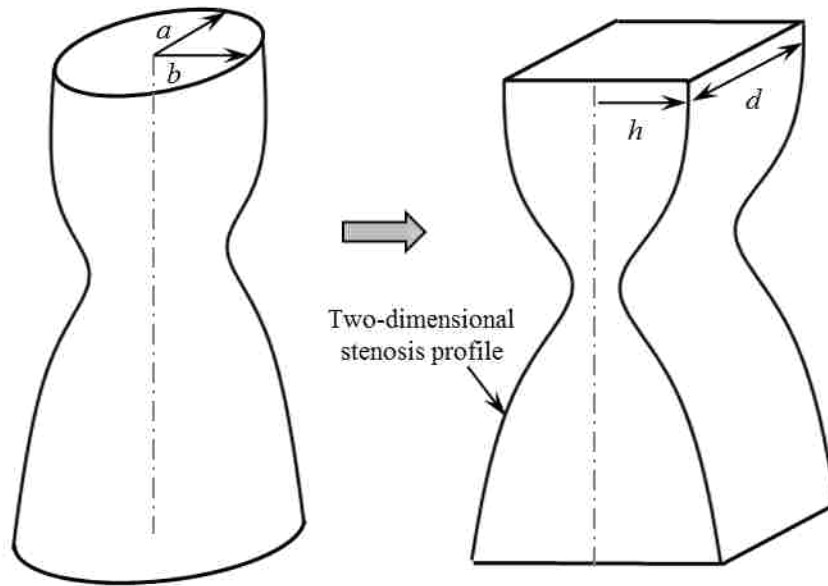


Figure 3-2. Schematic of conversion from elliptical airway area approximation to stenosis profile for a rectangular airway with stenosis profile height h and characteristic depth d .

The stenosis profile was further scaled so that the height at the superior end of the profile matched the height of previously used two-dimensional computational models just below the vocal folds (8.45 mm). The scaling factor was found to be $K = 1.5404$. Data points for profile height were found by Equation 3-3 at 0.5 mm increments of airway length (z), and the resulting h values at these points were multiplied by K to scale them. The corresponding z values were then also scaled by K , giving data points that were used to define the stenosis profile in a two-dimensional computational model.

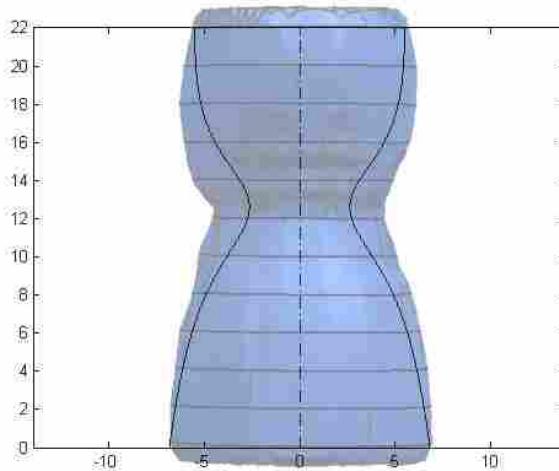


Figure 3-3. Stenosis profile adapted for two-dimensional airway (plot) compared to three-dimensional segmentation of actual stenosis from CT images (blue model).

3.2.2 Parameterization

The stenosis profile was parameterized and varied to create several severities of stenosis. Figure 3-4 gives details of the parameterization. Before parameterization, the coordinates of the stenosis profile data points were converted to the coordinate system that was to be used in the computational model, where $h = 0$ was defined at the superior-most point of the profile. Thus, h is defined in this new coordinate system in the figure. The stenosis height at the peak of the stenosis (h_{pk}) was determined by percent occlusion, or the percentage of the airway cross-sectional area that was obstructed by the stenosis. All other points along the profile were

parameterized by a ratio of the height at that point in the original (unparameterized) profile (h_0) to the original peak height ($h_{pk,0}$), multiplied by the parameterized peak stenosis height (h_{pk}), given by

$$h = \frac{h_0}{h_{pk,0}} h_{pk} \quad (3-4)$$

Downstream of the stenosis peak, the parameterized heights were referenced to the superior-most point of the stenosis ($h = 0$ mm), whereas upstream they were referenced to the inferior-most point ($h = -2.06$ mm). This allowed the parameterization to function properly upstream of the peak with both positive and negative height coordinates.

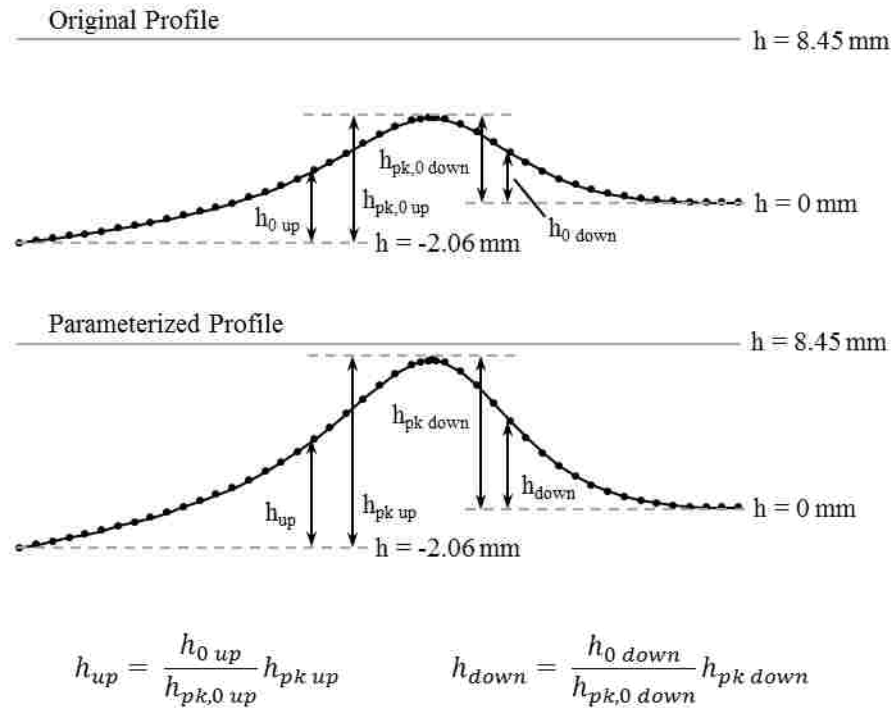


Figure 3-4. Parameterization of stenosis profile based on ratio of height at each point to peak height from original profile.

Six severities of stenosis were used for this study. A 0% case corresponded to no stenosis or a “normal” airway. 30%, 60%, and 90% cases corresponded to stenosis grades I, II, and III, respectively, according to the Myer-Cotton grading scale (Myer et al., 1994). Two additional grade III stenosis cases, 95% and 99%, were created in anticipation of more sensitive changes in this region of high stenosis severity.

3.2.3 Computational Modeling and Simulation

In order to model phonation with SGS, the stenosis profile was incorporated into a computational model simulating two-dimensional air flow through the vocal tract. The computational model was the same ADINA fluid structure interaction model that was developed for the inferior angle study presented in the previous chapter (Section 2.2). There is found a detailed description of the geometry, material properties, and numerical methods used for the model (Figure 2-2). This model had an inferior surface angle of 40° . The only variation to this model was that the fluid domain included a longer upstream tract (inlet was 35.7 mm upstream of inferior-most vocal fold point) with a stenotic region in order to simulate an airway with SGS. The parameterized stenosis profile was incorporated into the wall of the fluid domain directly upstream of the vocal fold, connecting to the inferior-most point on the inferior surface of the vocal fold profile. Number of nodes remained constant in all the cases at around 45,000, but meshing was biased in the stenotic region (finer mesh for higher severity) in order to maintain reasonable aspect ratios in the narrowest region and resolve flow features across the stenosis.

Six models bearing the above mentioned degrees of stenosis (0%, 30%, 60%, 90%, 95%, and 99%) were created (Figure 3-5). The vibratory response of the solid model to fluid flow was

simulated in ADINA for 6000 time steps with a time step size of 2.5×10^{-5} s, at inlet pressures of 300, 600, and 900 Pa for each case of stenosis.

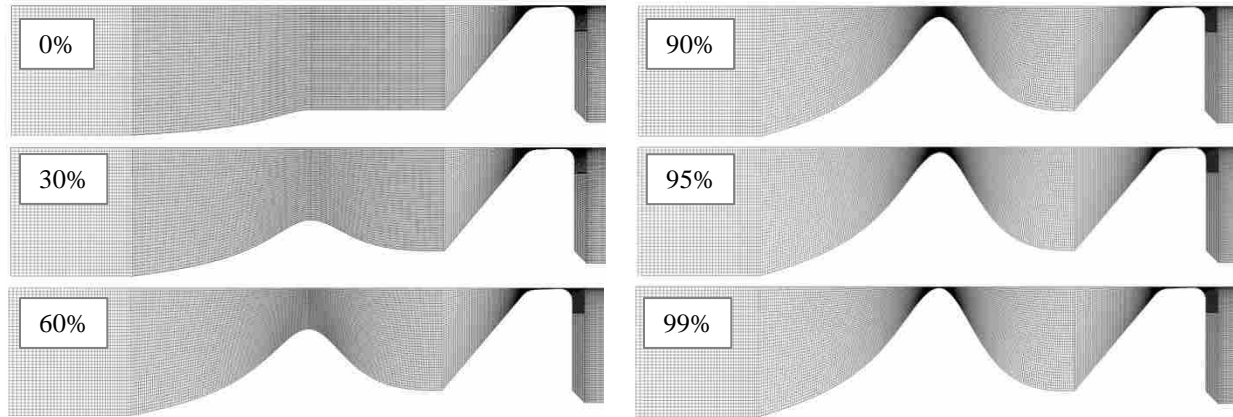


Figure 3-5. Fluid domains of FSI model for each severity of stenosis.

3.2.4 Verification

As with the inferior angle study, simulations were performed on the SGS model to ensure that the results were reasonably independent of grid density, time step size, and convergence criteria. These were performed using the normal (0%) case with a 600 Pa inlet pressure. The study was performed in the same manner as described for the inferior angle study (see previous chapter). Results were again compared by analyzing minimum glottal width waveforms. Figure 3-6 includes results of the grid-independence study; in this case, the waveforms from the model grid simulations and the grid-doubled simulations were deemed to be satisfactorily close. Results of the time step size and convergence criteria independence studies (Figure 3-6) yielded considerably less change.

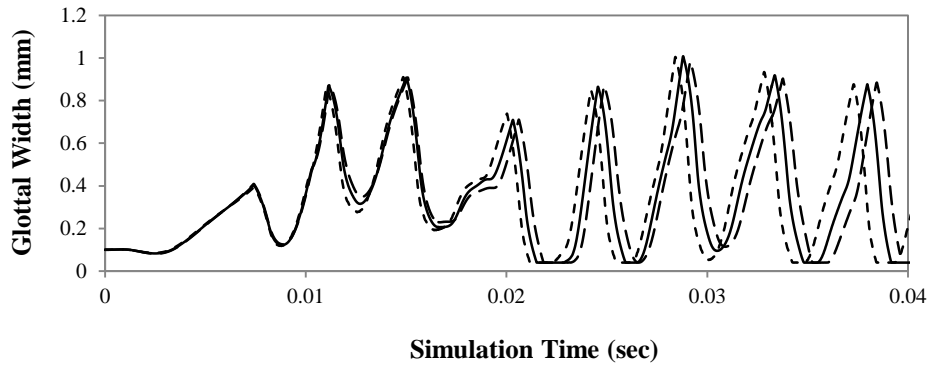


Figure 3-6. Results of the grid-independence study. ——— Model grid density, - - - - - Grid-halved density, - . - . - Grid-doubled density

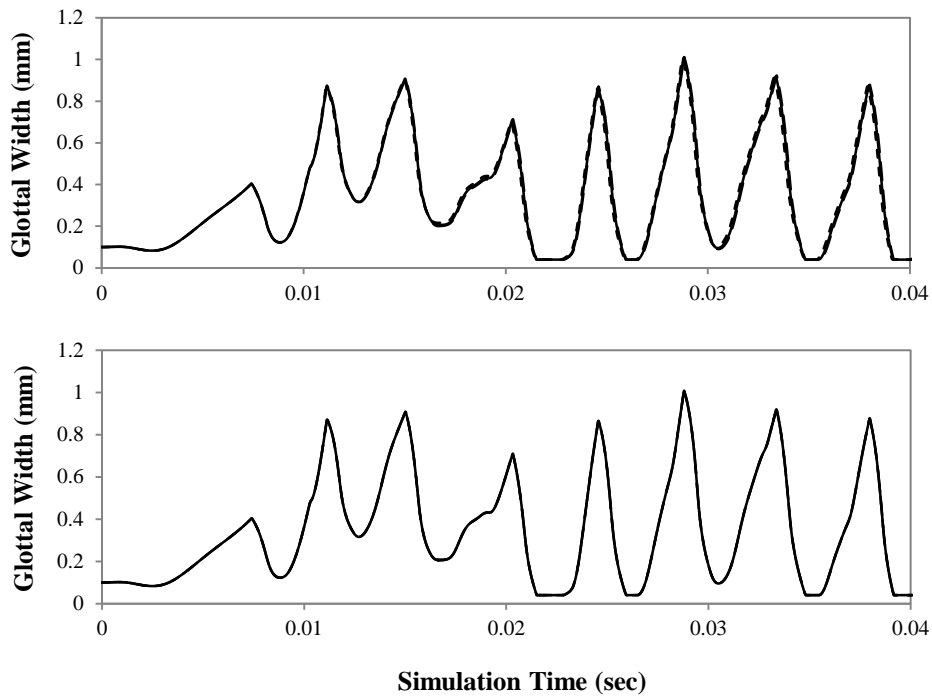


Figure 3-7. Top: Results of the time step independence study. ——— Model time step, - - - - - Doubled time step, - . - . - Halved time step; Bottom: Results of the convergence criteria independence study. ——— Model criteria, - - - - - Criteria increased by factor of 10, - . - . - Criteria decreased by factor of 10.

3.3 Results

3.3.1 Overview of Model Responses

Figure 3-8 shows model motion for the normal, 60%, 95%, and 99% cases at 600 Pa. Eight phases at even intervals of the oscillatory cycle are shown. Phase times are normalized by the oscillation period T . Motion profiles for the normal case (Figure 3-8, first column) showed that the glottis was “closed” or at its maximum closure at $t/T = 0$ and 0.125 . Here the point of contact was moving superiorly in a wavelike fashion, and the glottis began to shift to a convergent shape. The next three phases captured glottal opening with a convergent glottal profile. At $t/T = 0.625$ the glottis was at its maximum opening, and the last two phases were during glottal closing where the glottal profile alternated to a divergent profile. As the motion is followed throughout the cycle wavelike motion resembling a mucosal wave is apparent across the medial surface.

Motion was essentially identical for the 0%, 30%, 60%, and 90% cases at 600 Pa. The 60% case is shown for comparison in Figure 3-8 (second column). The 95% case (Figure 3-8, third column) exhibited slightly different motion in that it appeared that glottal opening occurred more quickly so that the glottis reached its maximum opening sooner (somewhere around $t/T = 0.5$). At $t/T = 0.625$ the glottis was somewhat divergent, indicating that it was in the closing phase by this point. At $t/T = 0.75$ the glottis displayed a noticeably flatter divergent profile. Vertical deformation of the model for the 95% case appeared somewhat less than the normal case, as indicated by the space between the furthest right part of the profile and the plot border. All of these changes, however, were very subtle. The 99% case (Figure 3-8, last column), on the other hand, yielded significantly different motion than any of the other cases. The glottis actually appeared to stay closed longer (until $t/T = 0.25$), but then it clearly reached its point of maximum

opening sooner at $t/T = 0.5$. It then closed with a more rounded divergent profile than the other cases. Both the amplitude of the glottal opening and the vertical deformation of the model were visibly less for the 99% case.

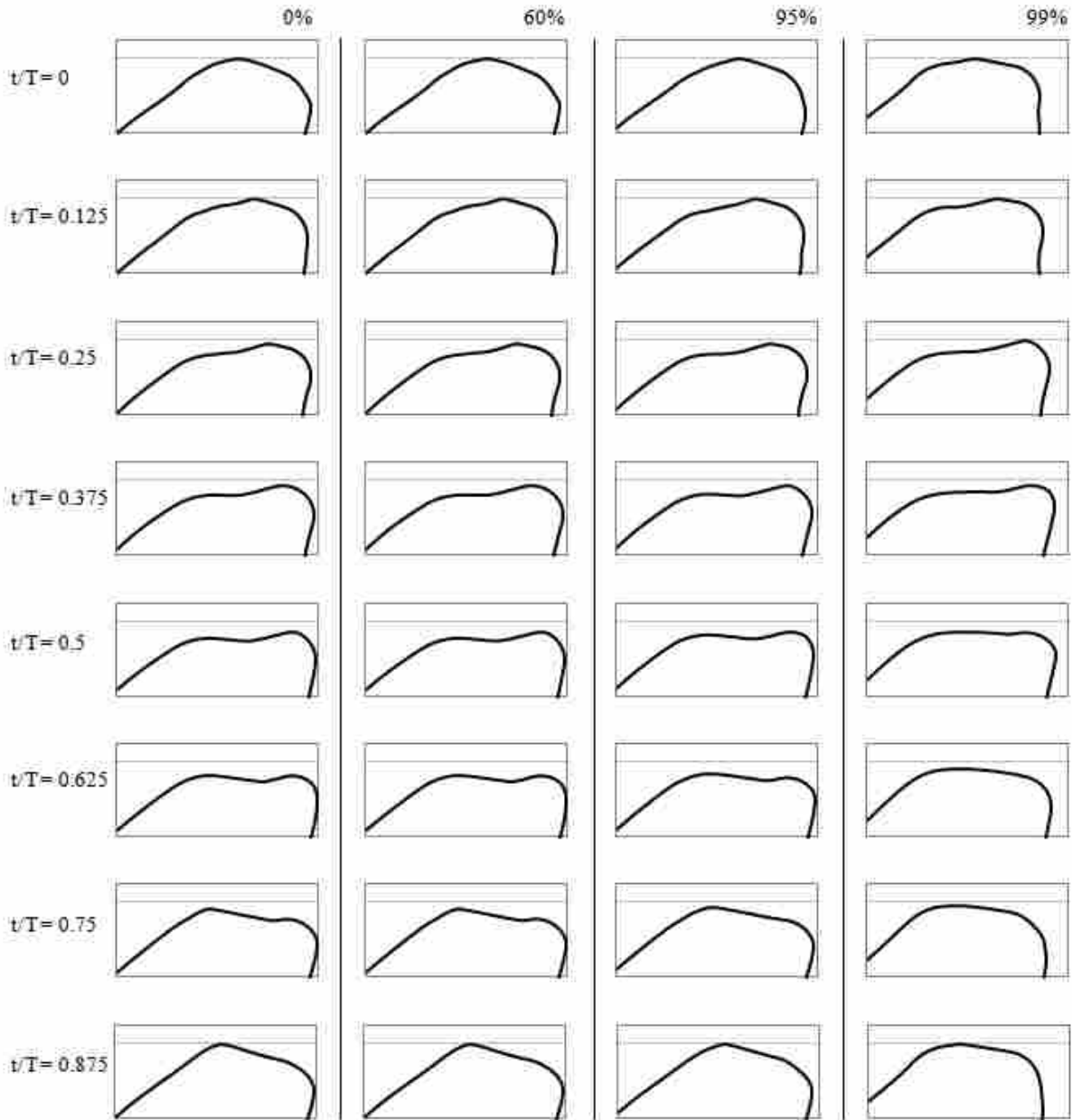


Figure 3-8. Profiles showing model motion for the normal (0%), 60%, 95%, and 99% stenosis cases at 600 Pa inlet pressure. Images are zoomed to show just the medial portion of the model.

Model oscillation frequency, averaged over ten steady-state cycles, is shown for all cases in Figure 3-9. For the lesser severities of stenosis, the frequency remained fairly constant at about 201, 229, and 246 Hz with inlet pressures of 300, 600, and 900 Pa, respectively. Frequency was not at all affected until the stenosis severity reached at least 90%. Between 90% and 95% still no appreciable change occurred, as the frequency only dropped at most about 10 Hz for any of the inlet pressures. Frequency decreased more considerably between 95% and 99% stenosis with large drops of around 20 Hz and 45 Hz at 600 and 900 Pa, respectively.

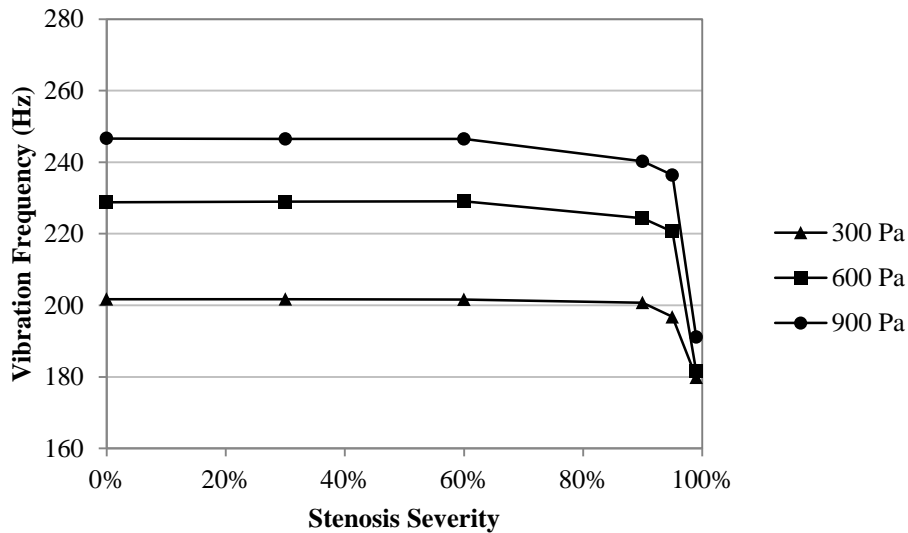


Figure 3-9. Model oscillation frequency for all stenosis cases at three inlet pressures.

3.3.2 Glottal Width

Glottal width was measured by calculating twice the minimum distance between the medial surface and the symmetry line. Figure 3-10 plots glottal width over a steady-state cycle for all cases and inlet pressures. At an inlet pressure of 300 Pa, glottal width waveforms for the

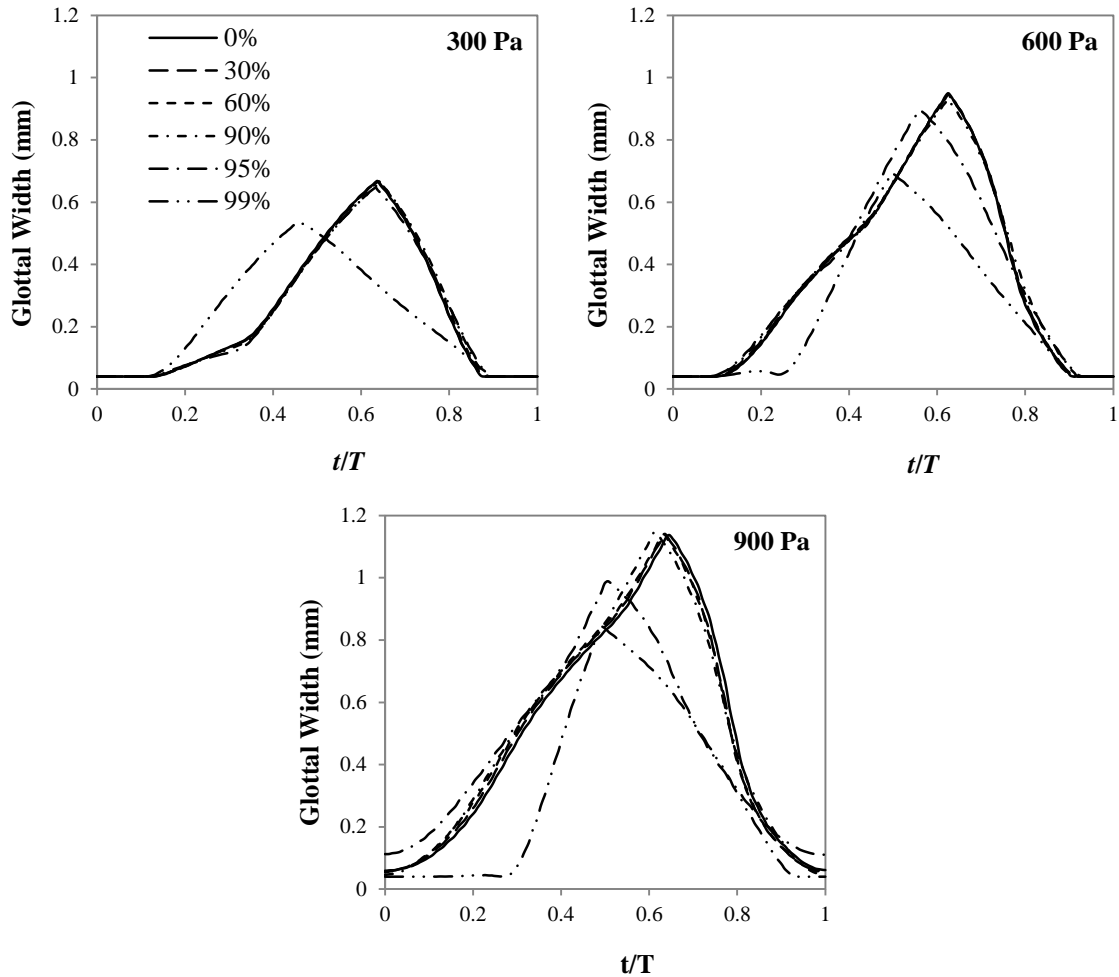


Figure 3-10. Glottal width waveforms over a normalized steady-state cycle for all stenosis cases at 300, 600, and 900 Pa inlet pressures.

0% to 95% cases were essentially the same as the normal case throughout the entire cycle. Peak values were about 0.67 mm. The 99% case, however, showed a peak that was close to 20% lower in magnitude and that occurred considerably sooner in the cycle. At 600 Pa, the 99% case again had a significantly lower peak glottal width (about 27% less) than the normal case, which peaked at about 0.95 mm. The peak glottal width, the point at which the model was at its maximum glottal opening, was at about $t/T = 0.5$, rather than $t/T = 0.625$ like the rest of the cases. The 95% case at 600 Pa also differed somewhat from the lesser severities with a 6% drop

in the peak and a shift in the location of peak glottal width. These results for both the 95% and 99% cases agree with the model behavior seen from the motion profiles. For an inlet pressure of 900 Pa, again only the 95% and 99% cases were affected. As with the results at 600 Pa, the differences between these and the normal case consisted of smaller peak glottal width values and shifts in where the peak occurred. The trend was increasing change with increasing stenosis severity. Here the peaks for the 95% and 99% cases dropped 13% and 26%, respectively, from the 1.14 mm maximum glottal width of the other cases. Minimum values for glottal width at 900 Pa showed that the 95% case did not close as much, while the 99% case was closed for a longer portion of the cycle than the cases of lesser severity.

3.3.3 Flow Rate

Flow rate was measured by taking twice the integral of velocity across the glottal jet and multiplying by 2.135 cm, corresponding to the scaled characteristic depth ($K \cdot d$, ref. section 3.2.1). Flow rate waveforms, corresponding to the same cycles as the glottal width plots, are shown in Figure 3-11. For the most part the flow rate behavior followed closely the patterns of the glottal width waveforms. As with glottal width, significant decreases in peak flow rates occurred for the 99% case at 300 Pa, and for the 95% and 99% cases at 600 and 900 Pa. The decreases in peak flow rates were substantially greater for flow rate waveforms than for glottal width. Flow rate was more sensitive to the stenosis, as evidenced by slight decreases in the peak flow rate which occurred for the 95% case at 300 Pa and 90% case at 600 and 900 Pa. Also seen in the glottal width waveforms, the flow rate peaks for the differing cases occurred earlier in the cycle than for the normal case and lower severities of stenosis. One observation of interest not seen with glottal width is that the flow rate waveforms for the 99% cases take on a very different

shape than the waveforms for the other cases. Additionally, the 95% case at 900 Pa showed high minimum flow rates compared to the other cases, which were all grouped around the same minimum values.

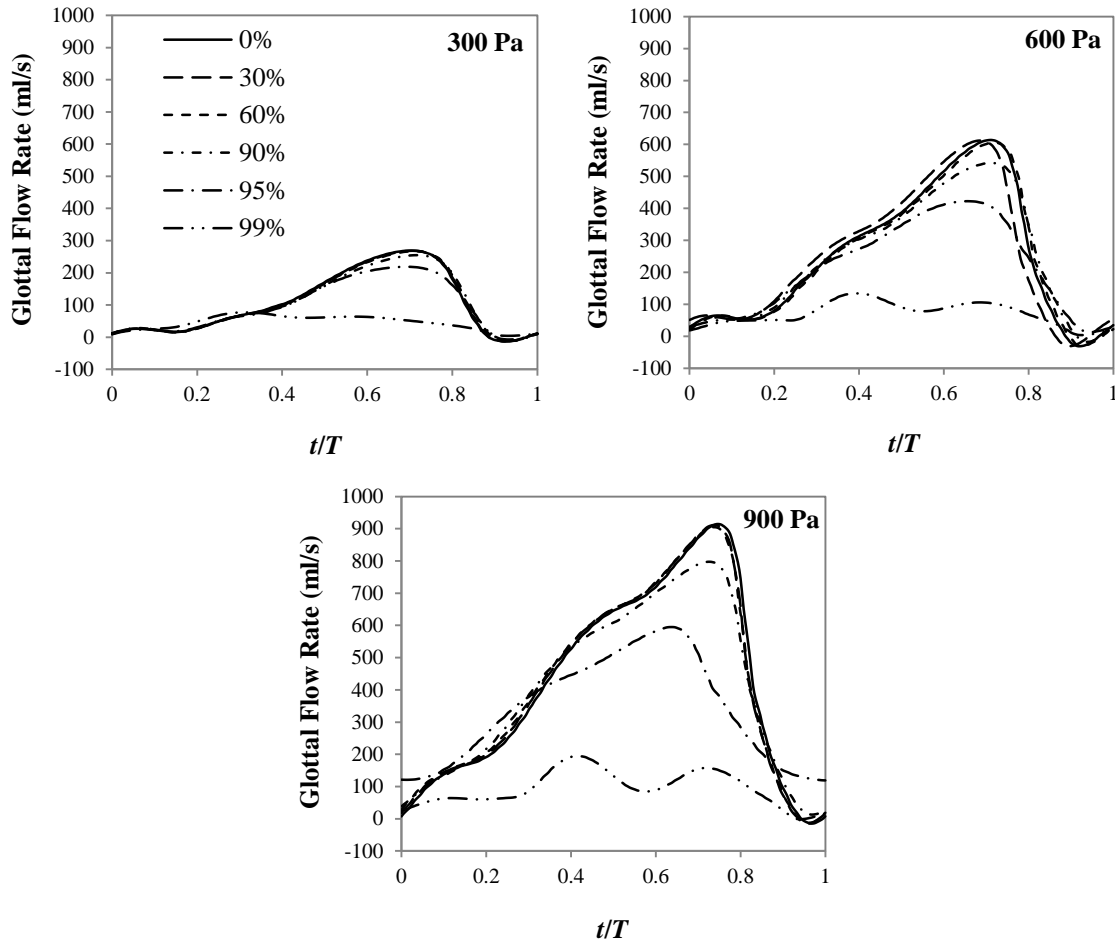


Figure 3-11. Glottal flow rate waveforms over a normalized steady-state cycle for all stenosis cases at 300, 600, and 900 Pa inlet pressures.

Maximum flow declination rate (MFDR), defined as the slope of the flow rate waveform at its steepest descent, was noticeably different for the cases which deviated from the normal case (Figure 3-11). Figure 3-12 quantifies how MFDR changed with stenosis severity. MFDR

was fairly steady up until 90% stenosis, where it began to decrease. The decrease in MFDR became greater with increasing stenosis severity at each inlet pressure, and the amount of change between severities also increased as pressure increased. At both 600 and 900 Pa inlet pressure the decreases in MFDR are substantial as they drop an order of magnitude by the 95% case.

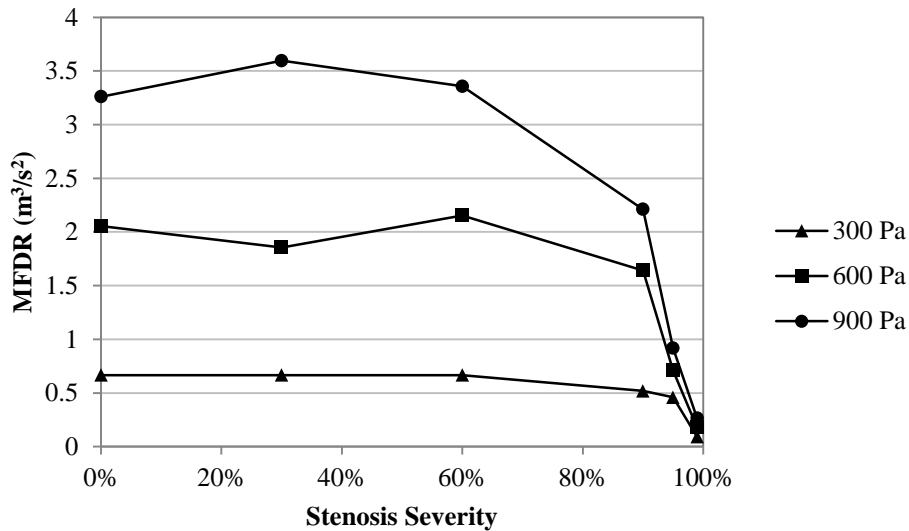


Figure 3-12. Maximum flow declination rate for each stenosis case at three inlet pressures.

3.3.4 Flow Resistance

Airway resistance was considered as a means to compare the effects of the stenosis with the effects of the glottis on the flow. Airflow resistance is calculated as a ratio of the driving pressure to the flow rate ($\Delta P/Q$). The driving pressure in this case was taken as the pressure difference across a section of airway (the stenotic region or the glottis), and the flow rate used for

both sections was that measured directly in the glottis. Resistance here was also normalized by dividing the pressure difference by the inlet pressure, and the instantaneous flow rate by the average flow rate, as follows:

$$R^* = \frac{\Delta P / P_{in}}{Q / \bar{Q}} \quad (3-5)$$

Average normalized resistance R^* for all cases is given in Figure 3-13. Resistance across the stenosis showed a steady increase with increasing stenosis severity, gaining two orders of magnitude by 90% stenosis. Resistance across the glottis, on the other hand, showed essentially the same resistance until 90% or greater stenosis severities, where it decreased as stenosis severity increased. At 90% and 95% resistance values across the stenosis and glottis are more or less on the same order of magnitude, and at 99% the two resistances are very close in magnitude.

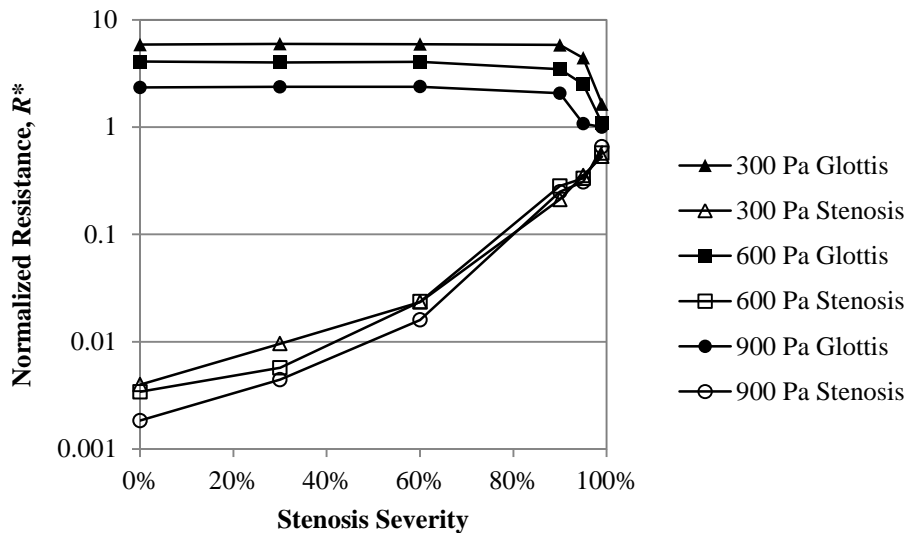


Figure 3-13. Average normalized resistance R^* across the glottis and across the stenosis for all stenosis cases at three inlet pressures. Note the logarithmic y scale.

3.3.5 Subglottal Flow Visualization

Subglottal flow was visualized in order to characterize the effects of the stenosis on the flow. Figures 3-10 through 3-12 show important flow features for a few different cases. Note the different velocity scale on each figure. The normal (0%) case (Figure 3-14) exhibited smooth, laminar flow through most of the oscillatory cycle with a thin recirculating layer along the outer wall of the airway as the flow was obstructed by the closing of the glottis. The visualizations revealed that flow in the subglottis became more disturbed as the severity of the stenosis increased. At 60% stenosis (Figure 3-15) the differences were that the recirculating layer during glottal closing was significantly thicker, taking up most of the airway when the glottis was

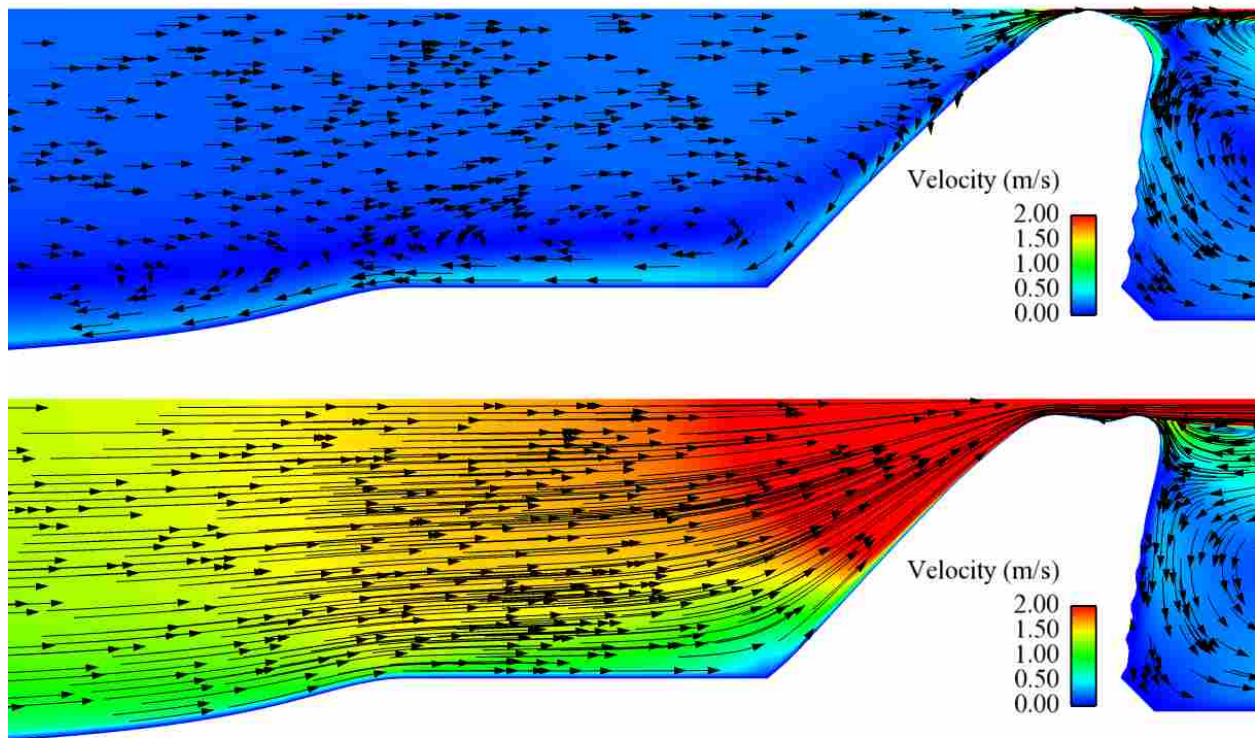


Figure 3-14. Visualization of subglottal flow velocity magnitude (color) and direction (arrows) for the normal (0% stenosis) case at 600 Pa. Upper image shows flow at $t/T \approx 0$ (closed glottis). Lower image shows flow at $t/T \approx 0.6$ (around maximum glottal opening).

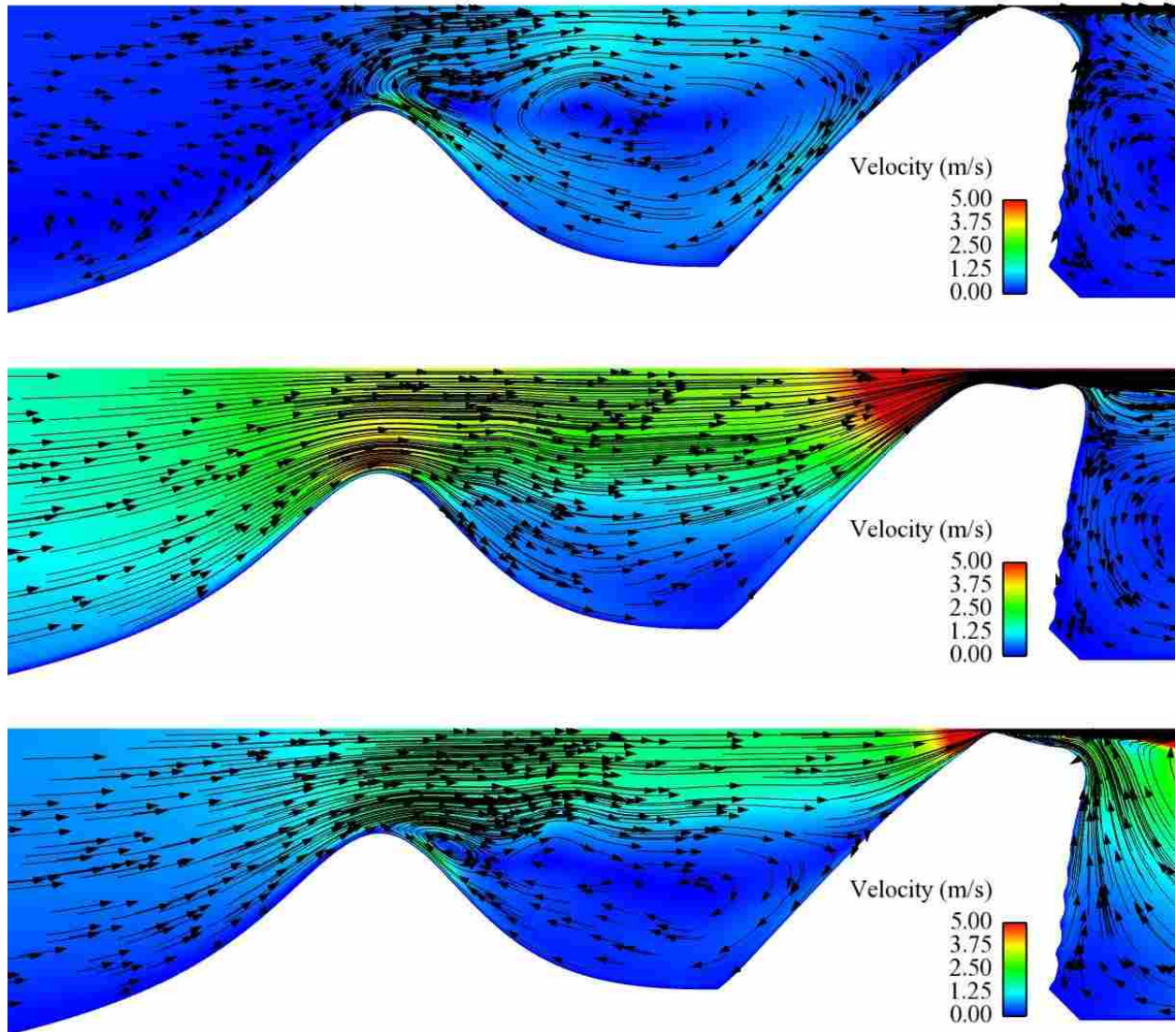


Figure 3-15. Visualization of subglottal flow velocity magnitude (color) and direction (arrows) for the 60% stenosis case at 600 Pa. Upper image shows flow at $t/T = 0$ (closed glottis). Center image shows flow at $t/T = 0.625$ (maximum glottal opening). Lower image shows flow at $t/T \approx 0.82$ (during glottal closing).

closed, and the velocities in the subglottis, particularly through the stenotic region, increased to around 5 m/s. Another important flow feature was a vortex that appeared just past the stenosis peak during glottal closing. It remained fairly stationary without traveling downstream and eventually dissipated as the glottis reopened. In the 95% case (Figure 3-16) even more significant change in the flow was seen. Velocities increased to values in the range of 20 m/s,

recirculation existed during the entire cycle, and a stronger vortex in the flow was created as the flow separated off the stenosis peak. The vortex in this case appeared during the opening phase and traveled downstream, dissipating somewhat but still remaining present throughout the cycle. These flow features were also present and similar in the 90% and 99% cases.

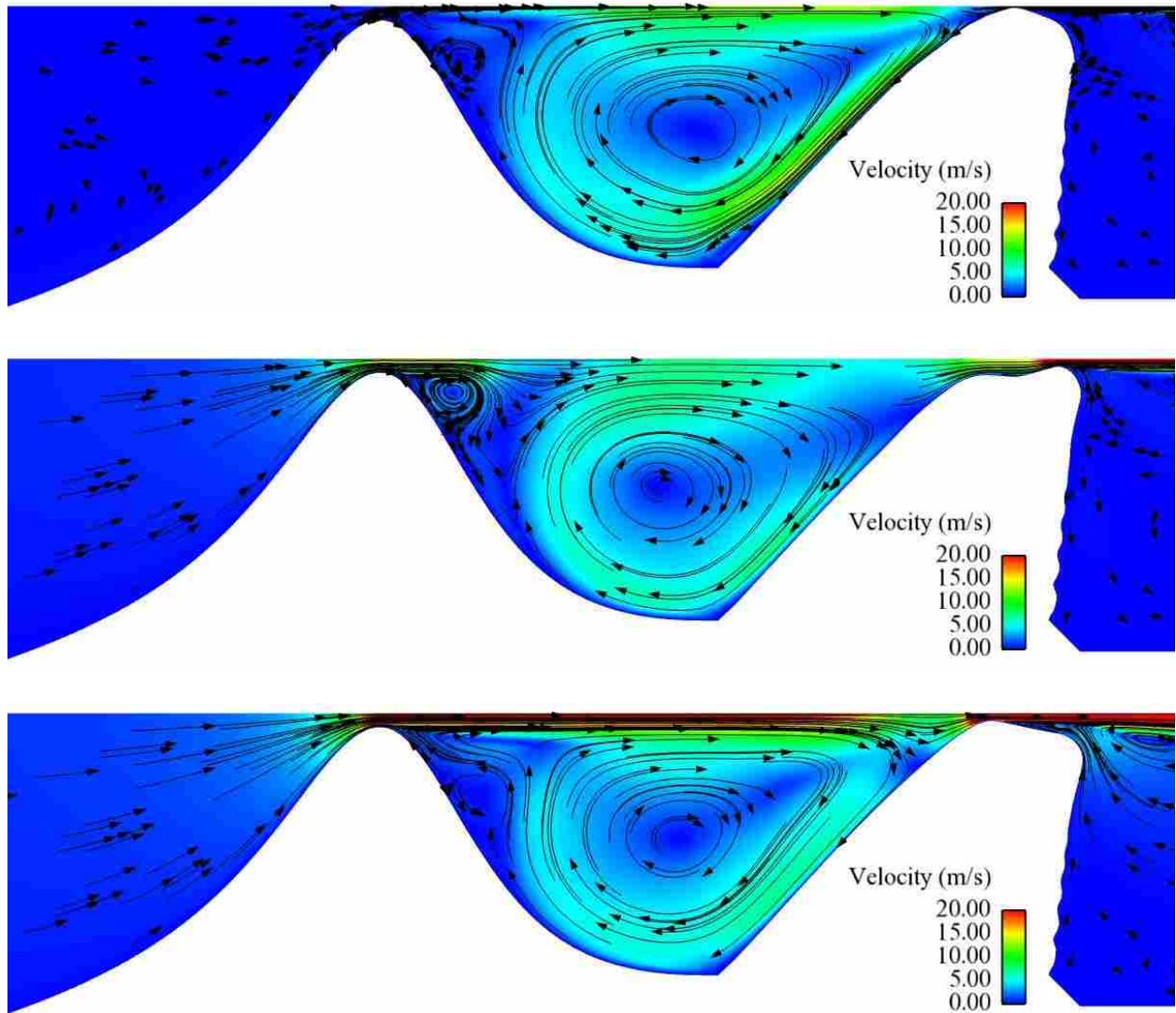


Figure 3-16. Visualization of subglottal flow velocity magnitude (color) and direction (arrows) for the 95% stenosis case at 600 Pa. Upper image shows flow at $t/T = 0$ (closed glottis). Center image shows flow at $t/T = 0.375$ (during glottal opening). Lower image shows flow at $t/T \approx 0.75$ (during glottal closing).

3.4 Discussion

As was discussed in the previous chapter the results of this FSI model again generally displayed motion that was similar to actual vocal fold vibratory motion, including convergent-divergent glottal profiles and mucosal wave-like movement of the medial surface. Quantifiable values such as glottal width, flow rate, and frequency were in the range of those measured during human phonation.

The purpose of this study was to explore how the presence of subglottic stenosis affected vocal fold vibration. The results showed that, with stenosis severities of about 90% and above, vibration of the vocal fold model was indeed altered. In particular, glottal width, flow rate, frequency, and vertical deformation of the model tended to decrease with increasing stenosis severity. Flow resistance across the glottis also decreased with stenosis above 90%, becoming very comparable in magnitude to the trans-stenosis resistance. These changes were more sensitive at higher inlet pressures (i.e., change was introduced at a lesser severity of stenosis as inlet pressure increased).

The main contributor to these changes may be a pressure drop across the stenosis. The constricted flow path created by the stenosis will cause a decrease in fluid pressure according to Bernoulli's principle. The fact that pressure drops across the stenosis is also evidenced by the flow resistance results. The steady increase in flow resistance across the stenosis is due to an increasing pressure difference across the stenosis as the degree of stenosis severity increases. As pressure decreases across the stenosis, it also decreases the pressure difference across the glottis. At higher severities of stenosis, the decrease in pressure difference across the glottis is significant enough in relation to flow rate that it causes glottal resistance to decrease substantially. A decrease in the pressure gradient across the glottis will also decrease the driving

force of the vocal folds, thus contributing to the smaller glottal width and lesser vertical deformation of the vocal fold model.

The decrease in frequency is likely connected with the lower amplitude motion. Because the model had non-linear stress-strain properties, it became stiffer the more it was deformed. With decreased deformation the effective stiffness of the model was less, resulting in a lower natural frequency. Thus, it vibrated at a lower frequency. This idea also explains why the frequency of the normal models increased with increasing inlet pressure which caused greater model deformation.

The changes in model vibration suggest that the voice can be affected by the presence of subglottic stenosis. Certain factors are a good measure of how the voice may change. First, vibration frequency is a key characteristic of the sound of the voice. With stenosis severities of about 95% and above, changes in frequency were substantial enough to be recognized as a change in pitch of the voice. In addition, MFDR is related to vocal acoustic power (Titze and Sundberg, 1992; Titze, 2000) and intensity (Titze, 2000; Titze, 2006). The considerable decrease in MFDR for high stenosis severities would possibly result in a lowered intensity of the voice or difficulty in speaking loudly. Interestingly, this has also been the result in patients who have undergone resection surgery for SGS (Grillo et al., 2003), but it is uncertain if there is any connection.

While distinct changes in vocal fold vibration did occur, it is significant that essentially no changes were seen until at least 90% of the airway was occluded. This means that only patients with the most severe cases of SGS would experience an affected voice. This may support the idea Ettema et al. (2006) put forth that other negative factors associated with SGS, such as multiple stenoses, vocal fold motion impairment, and previous airway surgery play a

more significant role in affecting the voice in SGS patients than the stenosis itself. Conversely, it may also be the case that the low sensitivity is due to factors specific to this model. For example, model geometry and material properties greatly affect vibratory behavior. Therefore, if these factors were changed, specifically to better match the geometry and material properties of the human vocal folds, different results may be observed. In addition, varying the position and properties of the stenosis may result in more or less model sensitivity. A stenosis closer, or even connected to, the vocal folds may affect their vibratory behavior much more than the one used here. Using a material model for the stenosis, rather than a rigid profile, or varying geometry (e.g., three-dimensional or asymmetrical) could also yield different results. Because of the uncertainty which remains this is a subject which needs further exploration, including studies using human subjects, excised larynges, and experimental models in order to be better understood.

Disturbances in subglottal flow were apparent with 60% stenosis and increased with increasing stenosis severity. The disturbed flow features included recirculation, vortex shedding, and increased velocities. This is consistent with the findings of previous research that studied the effect of SGS on respiration, which showed decreased pressure, turbulent flow, and increased shear stress in the stenotic region (Cebal and Summers, 2004; Brouns et al., 2007; Mihaescu et al., 2008). The presence of vortices and other turbulence in glottal flow can contribute to hoarseness or breathiness in the voice. However, these disturbances in the subglottal flow did not seem to have any connection to changes in model vibration.

3.5 Conclusions

A two-dimensional, fluid-structure interaction model was used to simulate the flow-induced vibration of the vocal folds with varying degrees of subglottic stenosis. The results showed that the presence of stenosis of up to 60% did not alter vocal fold vibration, while a stenosis of 90% or greater influenced several factors related to vocal fold vibration. Vertical model displacement, glottal width amplitude, and flow rate amplitude decreased with increasing stenosis severity above 90%. The model sensitivity to subglottic stenosis increased with increasing pressure, and changes in vibration correlated with changes in glottal flow resistance. Subglottic stenosis caused a substantial pressure drop in the subglottis, which may be a large contributing factor to other parameters, such as resistance and glottal width, being affected. Stenosis caused significant disturbances in subglottal flow with as low as 60% stenosis, which increased with increasing stenosis severity. The disturbed flow did not appear to affect vibration. High severities of stenosis led to significant decreases in frequency and maximum flow declination rate, suggesting that subglottic stenosis may cause changes in sound and power of the voice.

4 INFLUENCE OF SUBGLOTTIC STENOSIS ON SYNTHETIC VOCAL FOLD MODEL FLOW-INDUCED VIBRATION

4.1 Introduction

In the introduction to Chapter 3, previous work regarding the subglottis is reviewed and the relevance of studying the effect of subglottic stenosis on vocal fold vibration is discussed (see 3.1). While a few studies focused on computational models of SGS have been performed, no work has been performed to study SGS using an experimental setup.

In this study the effect of SGS on vocal fold vibration in a synthetic model was explored. The SGS was incorporated into the subglottal duct of an experimental airway setup and varied parametrically to determine how it influenced the vibration of silicone vocal fold models. The work presented in this chapter is a preliminary experimental complement to the computational SGS study in the previous chapter.

4.2 Methods

4.2.1 Stenosis Definition and Parameterization

The stenosis used for this study was defined using the same approximated profile as described in the previous chapter. Detailed methods for defining and parameterizing the profile are given there (3.2.1). In this study acrylic inserts with SGS profiles were fabricated and used to simulate stenosis in an experimental air flow duct, described in the next section.

4.2.2 Subglottal Duct

A subglottal duct (Figure 4-1) was custom designed for this study to be able to simulate varying severities of stenosis. A 15.24 cm tall rectangular duct was made with a clear acrylic front panel, clear acrylic sides, and an ABS plastic back panel. The front panel allowed for a coronal cross-sectional view of the airway. The airway at the bottom of the duct was 21.21 mm wide by 21.35 mm deep. This depth corresponds to the same scaled characteristic depth used in the computational stenosis work. The acrylic sides were approximately 10.5 cm tall.

Subglottic stenosis was created with acrylic inserts (see also Figure 4-1) which were CNC milled to create the stenosis profile shape for three cases of stenosis. The three cases created and studied here were 0%, 60%, and 95%. These created a stenotic profile in the coronal plane that had a uniform anterior-posterior cross section. No stenosis was present in the sagittal plane.

The stenosis inserts were incorporated into the subglottal duct above the side panels. The inserts and side panels of the subglottal duct fit together with paired notches, which aligned the stenosis profile with the rest of the duct. The inserts were held in place by housing the duct and inserts with clear acrylic plates on the top and bottom, connected by four columns on the corners of the plates. The top plate fit around the top of the inserts and was grooved to mate with the ridge on the top of the inserts and hold them at the proper distance apart. The top plate also had holes used to connect the vocal fold models to the top of the subglottal duct. The bottom plate was used to secure the duct to an air flow setup.

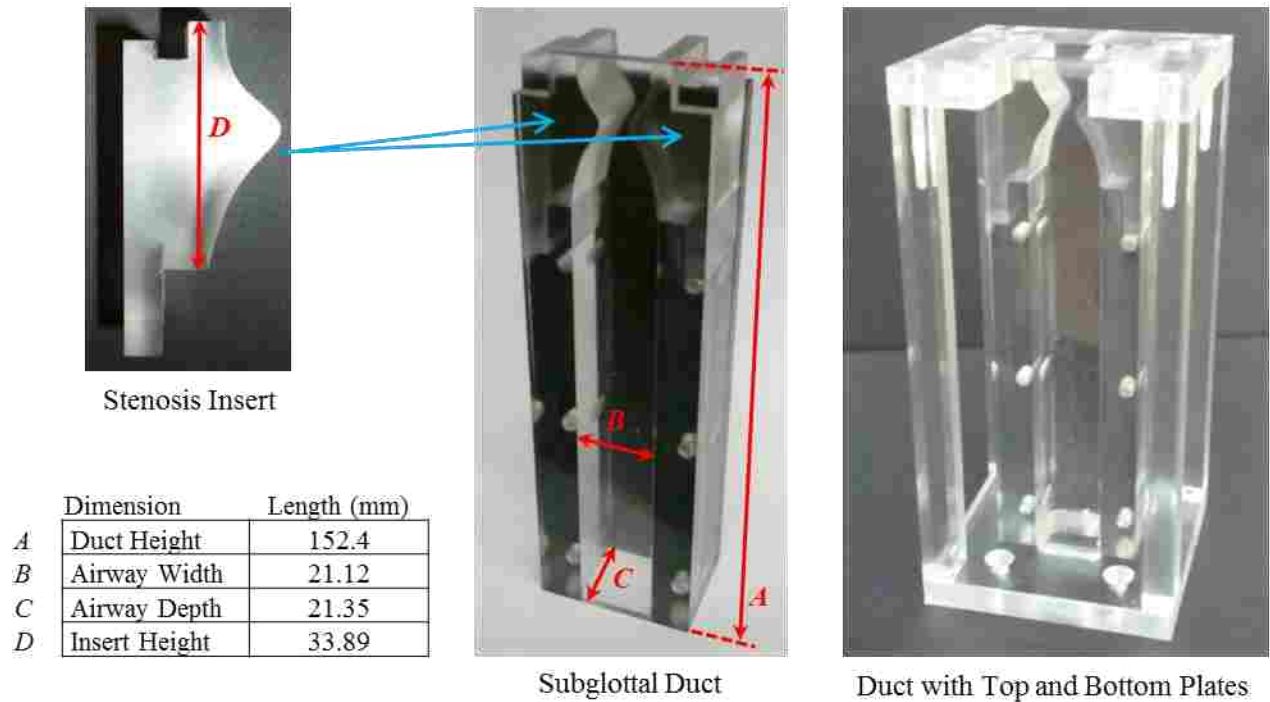


Figure 4-1. Images of subglottal duct and stenosis insert with dimensions.

4.2.3 Vocal Fold Model

The vocal fold models used in this study were the same as the model developed by Murray (2011). Figure 4-2 shows model geometry and dimensions. Following the procedure of Murray, the models consisted of four layers representing the body, ligament, cover, and epithelial tissue layers of the vocal folds with a fiber through the ligament layer to create anisotropic material stiffness. The models were fabricated using three-part addition cure silicone with differing ratios to create material properties appropriate for each layer.

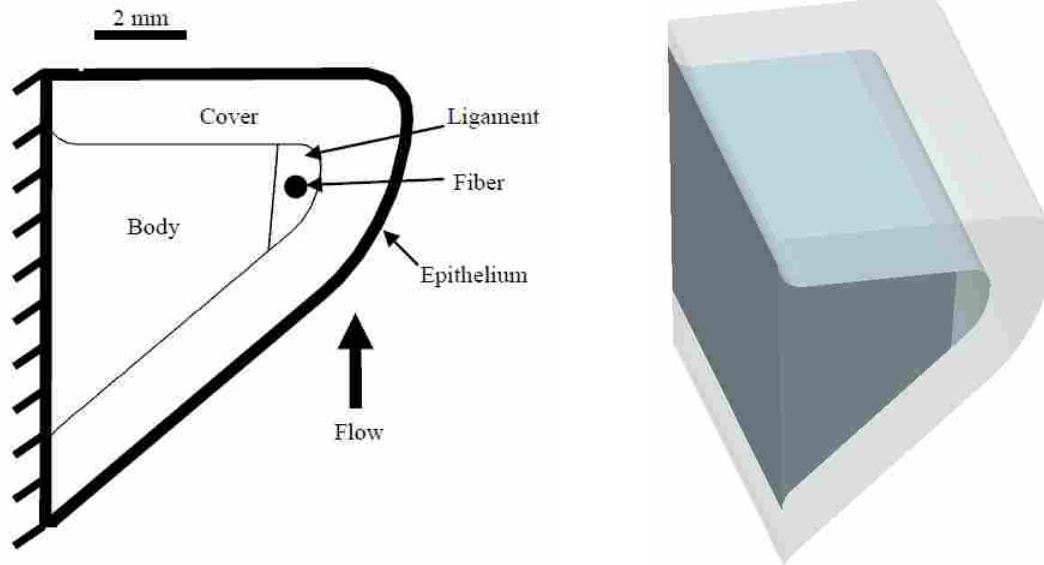


Figure 4-2. Synthetic vocal fold model, showing coronal cross-section with four-layer geometry (left) and isometric view (right).

At the time of model fabrication, specimens of the silicone used for each layer were made to test material properties. Cylindrical tensile specimens, 8 mm in diameter and approximately 120 mm long, were used to obtain elastic modulus data. Using an Instron tensile tester (3342) the specimens were extended at 1000 mm/min to 40% strain for 5 pre-cycles and then extended once more to 40% strain at 10 mm/min. Data from this last extension was recorded and used to calculate the Young's modulus. Young's modulus values for the body, ligament, and epithelial layers were 16.2, 1.96, and 66.5 kPa, respectively. The cover material was too soft for tensile testing; therefore, thin, cylindrical specimens (40 mm in diameter and 2 mm thick) for viscoelastic material properties measurements were fabricated. Using a TA Instruments rheometer (AR-2000EX) with a 40 mm parallel plate geometry, the specimens were subject to rotational shear forces at rates from 0.1 to 100 rad/s in order to determine the elastic and shear moduli (G' and G'') and dynamic viscosity (η') of the material. Results of the tests are shown in

Figure 4-3. While G' was relatively constant, G'' generally increased and η' decreased with increasing angular frequency, demonstrating that the silicone exhibited viscoelastic material behavior. This material behavior is similar to properties of human vocal fold tissue (Chan and Rodriguez, 2008).

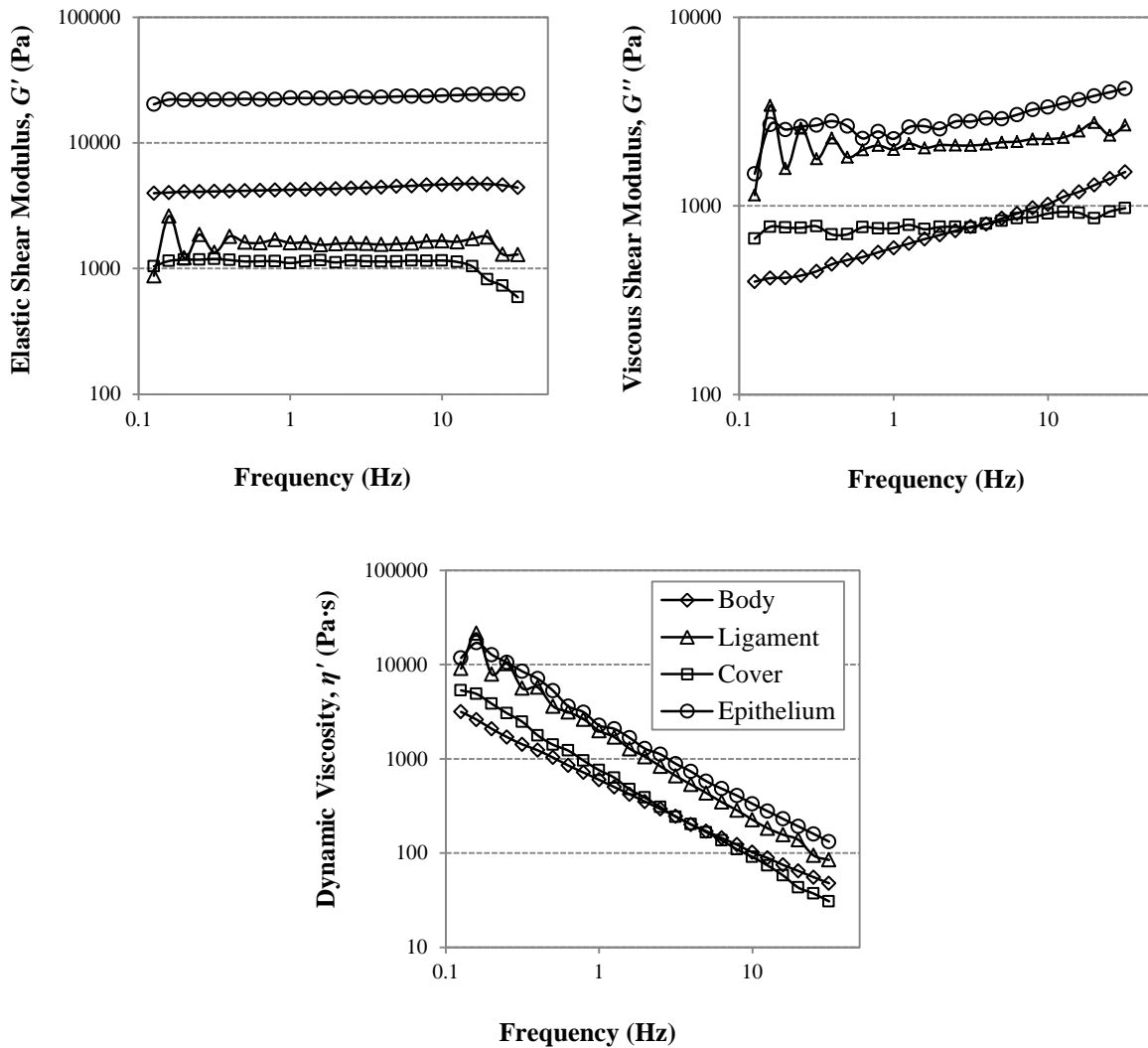


Figure 4-3. Rheological properties of silicone for various vocal fold model layers.

4.2.4 Experimental Setup

The experimental setup is illustrated in Figure 4-4. A pressurized air source was connected to a plenum settling chamber. A 40 cm flexible PVC tube connected the plenum to the subglottal duct. The vocal fold models were fastened to the top of the subglottal duct, in line with the air flow. A rotameter (Key Instruments) was installed upstream of the plenum to measure and adjust flow rate. Two differential pressure transducers (Kulite XCS-1-140-1D) were placed in pressure taps (1.85 mm diameter) in the subglottal duct to acquire pressure waveforms at two locations: (1) upstream of the stenosis (herein referred to as pre-stenosis pressure), and (2) directly below the vocal folds (herein referred to as post-stenosis pressure). A microphone (Larson Davis 2520) was clamped in place above the vocal fold models to record radiated sound during model vibration. The signals from the pressure transducers and microphone were read into and recorded by LabVIEW (National Instruments) by means of a National Instruments data acquisition system (NI cDAQ-9172). A high speed camera (Photron Fastcam SA3) was mounted above the vocal fold models to capture model motion.

4.2.5 Experimental Procedures

Vocal fold model vibration was initiated by effecting air flow through the vocal fold models until self-oscillation was produced. Onset pressure was determined by gradually increasing air flow via the flow meter valve until the models just began to vibrate, and recording the mean pressure recorded by the post-stenosis pressure transducer. This was done five times and the onset pressure values were averaged to take into account variation in the onset pressure. Using the average onset pressure (P_{on}) values of 125% and 150% of the onset pressure ($P_{1.25}$ and $P_{1.5}$) were determined, and the models were then vibrated at approximately these nominal values.

The values at which the models actually vibrated were not exactly these nominal values because of variation in the pressure signal and sensitivity of the flow control valve.

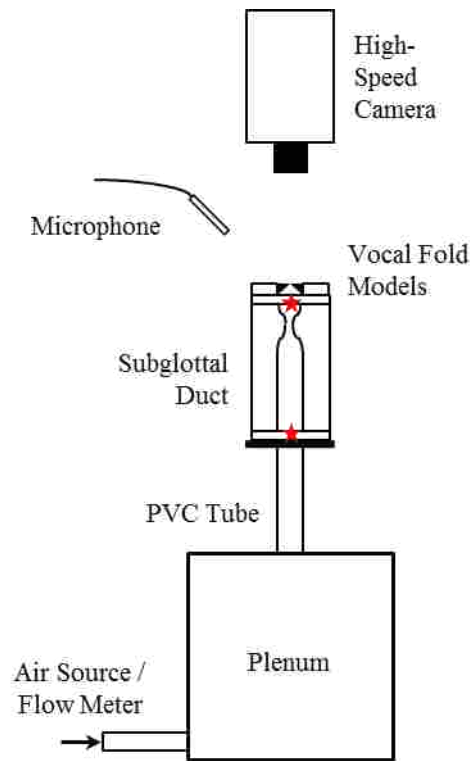


Figure 4-4. Experimental setup. Red stars show pressure tap locations in subglottal duct.

Data were acquired for each of three stenosis inserts (0%, 60%, and 95% stenosis) at each of the three pressures. The data included flow rate, pressure waveforms and mean pressures for both the pre- and post-stenosis pressures, microphone output, and high speed images. Flow rate was manually read from the flow meter. Pressure and sound data were recorded in LabVIEW for 0.488 s at a rate of 25,600 Hz. Also included in the LabVIEW output was a spectral analysis of the sound for each run, with a resolution of 2.048 Hz. High speed images of a superior view of the vocal fold model vibration were recorded at 3000 frames per second with 512×512 pixel resolution. Approximately 3000 images were saved for each run. Images were postprocessed

using a MATLAB code to obtain glottal area and videokymogram (VKG) images of the model motion. Glottal area was found by using a thresholding function to select all the pixels that represented dark glottal space and calculating the area with a pixel/mm calibration. VKG images were obtained in the MATLAB code by locating the center of the glottis in the anterior-posterior direction and retrieving the line of pixels perpendicular to the glottal opening at the center. The line of pixels retrieved from each image became each consecutive column of pixels in a VKG image. VKG images show glottal area waveforms and are sometimes used in clinical settings to observe asymmetric motion and mucosal wave motion.

4.2.6 Uncertainty Analysis and Statistical Significance

Estimates of the uncertainty in each of the experimental measurements were calculated. Details of the calculations are provided in Appendix A. Calculated uncertainty values are listed in Table 4-1.

Statistical significance of the results was determined by an unpaired t -test. The results between cases (samples) were compared by first calculating a two-sample t -statistic, given by

$$t = \frac{\bar{y}_1 - \bar{y}_2}{\sqrt{s_1^2/n_1 + s_2^2/n_2}}, \quad (4-1)$$

where \bar{y} is the sample mean, s is the sample standard deviation, and n is the number of sample data points. The subscripts 1 and 2 correspond to each respective sample in the comparison. From this t -statistic a p -value was found and compared to a significance level of $\alpha = 0.05$, corresponding to a 95% confidence level. If the resulting p -value of the comparison was less than 0.05 the difference in the results between the two cases was considered to be statistically significant. Because multiple measurements were only taken at onset pressure, statistical significance could only be determined for results at P_{on} .

Table 4-1. Uncertainty in experimental measurements.

<i>Measurement</i>	<i>Uncertainty</i>
Subglottal Pressure	± 27.88 Pa
Onset Pressure	± 75.91 Pa
Flow Rate	± 48.6 ml/s
Frequency	± 1.024 Hz
Glottal Area	± 1.157 mm ²

4.3 Results

4.3.1 Pressure

Figure 4-5 shows mean pre- and post-stenosis pressure data for the three different stenosis severities (0%, 60%, and 95%) at the three pressures (P_{on} , $P_{1.25}$, and $P_{1.5}$). Onset pressure increased slightly as stenosis severity increased. Pre- and post-stenosis pressure readings at all three pressures were essentially identical for the 0% and 60% cases, while the pre- and post-stenosis pressure differed at all three pressures for the 95% case. Pre-stenosis pressure was considerably greater than post-stenosis pressure, signifying that a pressure drop existed across the stenosis. The pressure drop increased with increasing pressure, having dropped by 9%, 13%, and 17% at P_{on} , $P_{1.25}$, and $P_{1.5}$, respectively. While the uncertainty of the pressure measurements was high compared to the magnitude of the pressure drops (± 28 Pa compared to 19, 35, and 57 Pa), the same behavior was repeated at all three pressures. Thus, there is confidence in the results. Comparing pre- and post-stenosis pressures at P_{on} yielded p -values much greater than $\alpha = 0.05$ for the 0% and 60% cases but less ($p = 0.01$) for the 95% case, showing that the pressure drop was statistically significant.

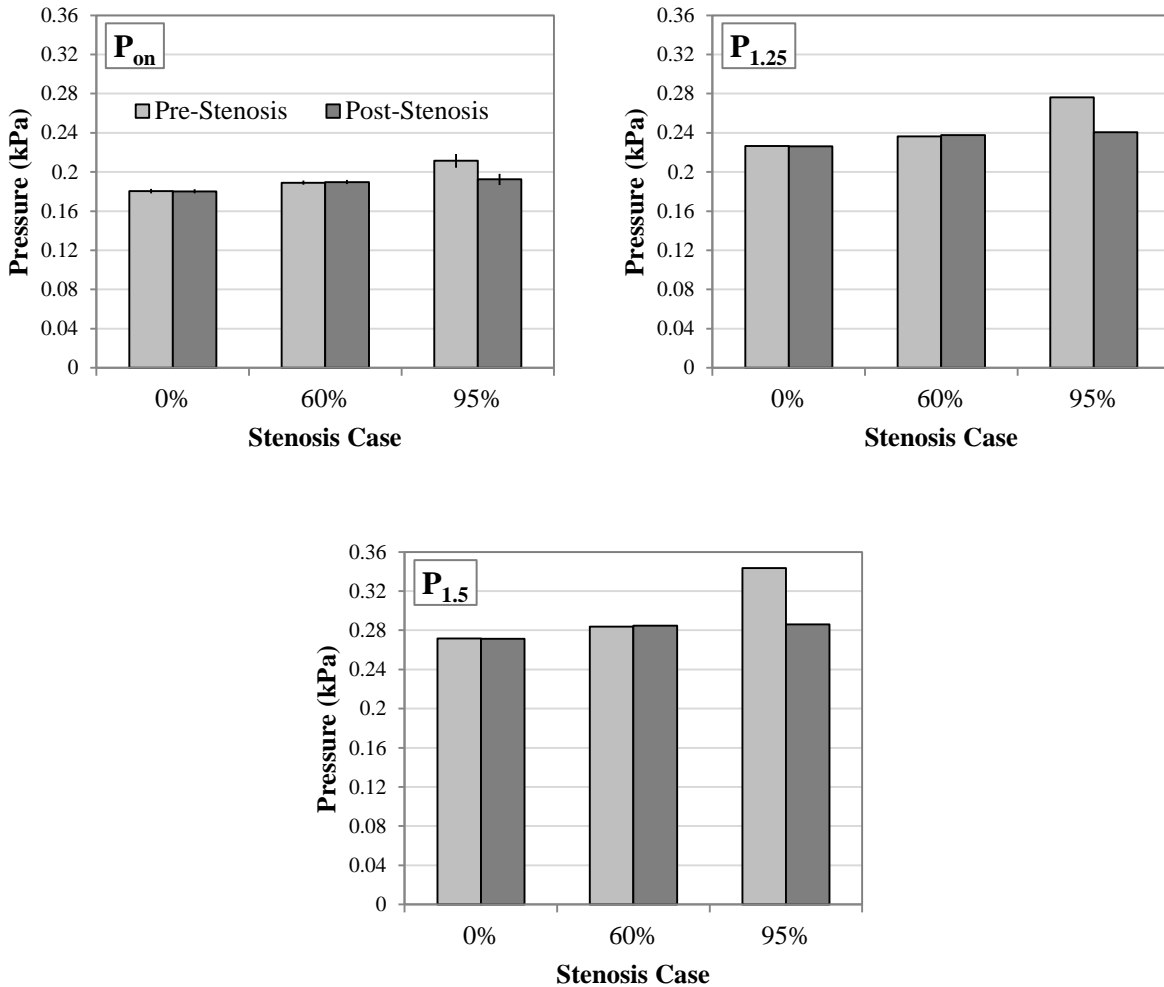


Figure 4-5. Mean pre- and post-stenosis pressure measurements for each case of stenosis severity. Top right and left plots are at onset pressure (P_{on}) and 125% of onset pressure ($P_{1.25}$), respectively. Bottom plot is at 150% of onset pressure ($P_{1.5}$). Lighter gray represents pre-stenosis pressure, and darker gray denotes post-stenosis pressure. Error bars at P_{on} show one standard deviation.

Pressure waveforms for the first 0.05 s of recorded pressure data are shown in Figure 4-6 for all stenosis cases at $P_{1.25}$. The waveforms for the 0% and 60% case showed similar trends. The pre-stenosis and post-stenosis pressures were generally in phase. The waveforms were similar, although the post-stenosis pressure clearly reached a higher value than the pre-stenosis pressure. Since Figure 4-5 showed that the mean pressures were essentially the same, this higher subglottal pressure here must be accounted for in other deviations between the waveforms,

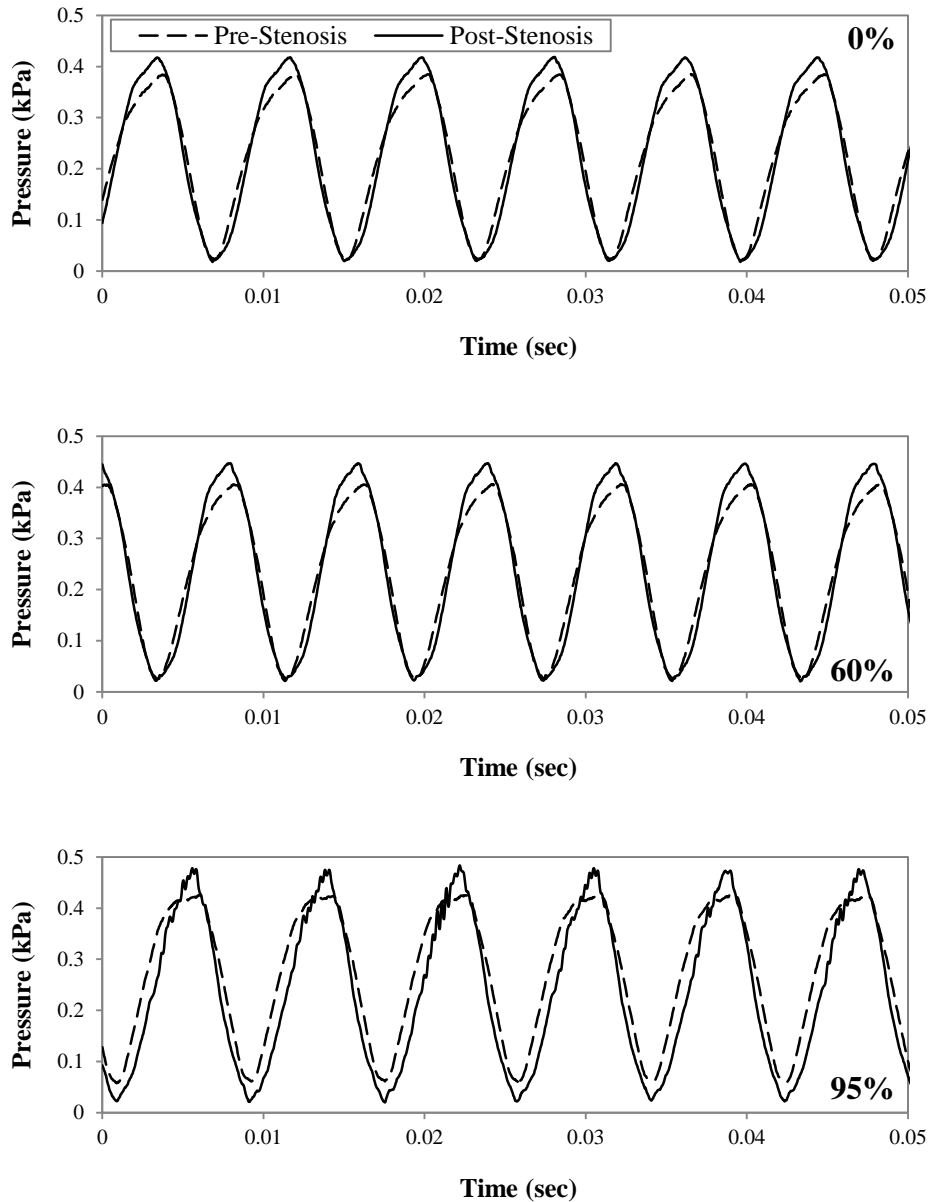


Figure 4-6. Pressure waveforms for the first 0.05 sec of recorded data for the 0% (top), 60% (middle), and 95% (bottom) cases at 125% of onset pressure ($P_{1.25}$).

likely, in the valley of the waveform where the post-stenosis pressure spends more time at values below the mean than the pre-stenosis pressure. The 95% case showed somewhat different behavior between the pre-stenosis and post-stenosis waveforms. The peak of the post-stenosis pressure was again higher, but the trough was also lower, than the pre-stenosis pressure. Also,

the trough of the post-stenosis waveform was even wider for this case, likely contributing to the mean pressure post-stenosis being lower than the pre-stenosis pressure for the 95% case. Another feature of interest is the noise that appears in the post-stenosis pressure waveform. This is not apparent in the 0% or 60% cases. The pre-stenosis pressure for the 95% case also does not appear to experience this noise. Pressure waveforms at P_{on} and $P_{1.5}$ showed similar results to these for all cases, except that the noise in the post-stenosis pressure waveform for 95% was less at P_{on} and slightly more prevalent at $P_{1.5}$.

4.3.2 Glottal Area, Flow Rate, and Frequency

Figure 4-7 shows glottal area over an oscillatory cycle for each case at $P_{1.25}$. The glottal area waveforms appeared very similar for all three cases. Both the 60% and 95% glottal area curves bear the same general shape as the 0% case, and the peak occurs at the same point in the cycle, meaning that the duration of the glottal opening and closing phases were unchanged. The 0% and 60% cases exhibit essentially the same maximum glottal area (about 16 mm²). The only difference that was seen was a larger maximum glottal area (19.1 mm²) for the 95% case compared to the others. At P_{on} all the waveforms, including maxima, showed no significant differences. At $P_{1.5}$ the same behavior as that shown here was observed, with the 0% and 60% cases being essentially identical and the 95% case showing a greater maximum glottal area.

Flow rate and model vibration frequency values versus pressure are given for all cases in Figure 4-8. As expected, flow rate increased steadily as pressure increased. The pressure-flow relationship was more or less linear for all three cases, generally increasing by 25% to 30% with each pressure increase. Comparing the cases at each pressure showed a sporadic trend, as flow rates for the 60% cases were 7% (or less) lower than the 0% cases, while 60% to 95% cases

showed up to about a 17% increase. The uncertainty in flow rate measurement (± 48.6 ml/s) was higher than any of the variation between cases.

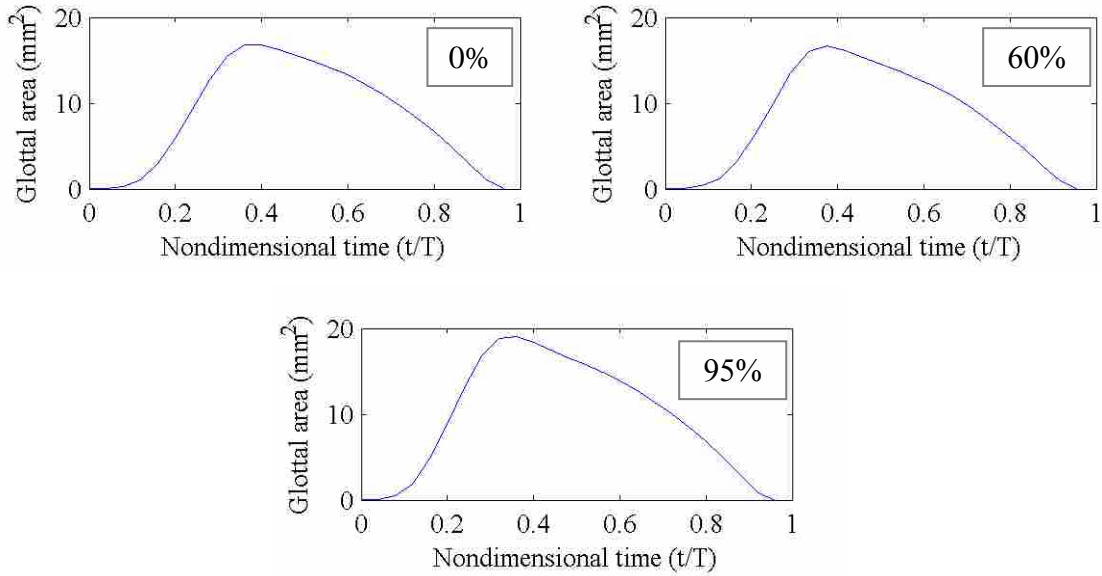


Figure 4-7. Glottal area over a nondimensionalized oscillatory cycle for all three cases at $P_{1.25}$.

Vibration frequency generally decreased with increasing pressure. The relationship here was again linear for the 0% and 60% cases, with frequency dropping about 3 Hz with each pressure increase. The 95% case, on the other hand, varied somewhat nonlinearly and showed twice as large of a frequency change between P_{on} and $P_{1.25}$ than the other cases. This contributed to a larger overall drop between P_{on} and $P_{1.5}$ of around 9 Hz. Like the other cases, the 95% case decreased about 3 Hz as pressure increased from $P_{1.25}$ to $P_{1.5}$. As with flow rate, frequency changed unpredictably between the stenosis cases, increasing approximately 3 Hz from 0% to 60% and decreasing close to 5 Hz from 60% to 95% at pressures above onset.

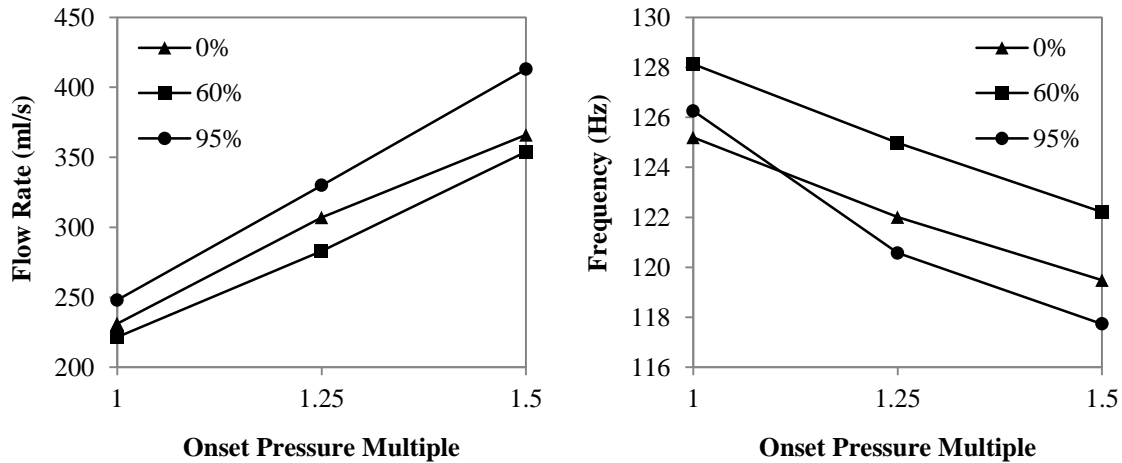


Figure 4-8. Flow rate (left) and model vibration frequency (right) for all cases and pressures.

4.3.3 Sound Analysis

Acoustic power spectral density (PSD) plots from the microphone signals for each case at $P_{1.25}$ are given in Figure 4-9. The two primary contributors to the radiated sound were at the fundamental frequencies (about 122, 125, and 120 Hz) and the next harmonic frequencies (about twice the fundamentals) for the 0%, 60%, and 95% cases, respectively. Other smaller contributions are seen at the higher harmonics. The fundamental frequency corresponds to the model vibration frequency.

While some subtle differences in the amplitudes of the PSD spikes were observable, the combine effect of the differing amplitudes over the spectrum was uncertain. In addition, the PSD amplitudes were influenced by driving pressure and flow rate, values which were slightly

different for the different cases. Therefore, in order to make the power spectra directly comparable, power efficiency (η_{power}) was calculated as

$$\eta_{power} = \frac{\Pi}{\bar{P}_s \bar{U}}, \quad (4-2)$$

where Π is the total radiated power, found by integrating PSD over the desired frequency range (100 to 1000 Hz, in the present study), \bar{P}_s is the mean subglottal pressure, and \bar{U} is the average flow rate.

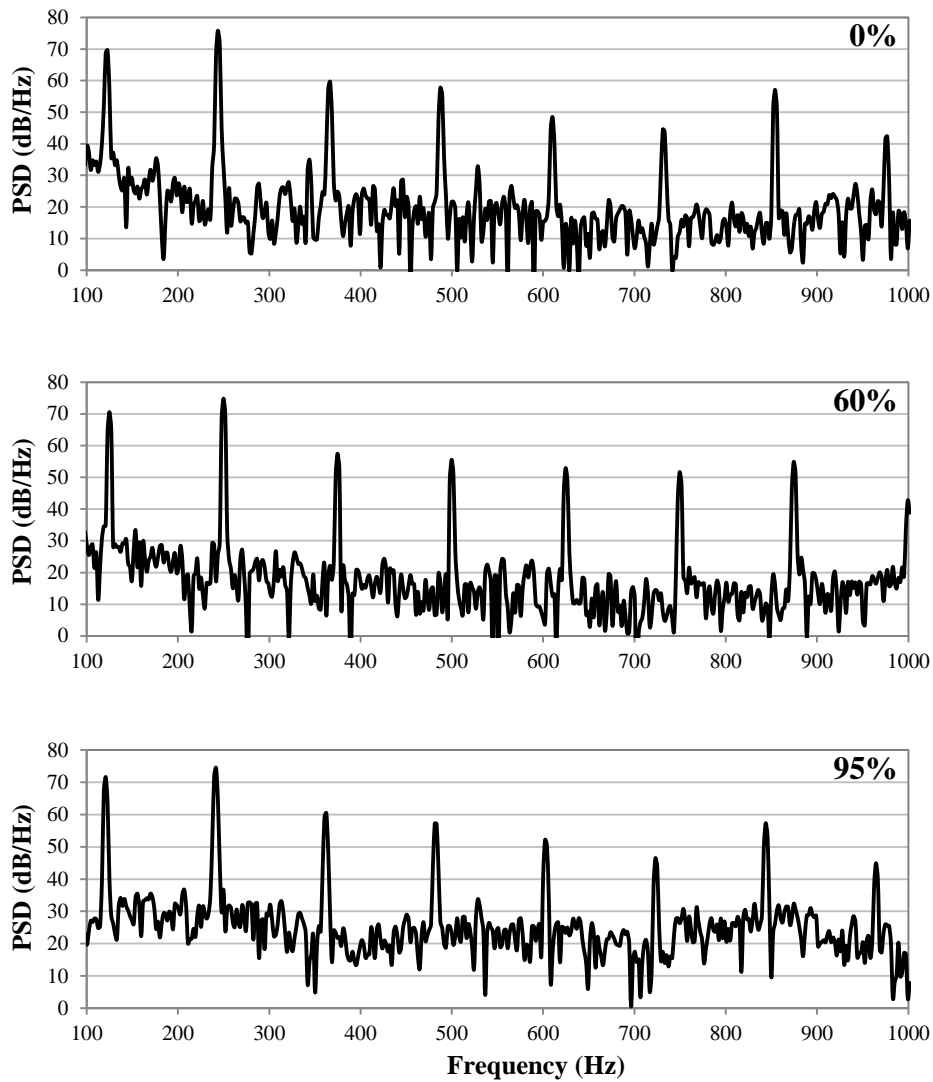


Figure 4-9. Power spectral density plots for each case at $P_{1.25}$.

Power efficiency values, normalized by the efficiency for the 0% case at each respective pressure, are shown in Figure 4-10. Power efficiency remained almost unchanged between the 0% and 60% cases but clearly decreased between the 60% and 95% cases. The drop in efficiency was 13% at both P_{on} and $P_{1.25}$ and 17% at $P_{1.5}$.

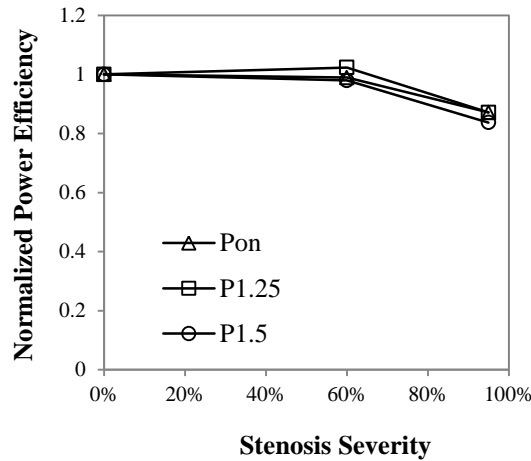


Figure 4-10. Power efficiency vs. stenosis severity at three pressures.

4.3.4 Videokymography

High-speed videokymograms (VKGs) of the 0%, 60%, and 95% cases at $P_{1.25}$ are displayed in Figure 4-11 for 10 oscillatory cycles. Regions are marked in the figure which corresponded to distinct phases of the glottal area waveform. Region A was during glottal opening, where the glottal profile is convergent and the pixel line showed only the superior surface of the vocal fold model. Region B was during glottal closing where the glottis shifted to a divergent shape so that the medial surface also was visible (darker, medial-most area). Region C denotes where the vocal fold models contacted and the glottis was fully closed.

Comparison of the cases did not reveal any significant differences in the motion. The duration of each portion of the cycle (opening, closing, closure) appeared to be essentially the same for all of the cases. The pixel lines throughout the cycle appeared to show the same features of the vocal fold surface for all three cases. Consistent with glottal area results above, the 95% case seemed to have a slightly larger maximum glottal width than the other two cases. Other distinct features that would indicate differences in model motion among the cases were not evident.

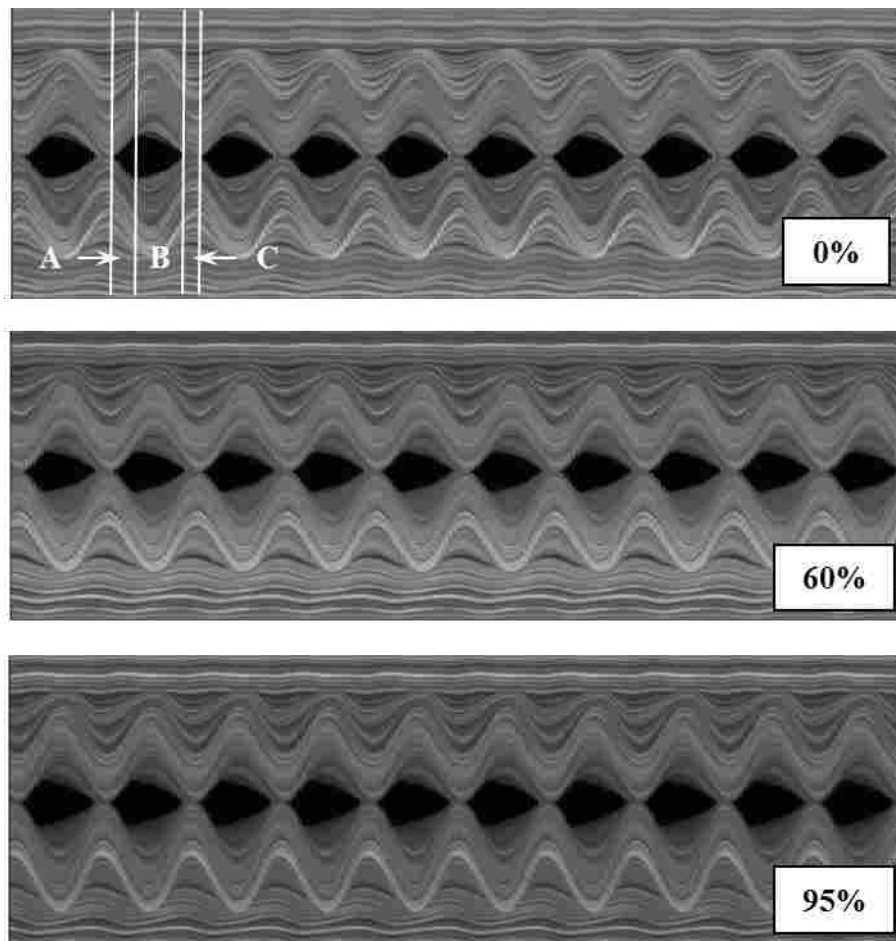


Figure 4-11. Videokymograms for 0% (top), 60% (middle), and 95% (bottom) cases at $P_{1.25}$.

4.4 Discussion

Mean pressure and pressure waveform data pre- and post-stenosis revealed that the stenosis presence had an effect on subglottal pressure distribution at high severities of stenosis. Mean pressure data showed a pressure drop across the stenosis at 95% which increased as subglottal pressure was increased. This result agrees with studies that have computationally modeled airways with stenosis and found that the stenosis caused increased pressure drops in the flow (Cebal and Summers, 2004; Brouns et al., 2006; Mihaescu et al., 2008). In addition, in the previous chapter it was shown that the pressure drop across a stenosis in a computational model increased with increasing stenosis severity and in turn affected glottal resistance and other factors. A significant pressure drop across the stenosis at 95% likely indicates that in order to increase the subglottal pressure to the onset pressure a higher lung pressure is required. This may correspond to more effort required for speech in patients with high severities of stenosis.

Another effect of the stenosis was that the pressure waveform for the 95% case showed high frequency noise, where none was present in the other cases. It is possible that the source of the noise was turbulence in the subglottal flow due to the stenosis, but this is uncertain. Flow visualization should be performed in order to determine if subglottal flow is indeed disturbed by the stenosis and how this might affect subglottal pressure.

The stenosis apparently had little effect on the glottal width and general model motion. The VKGs showed essentially no change between the normal case and the stenosis cases, except a slightly greater glottal width for the 95% case, which was consistent with the greater glottal area calculations for this case. It is uncertain why glottal area was larger for the 95% case and not for the 60% case. It is possible that the slightly higher subglottal pressure and flow rate for this case would contribute to greater driving forces and a wider opening glottis, but the variation

in pressure and flow did not seem to make a difference for the 60% case. Another explanation may be experimental artifacts. For example, as stenosis inserts were exchanged, the vocal folds models were unmounted from the setup. Remounting the models caused them to be slightly closer or farther apart than for the previous case, contributing to differences in the maximum glottal gap achieved during vibration. Further investigation into this measure would be warranted.

Flow rate and frequency results were somewhat inconclusive. Flow rate and frequency varied expectedly as pressure increased but showed unpredictable variation with increasing stenosis severity. While measurement uncertainty may have played a role, another reason for this behavior was again possibly the method of varying stenosis severity, explained above. Since the onset pressure, flow rate, and frequency for these particular models are highly sensitive to how much initial contact and pressure exists between the models, this may have contributed to the sporadic trend between cases. Although firm conclusions cannot be drawn about the effect of the stenosis because of this variation, there may still be some significance to a larger change between 60% and 95% than between 0% and 60%.

Sound analysis provided evidence that a stenosis alters power efficiency of the radiated sound at high severities of stenosis. Power efficiency generally shows how much power is produced for the given pressure and flow rate. Regarding the voice, it is related to the effort required to produce the sound. These results suggested that with the presence of SGS, the effort required to speak increases since less power is produced for the given pressure and flow rate.

Overall, the results of the present study compare well with and show similar behavior as those seen in computational models (see section 3.3). Here a noticeable pressure drop occurred in the flow across the stenosis at 95%. The computational models showed that the pressure drop

across the stenosis was substantial enough to affect glottal resistance at stenosis severities of 90% and above. Glottal width, flow rate, and frequency were also affected with 90% or greater stenosis in the computational models. Although these results with the synthetic model were inconclusive, there was greater change in these same factors for the 95% case than for the 60% case. Additionally, power efficiency of the sound from the synthetic models followed the same trend as the computational model results, as it was not affected until the stenosis severity reached 95%.

4.5 Conclusions

Subglottic stenosis was modeled using an experimental airway setup, including four-layer silicone self-oscillating vocal fold models. This setup used to determine how subglottic stenosis affects vibration of synthetic models. Results showed that in a synthetic model subglottic stenosis caused a significant pressure drop across the stenosis at 95%, which increased as pressure was increased. In addition, power efficiency of the radiated sound steadily decreased with increasing stenosis severity, which may have important implications for the effect of stenosis on the human voice. Stenosis had little effect on glottal area and model motion. The stenosis generally had a more noticeable and substantial effect for the 95% case. This compares well with the results of the computational work of the previous chapter, which showed that stenosis affects vocal fold model vibration at severities of 90% or higher.

5 CONCLUSIONS AND FUTURE WORK

5.1 Effect of Inferior Angle on the Self-Oscillation of a Computational Vocal Fold Model (Chapter 2)

5.1.1 Conclusions

A two-dimensional, self-oscillating, finite element model of the vocal folds was used to study the effect of changing inferior vocal fold surface geometry on vocal fold vibration. Fully-coupled fluid-structure interaction simulations with varying geometry were performed. Simulations using a partially rigid model were carried out in order to isolate and study the effects of changing subglottal aerodynamic loading on the model. Results of the fully-flexible model simulations showed that vocal fold vibration was significantly altered as the inferior angle of the model was varied. Specifically, reducing the angle resulted in greater vertical displacement of the vocal fold and a smaller convergent-divergent spatial portion of the glottis. Associated with changes in vibration were decreases in glottal width and flow rate amplitudes and net airflow-to-tissue energy transfer as the inferior surface angle was reduced. The partially rigid model responses yielded evidence that changes in vibration of the fully-flexible models occurred primarily because of changes in structural, rather, than aerodynamic, model responses.

5.1.2 Future Work

In order to confirm these findings and draw further conclusions regarding vocal fold vibration and voice quality, future studies are recommended, including more advanced computer modeling (e.g., three-dimensional, more anatomically accurate geometry, and materially anisotropic models over a range of geometries), and experiments using synthetic vocal fold models and possibly excised larynges. Future research should also include an in-depth exploration of why changing the inferior angle caused the resulting response and what profile geometry is optimal.

5.2 Influence of Subglottic Stenosis on Computational Vocal Fold Model Flow-Induced Vibration (Chapter 3)

5.2.1 Conclusions

A two-dimensional, fluid-structure interaction model was used to simulate the flow-induced vibration of the vocal folds with varying degrees of subglottic stenosis. The results showed that the presence of stenosis of up to 60% did not alter vocal fold vibration, while a stenosis of 90% or greater influenced several factors related to vocal fold vibration. Vertical model displacement, glottal width amplitude, and flow rate amplitude decreased with increasing stenosis severity above 90%. The model sensitivity to subglottic stenosis increased with increasing pressure, and changes in vibration correlated with changes in glottal flow resistance. Subglottic stenosis caused a substantial pressure drop in the subglottis, which may be a large contributing factor to other parameters, such as resistance and glottal width, being affected. Stenosis caused significant disturbances in subglottal flow with as low as 60% stenosis, which increased with increasing stenosis severity. The disturbed flow did not appear to affect vibration.

High severities of stenosis lead to significant decreases in frequency and maximum flow declination rate, suggesting that subglottic stenosis can cause changes in sound and power of the voice.

5.2.2 Future Work

Because this is the first attempt to study the response of self-oscillating vocal fold models due to SGS, further work must be performed in order to corroborate the findings of the present study. While the experimental work in Chapter 4 begins to address the need for comparison to the response of synthetic vocal fold models, further work using synthetic models is suggested. Supplemental computational studies should employ three-dimensional geometry and more complete material definitions (i.e., viscoelasticity, anisotropy). Most importantly, there is a need for data from real vocal folds, including both in-depth studies of voice quality in SGS patients and studies using excised larynges. Future studies should consider varying stenosis location and defining a more realistic stenosis, including accurate three-dimensional geometry and improved tissue properties. In addition, flow visualization, particularly particle image velocimetry, in the region of the stenosis should be performed.

5.3 Influence of Subglottic Stenosis on Synthetic Vocal Fold Model Flow-Induced Vibration (Chapter 4)

5.3.1 Conclusions

Subglottic stenosis was modeled using an experimental airway setup, including four-layer silicone self-oscillating vocal fold models. This setup used to determine how subglottic stenosis affects vibration of synthetic models. Results showed that in a synthetic model subglottic stenosis caused a significant pressure drop across the stenosis at 95%, which increased as

pressure was increased. In addition, power efficiency of the radiated sound steadily decreased with increasing stenosis severity, which may have important implications for the effect of stenosis on the human voice. Stenosis had little effect on glottal area and model motion. The stenosis generally had a more noticeable and substantial effect for the 95% case. This compares well with the results of the computational work of the previous chapter, which showed that stenosis affects vocal fold model vibration at severities of 90% or higher.

5.3.2 Future Work

While the present study represents relevant work, it is somewhat preliminary and should include in the future more extensive research, including more cases of stenosis, multiple models, and both glottal jet and subglottal flow visualization. Other suggestions for future work include those given in the future work section for Chapter 3 above (Section 5.2.2).

REFERENCES

- Agarwal, M., Scherer, R. C., and Hollien, H. (2003). "The false vocal folds: Shape and size in frontal view during phonation based on laminagraphic tracings," *J. Voice* 17, 97-113.
- Alipour-Haghighi, F., and Titze, I. R., (1991). "Elastic models of vocal fold tissues," *J. Acoust. Soc. Am.* 90 (3), 1326-1331.
- Alipour, F., Berry, D. A., and Titze, I. R. (2000). "A finite-element model of vocal fold vibration," *J. Acoust. Soc. Am.* 108, 3003-3012.
- Alipour, F., and Scherer, R. C. (2000). "Vocal Fold Bulging Effects on Phonation Using a Biophysical Computer Model," *J. Voice* 14 (4), 470-483.
- Alipour, F., and Scherer, R. C. (2004). "Flow separation in a computational oscillating vocal fold model," *J. Acoust. Soc. Am.* 116 (3), 1710-1719.
- Austin, S. F., and Titze, I. R. (1997). "The Effect of Subglottal Resonance Upon Vocal Fold Vibration," *J. Voice* 11 (4), 391-402.
- Baer, T. (1981). "Observation of vocal fold vibration: Measurement of excised larynges," in *Vocal Fold Physiology*, edited by K. N. Stevens and M. Hirano (University of Tokyo Press, Tokyo), pp. 119-133.
- Bailey, M., Hoeve, H., and Monnier, P. (2003). "Paediatric laryngotracheal stenosis: a consensus paper from three European centres," *Eur. Arch. Otorhinolaryngol.* 260, 118-123.
- Boessnecker, A., Berry, D. A., Lohscheller, J., Eysholdt, U., and Doellinger, M. (2007). "Mucosal Wave Properties of a Human Vocal Fold," *Acta Acust. United Ac.* 93, 815-823.
- Brouns, M., Jayaraju, S. T., Lacor, C., De Mey, J., Noppen, M., Vincken, W., and Verbanck, S. (2007). "Tracheal stenosis: a flow dynamics study," *J. Appl. Physiol.* 102, 1178-1184.

- Cebral, J. R., and Summers, R. M. (2004). "Tracheal and Central Bronchial Aerodynamics Using Virtual Bronchoscopy and Computational Fluid Dynamics," *IEEE Trans. Med. Imag.* 23 (8), 1021-1033.
- Chan, R. W., Titze, I. R., and Titze, M. R. (1997). "Further studies of phonation threshold pressure in a physical model of the vocal fold mucosa," *J. Acoust. Soc. Am.* 101 (6), 3722-3727.
- Chan, R. W., Fu, M., Young, L., and Tirunagari, N. (2007). "Relative Contributions of Collagen and Elastin to Elasticity of the Vocal Fold Under Tension," *Ann. Biomed. Eng.* 35 (8), 1471-1483.
- Chan, R. W., and Rodriguez, M. L. (2008). "A simple-shear rheometer for linear viscoelastic characterization of vocal fold tissues at phonatory frequencies," *J. Acoust. Soc. Am.* 124 (2), 1207-1219.
- Cotton, R. T. (1991). "The problem of pediatric laryngotracheal stenosis: a clinical and experimental study on the efficacy of autogenous cartilaginous grafts placed between the vertically divided halves of the posterior lamina of the cricoid cartilage," *Laryngoscope* 101 (Suppl. 56), 1-34.
- Decker, G. Z., and Thomson, S. L. (2007). "Computational Simulations of Vocal Fold Vibration: Bernoulli Versus Navier-Stokes," *J. Voice* 21 (3), 273-284.
- Doellinger, M., and Berry, D. A. (2006). "Visualization and Quantification of the Medial Surface Dynamics of an Excised Human Vocal Fold During Phonation," *J. Voice* 20 (3), 401-413.
- Ettema, S. L., Tolejano, C. J., Thielke, R. J., Toohill, R. J., and Merati, A. L. (2006). "Perceptual voice analysis of patients with subglottic stenosis," *Otolaryngol. Head Neck Surg.* 135, 730-735.
- Fukuda, H., Saito, S., Kitahara, S., Isogai, Y., Makino, K., Tsuzuki, T., Kogawa, N., and Ono, H. (1983). "Vocal fold vibration in excised larynges viewed with an x-ray stroboscope and an ultra-high speed camera," in *Vocal Fold Physiology: Contemporary Research and Clinical Issues*, edited by D. M. Bless and J. H. Abbs (College-Hill Press, San Diego), pp. 238-252.
- George, M., Lang, F., Pasche, P., and Monnier, P. (2005). "Surgical management of laryngotracheal stenosis in adults," *Eur. Arch. Otorhinolaryngol.* 262, 609-615.

- Giudice, M., Piazza, C., Foccoli, P., Toninelli, C., Cavaliere, S., and Peretti, G. (2003). "Idiopathic subglottic stenosis: management by endoscopic and open-neck surgery in a series of 30 patients," *Eur. Arch. Otorhinolaryngol.* 260, 235-238.
- Grillo, H. C., Mathisen, D. J., Ashiku, S. K., Wright, C. D., and Wain, J. C. (2003). "Successful treatment of idiopathic laryngotracheal stenosis by resection and primary anastomosis," *Ann. Otol. Rhinol. Laryngol.* 112, 798-800.
- Grisel, J., Khosla, S., Murugappan, S., Lakhamraju, R., Aubry, J., Gutmark, E., and Huntress, G. (2010). "How Does the Absence or Presence of Subglottal Medialization Affect Glottal Airflow?," *Ann. Otol. Rhinol. Laryngol.* 119 (8), 559-566.
- Herrington, H. C., Weber, S. M., and Anderson, P. E. (2006). "Modern Management of Laryngotracheal Stenosis," *Laryngoscope* 116, 1553-1557.
- Hirano, M. (1981). *Clinical Examination of Voice*, Springer-Verlag, New York.
- Hirano, M., Kurita, S., and Nakashima, T. (1981). "The structure of the vocal folds," in *Vocal Fold Physiology*, edited by K. N. Stevens and M. Hirano (University of Tokyo Press, Tokyo), pp. 33-43.
- Hofmans, G. C. J. (1998). "Vortex Sound in Confined Flows," Ph.D. thesis, Technische Universiteit Eindhoven, Eindhoven.
- Hofmans, G. C. J., Groot, G., Ranucci, M., Graziani, G., and Hirschberg, A. (2003). "Unsteady flow through in-vitro models of the glottis," *J. Acoust. Soc. Am.* 113, 1658-1675.
- Hsiao, T., Liu, C., Luschei, E. S., and Titze, I. R. (2001). "The Effect of Cricothyroid Muscle Action on the Relation Between Subglottal Pressure and Fundamental Frequency in an *In Vivo* Canine Model," *J. Voice* 15 (2), 187-193.
- Jiang, J. J., and Titze, I. R. (1993). "A methodological study of hemilaryngeal phonation," *Laryngoscope* 103 (8), 872-882.
- Lesperance, M. M., and Zalzal, G. H. (1998). "Laryngotracheal stenosis in children," *Eur. Arch. Otorhinolaryngol.* 255: 12-17.

- Li, S., Scherer, R. C., Wan, M., Wang, S., and Wu, H. (2006a). "Numerical study of the effects of inferior and superior vocal fold surface angles on vocal fold pressure distributions," *J. Acoust. Soc. Am.* 119, 3003-3010.
- Li, S., Scherer, R. C., Wan, M., Wang, S., and Wu, H. (2006b). "The effect of glottal angle on intraglottal pressure," *J. Acoust. Soc. Am.* 119, 539-548.
- Lucero, J. C. (1998). "Optimal Glottal Configuration for Ease of Phonation," *J. Voice* 12 (2), 151-158.
- Luo, H., Mittal, R., and Bielałowicz, S. A. (2009). "Analysis of flow-structure interaction in the larynx during phonation using an immersed-boundary method," *J. Acoust. Soc. Am.* 126 (2), 816-824.
- Mihaescu, M., Gutmark, E., Murugappan, S., Elleru, R., Cohen, A., and Willging, J. P. (2008). "Modeling Flow in a Compromised Pediatric Airway Breathing Air and Heliox," *Laryngoscope* 118, 2205-2211.
- Murray, P. R. (2011). "Flow-Induced Responses of Normal, Bowed, and Augmented Synthetic Vocal Fold Models," Master's thesis, Brigham Young University, Provo, UT.
- Myer, C. L., O'Connor, D. M., and Cotton, R. T. (1994). "Proposed grading system for subglottic stenosis based on endotracheal tube sizes," *Ann. Otol. Rhinol. Laryngol.* 103 (1), 319-323.
- Nanayakkara, I. (2005). "Vocal fold superior and inferior angles measured from radiographic images," Master's thesis, Bowling Green State University, Bowling Green, OH.
- Oren, L., Khosla, S., Murugappan, S., King, R., and Gutmark, E. (2009). "Role of Subglottal Shape in Turbulence Reduction," *Ann. Otol. Rhinol. Laryngol.* 118 (3), 232-240.
- Pickup, B. A. (2010). "Influence of Material and Geometric Parameters on the Flow-Induced Vibration of Vocal Fold Models," Master's thesis, Brigham Young University, Provo, UT.
- Pickup, B. A., and Thomson, S. L. (2010). "Flow-induced vibratory response of idealized versus magnetic-resonance imaging-based synthetic vocal fold models," *J. Acoust. Soc. Am.* 128 (3), EL124.

- Poetker, D. M., Ettema, S. L., Blumin, J. H., Toohill, R. H., and Merati, A. L. (2006). "Association of airway abnormalities and risk factors in 37 subglottic stenosis patients," *Otolaryngol. Head Neck Surg.* 135, 434-437.
- Riede, T., Tokuda, I. T., Munger, J. B., and Thomson, S. L. (2008). "Mammalian laryngeal air sacs add variability to the vocal tract impedance: Physical and computational modeling," *J. Acoust. Soc. Am.* 124 (1), 634-647.
- Saito, S., Fukuda, H., Isogai, Y., and Ono, H. (1981). "X-ray stroboscopy," in *Vocal Fold Physiology*, edited by K. N. Stevens and M. Hirano (University of Tokyo Press, Tokyo), pp. 95-106.
- Scherer, R. C., and Shinwari, D. (2000). "Glottal pressure profiles for a diameter of 0.04 cm," *J. Acoust. Soc. Am.* 107, 2905.
- Scherer, R. C., Shinwari, D., DeWitt, K. J. D., Zhang, C., Kucinski, B. R., and Afjeh, A. A. (2001). "Intraglottal pressure profiles for a symmetric and oblique glottis with a divergence angle of 10 degrees," *J. Acoust. Soc. Am.* 109, 1616-1630.
- Schuberth, S., Hoppe, U., Doellinger, M., Lohscheller, J., and Eysholdt, U. (2002). "High-Precision Measurement of the Vocal Fold Length and Vibratory Amplitudes," *Laryngoscope* 112, 1043-1049.
- Shinwari, D., Scherer, R. C., DeWitt, K. J., and Afjeh, A. A. (2003). "Flow visualization and pressure distributions in a model of the glottis with a symmetric and oblique divergent angle of 10 degrees," *J. Acoust. Soc. Am.* 113, 487-497.
- Smith, M. E., Marsh, J. H., Cotton, R. T., and Myer III, C. M. (1993). "Voice problems after laryngotracheal reconstruction: videolaryngostroboscopic, acoustic, and perceptual assessment," *Int. J. Pediatr. Otorhinolaryngol.* 25 (1-3), 173-181.
- Smith, M. E., Roy, N., Stoddard, K., and Barton, M. (2008). "How Does Cricotracheal Resection Affect the Female Voice?" *Ann. Otol. Rhinol. Laryngol.* 117 (2), 85-89.
- Thomson, S. L., Mongeau, L., and Frankel, S. H. (2005). "Aerodynamic transfer of energy to the vocal folds," *J. Acoust. Soc. Am.* 118, 1689-1700.

- Titze, I. R. (1981). "Biomechanics and distributed mass models of vocal fold vibration," in *Vocal Fold Physiology*, edited by K. N. Stevens and M. Hirano (University of Tokyo Press, Tokyo), pp. 245-270.
- Titze, I. R. (1988). "The physics of small-amplitude oscillation of the vocal folds," *J. Acoust. Soc. Am.* 83, 1536-1552.
- Titze, I. R., and Sundberg, J. (1992). "Vocal intensity in speakers and singers," *J. Acoust. Soc. Am.* 91 (5), 2936-2946.
- Titze, I.R. (2000). *Principles of Voice Production*, Second Printing (National Center for Voice and Speech, Iowa City, IA), pp. 245-251.
- Titze, I. R. (2006). "Theoretical Analysis of Maximum Flow Declination Rate Versus Maximum Area Declination Rate in Phonation," *J. Speech Hear. Res.* 49, 439-447.
- Zalzal, G. H. (1988). "Rib cartilage grafts for the treatment of posterior glottic and subglottic stenosis in children," *Ann. Otol. Rhinol. Laryngol.* 97, 506-511.
- Zalzal, G. H., Loomis, S. R., and Fischer, M. (1993). "Laryngeal Reconstruction in Children: Assessment of Voice Quality," *Arch. Otolaryngol. Head Neck Surg.* 119, 504-507.
- Zhang, Z., Neubauer, J., and Berry, D. A. (2006a). "The influence of subglottal acoustics on laboratory models of phonation," *J. Acoust. Soc. Am.* 120 (3), 1558-1569.
- Zhang, Z., Neubauer, J., and Berry, D. A. (2006b). "Aerodynamically and acoustically driven modes of vibration in a physical model of the vocal folds," *J. Acoust. Soc. Am.* 120 (5), 2841-2849.
- Zheng, X., Bielamowicz, S., Luo, H., and Mittal, R. (2009). "A Computational Study of the Effect of False Vocal Folds on Glottal Flow and Vocal Fold Vibration During Phonation," *Ann. Biomed. Eng.* 37 (3), 625-642.

APPENDIX A. UNCERTAINTY ANALYSIS

A.1 Subglottal Pressure

The subglottal pressure at both pressure taps was measured using silicone membrane differential pressure transducers referenced to the atmospheric air outside of the subglottal duct. The total uncertainty of the pressure measurements was calculated as

$$u_{press} = \sqrt{u_{hyst}^2 + u_{calib}^2 + u_{drift}^2}, \quad (A-1)$$

where u_{hyst} , u_{calib} , and u_{drift} are the nonlinearity/hysteresis, calibration, and drift uncertainties, respectively. The combined uncertainty due to nonlinearity and hysteresis specified by the manufacturer was $\pm 0.15\%$ of the full scale output (80 mV). From this voltage a pressure value was found by dividing by the manufacturer-specified calibration of 35.200 mV/PSI and converting the units to Pa. u_{hyst} was found to be ± 23.5 Pa. u_{calib} was taken as half of the resolution of the calibration (± 0.0005), which was again converted to a pressure in Pa using the calibration value and changing units, giving an uncertainty due to calibration of ± 0.1 Pa. Over time there was a slight drift in the DC offset of the transducers, changing as much as 15 Pa while taking measurements for each case. Thus, the uncertainty due to the drift (u_{drift}) was ± 15 Pa. Substituting each uncertainty value into Equation A-1 above resulted in a total uncertainty in subglottal pressure measurement of ± 27.88 Pa.

A.2 Onset Pressure

Onset pressure was determined by gradually increasing air flow until vocal fold model vibration began and recording the post-stenosis pressure at this point. This was done five times for each case, and the means and standard deviations were found. The uncertainty of these measurements was estimated statistically, based on the sample size and spread of the measurements, by the following equation:

$$u_s = t_{v,95\%} S_{\bar{x}}. \quad (\text{A-2})$$

The standard deviation of the means ($S_{\bar{x}} = S_x/\sqrt{n}$) was calculated with the worst case standard deviation (S_x) of 57 Pa and sample size (n) of 5. The t-estimator ($t_{v,95\%}$), corresponding to 4 degrees of freedom ($v = n-1$) with a 95% confidence level, was given from tabulated data as 2.770. This resulted in an uncertainty of ± 70.61 Pa, which was combined with the uncertainty from the pressure transducer measurements as

$$u_{pon} = \sqrt{u_s^2 + u_{press}^2}. \quad (\text{A-3})$$

This gave a total uncertainty in the onset pressure of ± 75.91 Pa.

A.3 Flow Rate

Flow rate was measured with a rotometer. The uncertainty of the flow measurements takes into account uncertainties in both the resolution (u_{res}) and accuracy (u_{acc}) of the flow meter, by

$$u_{flow} = \sqrt{u_{res}^2 + u_{acc}^2}. \quad (\text{A-4})$$

The resolution uncertainty was half the resolution of 47.2 ml/s, or ± 23.6 ml/s. The accuracy uncertainty was specified by the manufacturer to be $\pm 3\%$ of the full scale output (1416 ml/s),

giving an uncertainty of ± 42.5 ml/s. These values in Equation A-4 above yield a total flow rate uncertainty of 48.6 ml/s.

A.4 Frequency

Model vibration frequency was found in LabVIEW, which determined the fundamental frequency from the power spectrum of the periodic pressure signal. The pressure signal used to find the power spectrum was recorded for 0.45 sec at 25,600 Hz, giving a frequency discrimination of 2.048 Hz. The uncertainty in the frequency measurement was taken as half of this frequency resolution, or ± 1.024 Hz.

A.5 Glottal Area

Uncertainty in the calculation of glottal area was estimated as a combination of zero-order (u_0), threshold (u_{th}), and calibration (u_c) uncertainties by

$$u_{area} = \sqrt{u_0^2 + u_{th}^2 + u_c^2}. \quad (\text{A-5})$$

The zero-order uncertainty due to the resolution of the high speed camera was taken as half of the smallest area the camera could measure, as follows:

$$u_0^2 = \pm \frac{1}{2} \left[\left(\frac{1 \text{ pixel}}{\text{pixels/mm}} \right)^2 \right]^2. \quad (\text{A-6})$$

The length scale calibration for the high speed images of 29 pixels/mm was used as the denominator in the above equation, yielding an uncertainty of $\pm 1.41 \times 10^{-6}$ mm².

The uncertainty due to thresholding took into account the change in calculated glottal area based on the selected threshold value for differentiating between the airway and the vocal fold model. This was estimated by

$$u_{th}^2 = \left(\frac{dA}{dTh} C_{th} \right)^2, \quad (A-7)$$

where A is the glottal area, Th is the threshold value (from 10 to 30 in this case, based on a scale from 0 to 255 for 8-bit grayscale intensity values), and C_{th} is the difference between threshold values (an increment of 10 was used between threshold values). The change in area per change in threshold $\left(\frac{dA}{dTh} \right)$ was found by taking the slope of a line that was fit through maximum glottal area points calculated at threshold values of 10, 20, and 30 for the 95% case. The resulting threshold uncertainty was $\pm 0.708 \text{ mm}^2$.

The calibration uncertainty took into account the change in calculated glottal area due to changes in image length scale calibration, which was determined by the user selecting two image points 10 mm apart. The uncertainty is given by

$$u_c^2 = \left(\frac{dA}{dy} y_p \right)^2, \quad (A-8)$$

where $\frac{dA}{dy}$ represents the sensitivity of the calculated glottal area to the user-selected calibration points. The length scale calibration was varied as calibration point locations were moved ± 2 pixels in the y -direction. Glottal area was calculated using each different calibration, and $\frac{dA}{dy}$ was calculated as the difference in maximum and minimum glottal areas over the overall difference in y -position of the selected points corresponding to those areas. The uncertainty in pixel location of the points (y_p) was estimated to be ± 4 pixels. Calibration uncertainty was found to be $\pm 0.631 \text{ mm}^2$.

Substituting the individual uncertainty values into Equation A-5 gave a total uncertainty in glottal area of $\pm 1.157 \text{ mm}^2$.